IMPACT OF PRESSURE ON DEFORMATION OF A COMPLIANT WALL IN A TURBULENT BOUNDARY LAYER

by

Jin Wang

A dissertation submitted to Johns Hopkins University in conformity with

the requirements for the degree of Doctor of Philosophy

Baltimore, Maryland

October 2019

Abstract

In this thesis, we have introduced a 3D integration method. This parallel-line, omni-directional integration procedure (Omni3D) calculates the pressure at every point by integration from all directions. To reduce the computational costs, the calculations are performed by a GPU-based algorithm, which determines the 3D pressure field from tomographic PIV data in 1 min. The accuracy of Omni3D is compared to that of several techniques, including procedures based on solving the Pressure Poisson Equation (PPE). The error analysis is based on Direct Numerical Simulation (DNS) data for isotropic turbulence, synthetic 3D PIV images for turbulent channel flow generated from DNS data. For acceleration fields with low errors and properly specified boundary conditions, Omni3D and PPE give similar results. However, Omni3D is more effective in suppressing the effects of acceleration errors. Omni3D could be further improved by avoiding high error regions using e.g. giving weight to the integration path by Omni3D-Weighted method or terminating certain integration paths by Omni3D-Selected method.

Omni3D is applied to the experiment of turbulent channel flow over a compliant surface. In the experiment, the time-resolved, three-dimensional flow field and the two-dimensional surface deformation are measured simultaneously. The friction velocity Reynolds number is Re_τ=2300, and Young's modulus (E) of the wall is 1 MPa, resulting in a ratio of shear speed, Ct, to the centerline velocity, U_c, of 6.8. We used the four methods mentioned above to calculate the pressure and Omni3D-Weighted gives the highest pressure-wall normal velocity correlation values. Conditional correlations are also calculated between deformation and flow variables, including pressure to characterize the flow structures associated with the deformation. Positive deformations (bumps) caused by negative pressure fluctuations are preferentially associated with ejections involving spanwise vortices located downstream and quasi-streamwise vortices with spanwise offset. Results of conditional correlations are consistent with the presence of hairpin-like structures. The negative deformations (dimples) are preferentially associated with positive pressure fluctuations at the transition between upstream sweeps to a downstream ejection.

The recent study examines the interactions of a compliant wall with a turbulent boundary layer as the deformation scale increases from submicron to several wall units (δ_ν). Re_τ ranges from 1435 to 5179, and $E/\rho U_0^2$ varies from 59 to 2.4. Time-resolved MZI is used for measuring the spatial distribution of surface deformation, and 2-D PIV, for measuring the velocity in the inner part of the boundary layer. Reynolds stresses and two-point correlations are measured in the log layer. The deformation amplitude increases from $0.02\delta_\nu$ at $E/\rho U_0^2 = 59$ to $3.6\ \delta_\nu$ at $E/\rho U_0^2 = 2.4$. Wavenumber-frequency and 2D spatial spectra show that the deformations consist of two modes: The first is an advected mode that travels downstream at 66% of U_0 (freestream velocity), has a lattice-like structure, and a preferential spanwise alignment. The amplitude and frequency of this mode agree with the Chase (1991) and Benschop et al. (2019) model predictions. The second mode is a streamwise-aligned wave that propagates at C_t (=7.85 m/s) in the spanwise direction and has a wavelength of three times the compliant layer thickness. With decreasing $E/\rho U_0^2$, the velocity profiles in the boundary layer increasingly deviate from those of a smooth wall. Yet, these deviations begin when the deformation is $0.02\delta_\nu$. The most prominent features are a sharp decrease in velocity at $y^+<10$ and an increase in the near-wall turbulence, both consistent, for matching $E/\rho U_0^2$, with the DNS results of Rosti and Brunt (2017).

Advisor: Dr. Joseph Katz
Dissertation Reader: Dr. Tamer Zaki and Dr. William Blake

Acknowledgments

First and foremost, I would like to express my sincere gratitude to my advisor, Dr. Joseph Katz, for offering me the opportunity to work on this challenging project and providing me with all the equipment and support necessary to conduct this research. His constant guidance and encouragement motivate me through my entire graduate study. Furthermore, the intense curiosity and industriousness he has demonstrated during research are the merits I need to learn in my own future career.

I would like to thank my dissertation readers, Dr. Tamer Zaki, and Dr. William Blake, for all the suggestions they have provided for my work. Special thanks are due to Dr. Yury Ronzhes, for his help in building and maintaining the daily operation of the test facility, as well as the mechanical design of the compliant wall and the electronic instrumentation for camera-laser synchronization.

Over the past several years of my graduate study, I had the privilege to work among a group of extremely hard-working and talented colleagues, including Dr. Xiaofeng Liu, Dr. Cao Zhang, Dr. David Tan, Dr. Cheng Li, Dr. Hangjian Ling, Dr. Kaushik Sampath, Dr. Yuanchao Li, Dr. Huang Chen, Xinzhi Xue, Jibu Jose, Karuna Agarwal, Subhra Koley, Yuhui Lu and others. It is their generous help both during the research as well as in my daily life that makes this work possible. Especially, Dr. Cao Zhang performed the Tomographic PIV measurement, based on which I can run and verify my GPU-based pressure reconstruction code.

Lastly, I would like to express my gratitude to my parents and my girlfriend, for their many years of support and endless love. Especially, I deeply appreciate my girlfriend, Xiao Wu, for her patience and understanding, as well as all the happiness and joy she brought to me.

This work was supported by the Office of Naval Research (N00014-16-1-2300). The program officers are Debbie Nalchagian and Greg Orris.

Table of Contents

List of Tables

List of Figures

Chapter 1. Introduction

The former study of interactions between the laminar/turbulent boundary layer and the compliant surface has a long history. These studies are focused on laminar to turbulent boundary layer transition, skin friction reduction, structural vibration, and noise suppression. Among these investigations, the pressure field is of vital importance. Thus, a 3D pressure reconstruction technique from the Particle Image Velocimetry (PIV) has been developed. This method is used to calculate the 3D pressure field of the turbulent channel flow over a compliant surface. Besides this experiment, another series of experiments are performed to study the compliant surface deformation under the turbulent boundary layer. In the first experiment, a hard compliant surface (Young's modulus: ~1 MPa) whose shear wave speed (17 m/s) is much higher than the flow speed (2.5 m/s) has been used. As expected, a one-way coupling between the flow and the deformation is observed. The second experiment is designed carefully using the Chase (1991) model, which can predict the surface response of a compliant material to the prescribed pressure and shear excitation. Compliant surface thickness, Young modulus as well as the flow speeds are selected to satisfy the requirement of our instrumental capabilities and ensure two-way coupling. Section 1.1 gives an overview of theoretical, experimental, as well as numerical investigations of the compliant surface in drag reduction, transition delay from laminar flow to turbulent flow, flow-induced vibration and instabilities in the past decades. Section 1.2 discusses different approaches utilized in modeling the response of the compliant surface under prescribed pressure and shear wave perturbations. The Chase (1991) model and Benschop et al. (2019) model are particularly relevant to the present work because it can guide us with the design of our experiments. Hence, they are explained in detail. Section 1.3 reviews the development of PIV-based pressure measurement techniques, including solving Pressure

Poisson Equation (PPE) and direct integration of material accelerations. Section 1.4 provides an outline of this thesis.

1.1 Overview of the compliant surface – boundary layer interactions

The investigation of the compliant surface can be dated back to 1936. Gray's famous paradox in his study on dolphin's swimming showed that the dolphin needed at least seven times of muscle power of a usual mammal to support its high-speed movement in water (Gray, 1936). This paradox inspired many people to find the underlying secret of how a dolphin would use its skin to control the flow and reduce the drag. Kramer (1957) first used a compliant surface made of rubber and silicone oil to cover his experimental model. By towing the model in the water, he claimed a 50% drag reduction compared to the rigid model. The drag reduction might be attributed to the delay of transition to turbulence. However, the accuracy of Kramer's experiment was questioned by Bushnell et al. (1977). Later, a lot of experiments have been done aiming at repeating Kramer's findings in drag reduction. All investigators trying to repeat Kramer's work failed to substantiate such a claim in spite of careful consideration of experimental procedures. Blick and his co-workers (Fisher & Blick 1966; Looney & Blick 1966; Blick & Walters 1968) carried a series of experiments in a wind tunnel using a compliant wall made of a thin sheet of polyvinyl chloride (PVC). Inside the sheet, fluids with different viscosities are contained, making the damping rate adjustable. In the wind tunnel test, a turbulent drag reduction of 50% was reported, together with a 25% reduction in the Reynolds stress. However, compliant surfaces constructed by the same as Blick were tested by Harris & Lissaman (1969), no significant changes in drag and Reynolds stress between their rigid and compliant surfaces were observed. McMichael *et al*. (1980) built compliant surfaces by stretching mylar membranes over polyurethane foam sheets. They failed to find a significant change in skin friction coefficients. Lee *et al*. (1993a) conducted research on a turbulent boundary layer over a compliant surface made of polydimethylsiloxane (PDMS). A significant reduction in turbulent intensity was reported by the upward shift of the logarithmic mean velocity profile in their water tunnel experiment. Unfortunately, no information about the amount of drag reduction was available since the skin friction was not measured in the experiment. Choi *et al*. (1997) tested a similar compliant coating used by Kulik et al. (1991). Their results showed a 7% reduction of the drag and a 5% reduction of the turbulence intensity. In spite of significant efforts invested in testing compliant surfaces of different materials (e.g. anisotropic compliant material by Liu et al. 2017) and geometries (e.g. multiple compliant panels by Kulik et al. 2019), the results regarding the effect of drag reduction were still inconclusive.

For the investigation of the compliant surface, there are generally two topics, one is the effect of the compliant wall on the laminar boundary layer transition to the turbulent boundary layer, and the other is an interaction between the turbulent boundary layer and the compliant surface deformation. By choosing the flexibility and the internal damping of materials, it’s shown by Benjamin (1960, 1963) and Landahl (1962) theoretically that compliant surface could delay the transition from laminar to turbulent flow. Compliance of the wall could introduce two categories of instabilities, i.e. Tollmien-Schlichting (TS) type instabilities which also occur in the rigid smooth wall boundary layer and flow-induced surface instabilities (FISI) which is caused by the deformation of the compliant surface. These instabilities could trigger the transition of laminar flow to turbulence. The TS waves were stabilized by the wall compliance and destabilized by the material damping. The FISI, on the other hand, was destabilized by the wall compliance and stabilized by the material damping. Lee et al. (1995) studied the effect of complaint surface on the stability of the Blasius boundary layer in a wind tunnel. They confirmed that at low Reynolds numbers, when the amplitudes of FISI were small, the wall compliance reduced the growth rate of unstable TS waves. Wang et al. (2006) reached the same conclusion based on direct numerical simulation (DNS). Kumaran and others' studies on flow over flexible channels and tubes coated with elastic and hyper-elastic walls found a significant increase of instability at nearly zero Reynolds number (Kumaran, Fredrickson &Pincus 1994; Kumaran 1995, 1996, 1998a, b; Srivatsan & Kumaran 1997; Shankar &Kumaran 1999; Kumaran & Muralikrishnan 2000). They ascribe the instability to an energy transfer from the mean flow to the fluctuations because of the deformation at the interface.

The second category focuses on the interactions between the compliant surface and a fully-developed turbulent boundary layer. For soft materials, experimental studies revealed the formation of the so-called static-divergence wave (Hansen & Hunston 1974, 1983; Hansen *et al*. 1980; Gad-el-Hak *et al*. 1984). The crest of these waves was aligned in the spanwise direction, and they exhibited a low phase speed (~$0.05U_0$) and high amplitudes of the order of the coating thickness. They appeared when the free-stream velocity was several times larger than the shear wave speed of the compliant coating. Formation of such waves usually increased the drag, presumably due to an increase in surface roughness (Hansen & Hunston 1974; Gad-el-Hak *et al*. 1984). In the absence of static-divergence waves, i.e., at flow speeds lower than the onset level, the tools available to Gad-el-Hak *et al*. (1984) could not detect measurable surface deformation or changes in the mean velocity profile.

Over the past two decades, numerical simulations of interactions of a boundary layer with modeled surface compliance have taken a leading role as a research tool (e.g. Endo & Himeno 2002; Xu *et al*. 2003; Kim & Choi 2014; Xia et al. 2017; Rosti and Brandt, 2017). DNS of a turbulent channel flow ($Re_\tau=u_\tau h/\nu=150$, where u_τ is the friction velocity, h is the channel half-height and *v* is the liquid viscosity) over a soft compliant wall modeled as an array of springs and dampers by Endo & Himeno (2002) showed a moderate reduction (2.7%) of the average drag. Whereas the investigation by Xu et al. (2003) using the same model at a close Reynolds number found little change in the skin friction. Simulations by Kim & Choi (2014) at Re_τ=138 found large-amplitude quasi-2D surface waves traveling downstream at 40% of the centerline velocity when the compliant surface is soft. These waves are comparable to the static divergence wave in alignment and magnitude but differ from the latter in advection speed. The deformation pattern becomes complex and the advection speed is increased to 72% of the centerline speed. No drag reduction was found in the simulation. The DNS results by Xia et al. (2017) show that turbulent drag increase is primarily due to the increase of Reynolds shear stress term and the mean convection term. The DNS mentioned above used the spring and damper model. Rosti and Brandt (2017) performed the first DNS of turbulent channel flow (Re_τ ~180) over a hyper-elastic compliant wall, where the solid is a neo-Hookean material satisfying the incompressible Mooney–Rivlin law. They show that with increasing elasticity of the compliant surface, the flow becomes more spanwise correlated. Furthermore, the wall deformations cause a downward shift in the log layer and an increase in the slope of the mean velocity profile in the viscous sublayer. They also increase all the Reynolds stress components near the wall.

In parallel with simulations involving fluid-structure “two-way coupling”, substantial efforts were invested in modeling, computing and measuring the response of compliant walls to prescribed pressure and shear perturbations (e.g., Duncan *et al*. 1985; Duncan 1986; Ko & Schloemer 1989; Chase 1991, Benschop et al. 2019). These studies focused on material dynamics and did not involve flow simulations. Yet, they provided considerable insight on the effects of layer thickness and material properties, such as the Young and shear moduli as well as the material damping, on the response of the wall to the prescribed excitations.

1.2 Modeling of the compliant surface

For experimentalists, usually, two categories of compliant surfaces have been made. One is a thin membrane enclosing a damping material (e.g., Fisher & Blick 1966; Looney & Blick 1966; Blick & Walters 1968; Harris & Lissaman 1969; McMichael *et al*. 1980), the other is a single-layer of viscoelastic rubber (e.g., Hansen & Hunston 1974, 1983; Hansen *et al*. 1980; Gad-el-Hak *et al*. 1984, 1986; Lee *et al*. 1993a, b; Hess *et al.* 1993; Choi *et al*.1997). Accordingly, the modeling of a compliant surface can be divided into two types: the surface-based model and the volume-based model (Gad-el-Hak 2002). The spring-damper model (e.g., Carpenter & Garrad 1985, 1986; Endo & Himeno 2002; Xu *et al*. 2003; Kim & Choi 2014) is a widely used surface-based model, which simplifies the compliant surface as a thin plate supported by an array of springs and dampers. The equation regarding the wall-normal displacement is

$$\frac{\partial^2 d}{\partial t^2} = -\frac{K}{m}d - D\frac{\partial d}{\partial t} + \frac{T_x}{m}\frac{\partial^2 d}{\partial x^2} + \frac{T_z}{m}\frac{\partial^2 d}{\partial z^2} - \frac{B_x}{m}\frac{\partial^4 d}{\partial x^4} - \frac{B_z}{m}\frac{\partial^4 d}{\partial z^4} + F \tag{1.1}$$

where, $d(x, z, t)$ is the wall-normal displacement, K is the spring constant, D is the damping coefficient, T_x and T_z are the tension coefficients, B_x and B_z are flexural rigidities, F is the external forcing and m is the mass per unit area, x, y, and z denote the streamwise, wall-normal and spanwise directions, respectively. In the surface-based model, the horizontal displacement is usually neglected. For a thin membrane, the flexural rigidities are also neglected.

The second approach is the volume-based model, shown in figure 1.2, which directly solves the Navier equation for elastic materials (Landau & Lifshitz 1970),

$$\rho_c \frac{\partial^2 \boldsymbol{d}}{\partial t^2} = \frac{E}{2(1+\sigma)} \nabla^2 \boldsymbol{d} + \frac{E}{2(1+\sigma)(1-2\sigma)} \nabla(\nabla \cdot \boldsymbol{d}) \tag{1.2}$$

where $\boldsymbol{d}(x, y, z, t)$ is the displacement vector, ρ_c is the density of the compliant material, E is Young's modulus and σ is the Poisson's ratio. The viscoelasticity of the material is accounted for by replacing the real-valued modulus, E, with a complex modulus $E'+iE''$, (Fung 1965; Ferry 1970), with E' being the storage modulus, and E'' the loss modulus. The key parameter that quantifies the material viscoelasticity is the frequency-dependent loss tangent, $\zeta=E''/E'$. This type of model has been implemented by Duncan *et al.* (1985), Duncan (1986) and Chase (1991), among others.

The analysis of Chase (1991) is particularly relevant to the present study and is instrumental for elucidating many of the observations. Hence, it is summarized below.

The 2-D Chase (1991) model involves streamwise and wall-normal small-amplitude deformations. The computational domain is unbounded in the x-direction, with a layer thickness of l_0 (figure 1.2). At the fluid-solid interface, fluctuating pressure, $p_0\exp[i(kx-\omega t)]$, and wall shear stress, $\tau_0\exp[i(kx-\omega t)]$, are prescribed as the boundary conditions. Here, k is the wavenumber, ω is the angular frequency, p_0 and τ_0 are the amplitudes of the pressure and shear waves, respectively. Equation 1.2 is solved by first applying the Helmholtz decomposition, in which the 2D displacement vector, $\boldsymbol{d}=d_x\boldsymbol{i}+d_y\boldsymbol{j}$, is written in terms of a scalar potential, φ, and vector potential, ψ,

$$d_x = \frac{\partial \varphi}{\partial x} + \frac{\partial \psi}{\partial y}$$
$$d_y = \frac{\partial \varphi}{\partial y} - \frac{\partial \psi}{\partial x} \tag{1.3}$$

Here, φ and ψ are solutions of wave equations with complex wave speeds c_l and c_t, respectively. The wave speeds are related to Young's modulus and Poisson ratio through

$$c_l = \sqrt{\frac{E(1-\sigma)}{\rho(1+\sigma)(1-2\sigma)}}$$
$$c_t = \sqrt{\frac{E}{2\rho(1+\sigma)}} \tag{1.4}$$

The solutions to the wave equations are:

$$\varphi(x,y,t) = \hat{\varphi}(y)e^{i(kx-\omega t)}$$
$$\psi(x,y,t) = \hat{\psi}(y)e^{i(kx-\omega t)} \tag{1.5}$$

with amplitudes

$$\hat{\varphi}(y) = a_l \sinh\left[K_l(y+l_0)\right] + b_l \cosh\left[K_l(y+l_0)\right]$$
$$\hat{\psi}(y) = a_t \sinh\left[K_t(y+l_0)\right] + b_t \cosh\left[K_t(y+l_0)\right] \tag{1.6}$$

Here, $K_l=(k^2-\omega^2/c_l^2)^{1/2}$, $K_t=(k^2-\omega^2/c_t^2)^{1/2}$. The four unknown constants, a_l, b_l, a_t and b_t are determined based on the boundary conditions. At the top surface of the coating (y=0), the normal and shear stresses, σ_{yy} and σ_{xy} are

$$\sigma_{yy}(y=0) = \left[-p_0 + i\omega d_y(y=0)z_+\right]e^{i(kx-\omega t)}$$
$$\sigma_{xy}(y=0) = \tau_0 e^{i(kx-\omega t)} \tag{1.7}$$

These stresses are related to the displacement by

$$\begin{aligned} \sigma_{yy} &= \rho_c \left[c_l^2 \frac{\partial d_y}{\partial y} + \left(c_l^2 - 2c_t^2 \right) \frac{\partial d_x}{\partial x} \right] \\ \sigma_{xy} &= \rho_c c_t^2 \left(\frac{\partial d_x}{\partial y} + \frac{\partial d_y}{\partial x} \right) \end{aligned} \tag{1.8}$$

The second term in equation 1.7 accounts for the fluid loading, and z_+ is the acoustic impedance of the outer fluid half-space. At the bottom surface of the coating (y=-l_0), the boundary conditions are

$$\begin{aligned} & d_x \left(y = -l_0 \right) = 0 \\ & \sigma_{yy} \left(y = -l_0 \right) = -i\omega z d_y \left(y = -l_0 \right) e^{i(kx-\omega t)} \end{aligned} \tag{1.9}$$

Here, the boundary conditions restrict the streamwise motion but allow the bottom wall to move in the vertical direction. This type of condition includes the cases when the backplate is not rigid, and z is the acoustic impedance at the elastomer-back plate interface. In cases where the compliant coating is attached to a rigid base, $z \rightarrow \infty$, the second boundary condition in equation 1.9 reduces to $d_y(y=-l_0)=0$, as expected. The four constants a_l, b_l, a_t and b_t are determined using the boundary conditions equations 1.7 and 1.9. In Chapter 4, this model is implemented to predict the amplitude and phase responses of the present compliant coating to pressure perturbations.

Recently, Benschop et al. (2019) proposed another model to predict the surface response to pressure and shear excitations. The model is successfully used to calculate the power spectral density of the deformation. The Chase (1991) model and the Benschop et al. (2019) model solved the same equations, but with different boundary conditions. At the top surface of the coating (y=0), the normal and shear stresses, σ_{yy} and σ_{xy} are

$$\begin{aligned} & \sigma_{yy} \left(y = 0 \right) = -p_0 e^{i(kx-\omega t)} \\ & \sigma_{xy} \left(y = 0 \right) = \tau_0 e^{i(kx-\omega t)} \end{aligned} \tag{1.10}$$

At the bottom surface of the coating ($y=-l_0$), the boundary conditions are

$$\begin{aligned} d_x\left(y=-l_0\right)=0 \\ d_y\left(y=-l_0\right)=0 \end{aligned} \tag{1.11}$$

The boundary condition at $y=-l_0$ for the Benschop (2019) model is the same as the Chase model when the impedance of the thin plate is not considered.

We are concerned about the model because it can guide the design of our experiments. In the early stage of the experiments, a “hard” compliant surface is made. Simultaneous measurements of the 2D surface deformation by Mach-Zehner Interferometry (MZI) and the 3D velocity distributions by Tomographic Particle Image Velocimetry (TPIV) were performed. The deformation is much smaller than a wall unit and only one-way coupling is observed. Later, we carefully designed the experiment using the Chase (1991) model described above ensuring the deformation is higher than a wall unit. A “soft” compliant surface was manufactured and tested. In the subsequent experiments, the two-way coupling is found. The first experiment will be discussed briefly because it has been covered in the thesis of Zhang (2016). The second experiment will be presented in chapter 4 in detail.

1.3 Review of the PIV based pressure measurement techniques

As discussed in the Chase (1991) model, the pressure is directly related to the deformation. In the first experiment, we want to know the 3D pressure distributions and correlate it with the deformation, thus a 3D pressure reconstruction method is needed. Also, the development of a pressure reconstruction algorithm is of vital importance in serval aspects. Knowledge about pressure distribution in a flow field is important in a variety of engineering problems, e.g. determining the lift force in airplane aerodynamics, and the prediction of propeller performance and cavitation in marine hydrodynamics. Wall pressure fluctuations also play a primary role in the generation of flow-induced vibration and noise (Willmarth 1975, Blake 2017). Furthermore, one of the unresolved challenges in the modeling of high Reynolds number turbulent shear flows involves the pressure-velocity correlations in the Reynolds stress transport equations (Pope 2000, Liu and Katz 2017). The classical method for pressure-based force measurement involves the integration of the surface pressure distribution based on data obtained at discrete point pressure taps or pressure-sensitive paints (PSP) (Sexton et al. 1973, Peterson and Fitzgerald 1980, Morris 1995, Bukov et al. 1992). However, with the introduction of particle image velocimetry (PIV)-based techniques, recent unsteady force measurements on a rotary-wing already involve the calculation of the pressure distribution from the time-resolved velocity field, followed by spatial integration over the surface (Villegas and Diez 2014). Likewise, while most of the present experimental data on pressure fluctuations in turbulent flow away from boundaries has been obtained using inserted probes (e.g. Tsuji et al. 2003, 2007), recent studies have transitioned to PIV-based techniques. Several approaches have been used, including direct integration of material acceleration (Liu and Katz 2006, Joshi et al. 2014, Zhang et al. 2017), solving the Pressure Poisson Equation (PPE) (e.g. Roache 1976, de Kat and van Oudheusden 2012, van Oudheusden 2013), and integration in the Fourier domain (Huhn et. al, 2016). Methods relying on time-resolved particle tracking velocimetry (PTV) data, such as Shake-The-Box (Schanz et al. 2016), to obtain the acceleration, and then integrating it using PPE on the unstructured grid have also been introduced (van Gent et al. 2017).

Considerable effort has already been invested to determine the uncertainty in the material acceleration by the Eulerian or Lagrangian method (Lynch and Scarano 2014, de Kat and van Oudheusden 2012) as summarized in the review papers (van Oudheusden et al. 2013). In general, the conclusion of these studies is that the Lagrangian approach is less sensitive to errors in velocity (Violato et al. 2011). Recently introduced techniques to increase the accuracy of the Lagrangian approach include fluid trajectory correction (Lynch and Scarano 2013, 2014) and ensemble-averaged correlation (Jeon et al. 2014). For planar pressure reconstruction, solving the PPE is the popular approach (Villegas and Diez 2014, van Oudheusden et al. 2007, Violato et al. 2011, Schneiders et al. 2016, Jeon et al. 2016, Tronchin et al. 2015). Direct planar integration of instantaneous material acceleration has been reported initially by (Baur and Köngeter 1999), where the integration is performed along four equally-distributed paths. Since the limited number of paths carry with them cumulative effects of local acceleration errors, Liu and Katz (2006, 2013) have introduced the 2D virtual-boundary omni-directional integration method (Omni2D) and its latest version of rotating-ray omni-directional integration (Liu et al. 2016). It determined the pressure at each point by integration along with all directions originating from equally separated points along a virtual circle surrounding the sample area. This approach prevents local path clustering, especially near boundaries, and minimizes the propagation of errors from regions with high acceleration errors. This method has already been used to calculate the pressure in turbulent boundary layers (Joshi et al. 2014) and cavity shear layers (Liu and Katz 2013, 2017). Using synthetic data for comparing integration methods, Charonko et al. 2010 conclude that PPE performs better for Poiseuille flow and Omni2D is better for a vortex.

Since we want to develop a 3D method as an extension of Omni2D, the details of Omni2D will be discussed in the following. The virtual-boundary, omni-directional integration method was first developed by Liu and Katz (2006, 2013). As shown in figure 1.3, a circle enclosing the sample area is generated. Integration follows paths starting from one point on the circle and ending at another point. The actual integration is marching in zigzags, ensuring the integration steps are the shortest. Iterations (~10) are done in the first place to obtain converged boundary pressure, then the pressure at inner nodes is calculated by applying the Omni2D integration once more. The pressure at inner nodes is the average of all the integration paths. Recently, Liu et al. (2016) upgraded the virtual-boundary, omni-directional integration method into rotating-ray omni-directional integration methods and achieved higher accuracy.

While PPE can be readily extended to volumetric measurements using e.g. time-resolved tomographic PIV data (Elsinga et al. 2005, Ghaemi et al. 2012, Ghaemi and Scarano 2013), an extension of Omni2D to 3D, has been problematic owing to the massive amount of computations involved. Yet, as discussed in this paper, omni-directional integration is effective in minimizing the impact of local acceleration errors and provides a convenient means of avoiding areas with high acceleration errors. Hence, the goal is to develop and evaluate a fast and robust 3D pressure reconstruction method based on similar principles. The new GPU-based, parallel-line, 3D omni-directional method (Omni3D) discussed in the next sections integrates the material acceleration along with a series of parallel lines aligned in all possible directions. The pressure at every point is the average value obtained from integration along all the paths crossing this point. Hence, errors associated with a certain path are minimized. Iterations, typically 3-4, are used for correcting the initially assumed pressure distribution along the external surfaces of the sample volume. Hence, there is no need to prescribe a pressure distribution along the boundary. Methods for identifying and avoiding regions with particularly high material acceleration errors are also introduced and verified. The new technique is evaluated using forced isotropic turbulence data and synthetic 3D PIV data generated from the results of Direct Numerical Simulations (DNS) for turbulent channel flow. The analysis examines the propagation of errors, and effects of spatial resolution on the pressure distributions for several integrational approaches, including the more commonly used PPE method with different boundary conditions.

1.4 Outline of the thesis

To study the two-way coupling between compliant surface deformation and turbulent flow, a soft compliant surface with a magnitude of deformation larger than a wall unit needs to be produced. Besides that, measurement techniques regarding 3D distributions of velocities, pressure and 2D deformation pattern of the compliant wall are required. As is presented in Zhang et al. (2015, 2017), using the MZI and corresponding fringe enhancement as well as the phase retrieval method, 2D surface deformation down to sub-micron could be captured. With the developing of Tomographic Particle Image Velocimetry (TPIV), the 3D pressure distributions are reconstructed from 3D velocity fields using the Omni3D method we extended from the 2D Virtual-boundary, Omni-directional integration method (Omni2D). In Chapter 2, a detailed description of the concept of Omni3D and its DNS verification based on the forced isotropic turbulence and turbulent channel flow will be discussed. Chapter 3 talks about the application of Omni3D to the first experiment of turbulent channel flow over a “hard” compliant surface. To ensure a two-way coupling of flow and deformation, in Chapter 4, experiments of the turbulent boundary layer over a new softer compliant surface will be discussed. Production of the surface, measurement of 2D surface deformation and 2D PIV measurement of the near-wall flow will also be shown.

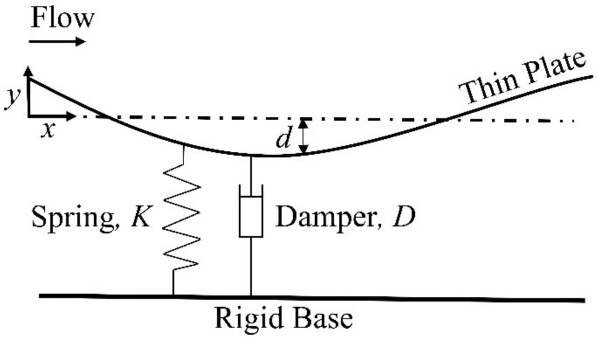

FIGURE 1.1. Sketch for the surface-based model of the compliant surface.

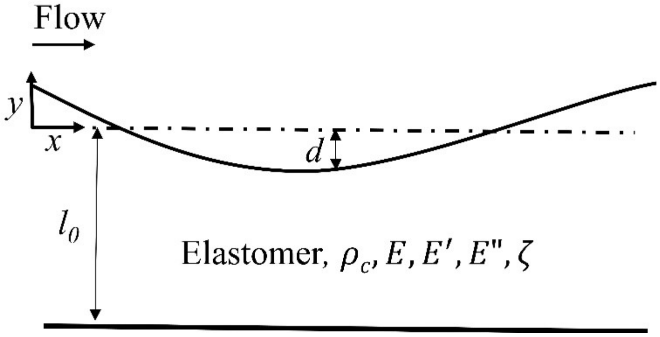

FIGURE 1.2. Sketch for the volume-based model of the compliant surface

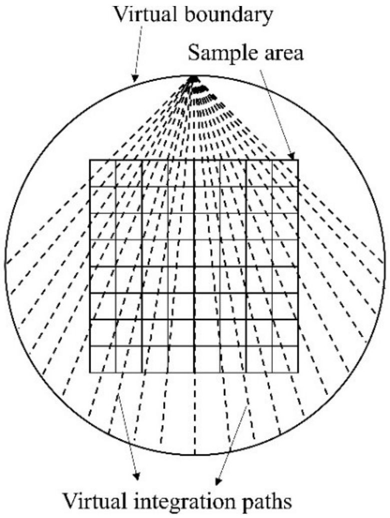

FIGURE 1.3. Sketch for the Virtual-boundary, omni-directional integration (Omni2D, Liu & Katz, 2006)

Chapter 2. GPU-based, parallel-line, omni-directional integration (Omni3D)

2.1 Outline of Omni3D method

For an incompressible flow field with velocity $\boldsymbol{u}(\boldsymbol{x},t)$, the 3D instantaneous pressure field can be obtained by integrating the Navier Stokes Eqn:

$$\frac{D\boldsymbol{u}}{Dt} = -\frac{1}{\rho}\boldsymbol{\nabla} p + \nu\nabla^2\boldsymbol{u} \tag{2.1}$$

where, *D*/*Dt* denotes the material derivative, and boldface denotes a vector. The viscous term is usually neglected away from boundaries at high Reynolds numbers but should be evaluated and included in the analysis in specific regions. For pressure reconstruction using Omni3D, groups of parallel lines covering the entire sample volume and aligned along all possible directions are used for defining the integration paths. Integration steps proceed from node to node which has the minimal distance from the straight line defined by the angle and endpoints. This process is referred to as the Parallel Line Omni-Directional Integration (PLODI) procedure in subsequent discussions. As the initial step, iterations (typically 3-4) are used for determining the pressure distribution along the boundaries that is consistent with the internal acceleration field. The first iteration uses a selected pressure distribution along each boundary using e.g. Omni2D. Different boundary planes are connected initially by matching the pressure in one of the common points, resulting in discontinuities in other points. These discontinuities are corrected/eliminated by the iterations and do not have any effect on the final converged pressure distribution. Then, the PLODI is applied to calculate the pressure difference between boundary points (only). The results of integration from all directions are averaged to provide an updated pressure in each boundary point. This procedure is subsequently repeated until the data converges, i.e. the pressure distributions along the surfaces are consistent with the internal 3D acceleration field. In the next step, PLODI is applied to compute the pressure in the inner nodes as well based on the converged pressure distribution along the boundaries. The pressure in each internal point is the average of values obtained from all integration paths that start in boundary nodes and end at this point. This averaging is aimed at minimizing the impact of propagation of random errors in acceleration along the integration paths. Computations of the internal pressure do not involve iterations.

The purpose of performing the integration along groups of parallel-line oriented in different directions is to improve the efficiency of the computations in comparison to the original Omni2D (Liu and Katz 2006, 2008, 2013, Liu et al. 2016). The two parameters for generating the parallel lines are the angle/orientation and the line spacing. As illustrated in figure 2.1, the angles are defined by connecting nodes distributed uniformly on a spherical virtual grid surrounding the sample volume to the center of the sphere. This uniform spherical grid assures that the integration angles are distributed homogeneously. In general, there are only five regular polyhedrons that can equally divide a sphere and generate a strictly uniform spherical grid, namely a tetrahedron, cube, octahedron, dodecahedron, and icosahedron, but the associated number of vertices is not large enough to satisfy the required resolution. To create a dense homogeneous grid, an initial icosahedron grid is divided recursively multiple times. In every step, the triangular surface is divided into four equal parts and then projected onto the surface of the sphere. Repeating this procedure six times generates a spherical triangular grid with 20480 faces (figure 2.1a). It should be noted, one can also use commercial software, e.g. Comsol to generate a grid on the sphere. The downgrade of the grid using Comsol will result in a decrease of accuracy, although it’s not shown here. This procedure is only used for defining the angles. The integrations by PLODI are performed from boundary to boundary nodes along parallel lines. The distance between these lines is a free parameter.

The following discussion addresses the size of the integration grid and computation time. The grid on the spherical virtual boundary should be dense enough to match the data within the sample volume. For N surface triangles on the sphere, the average solid angle of each triangle is $\Omega=4\pi/N$. The projected area of this triangle on the boundary of the sample volume is about $4\pi(L/2)^2/N$, where L is the corresponding length. To match this projected area with the characteristic resolution of the PIV data (denoted as Δx), $4\pi(L/2)^2/N\sim0.5\Delta x^2$, where the 0.5 factor accounts for the area ratio between a triangle and a square. Hence, $N\sim2\pi(L/\Delta x)^2$. For example, for a data grid of 100×47×38 velocity vectors obtained in recent tomographic PIV measurements (Zhang et al. 2015, 2017), using $L/\Delta x\sim70$ (diameter of an equivalent sphere) gives $N\sim3\times10^4$. The actual number of faces used in our calculations is 20480. The implications as far as the amount of computation involved are as follows: Suppose M is the number of angles defined by the spherical virtual grid and Δ_{LS} is the spacing between parallel lines. Then, the total number of integration paths is about $M(L/\Delta_{LS})^2$. For the above-mentioned icosahedron-based grid, according to Euler's formula (Spanier 1966), $N+M-E=2$, where E is the total number of edges. Since each edge is part of two surfaces, for triangles, $E=3N/2$, giving $N=2(M-2)$, i.e. M=10242. Choosing $\Delta_{LS}\sim\Delta x$, the number of integration paths is in the order of 10^8. Consequently, it takes more than 3 hours for integrating the acceleration in a single 100×47×38 voxel grid using a C^{++}-based code running on a quad-core, 3.7 GHz Intel i7-3860 processor. Considering that only the original acceleration data is read and integrated along a single path, the integrations along different lines are independent of each other, i.e., they do not require any communication among them. Hence, the algorithm can be readily optimized for parallel computing using a GPU system. The flow chart for the parallel computation developed for this purpose is presented in figure 2.2. It consists of five steps:

(i) Allocation of memory on the GPU device, as well as reading and transferring of the acceleration data to the GPU memory.

(ii) Using PLODI in parallel to obtain the pressure difference between each two boundary nodes, denoted as $PINT\ (n_{in}, n_{out})$, where, n_{in} and n_{out} are the starting and ending points of an integration path.

(iii) Calculating the pressure in each of the boundary nodes by averaging the results of integrations from all directions. This step is performed using

$$P_{n_{out}}^{new} = \frac{\sum_{n_{in}=1, n_{in} \neq n_{out}}^{Nsurface} (P_{n_{in}}^{old} + PINT(n_{in}, n_{out}))}{Nsurface - 1} \tag{2.2}$$

where $N_{surface}$ is the total number of grid points on the surface of the sample volume. The values of M or N could be selected independently of $N_{surface}$. Theoretically, for large line spacing and a small number of angles, some boundary points could be missed. As a rigorous error analysis later in this paper shows, such occurrence is undesirable in the application of Omni3D, and that the optimal line spacing is comparable to the grid spacing. After updating the pressure over the entire surface, this procedure is repeated until results converge. Typically, 3-4 iterations are sufficient to reach convergence. It should be noted that the iteration procedure is the same as least-square fit giving the prescribed boundary pressure difference, as shown in the Appendix. A.

(iv) Inner pressure integration: In parallel, each GPU thread is assigned an integration path from boundary to boundary nodes, and PLODI is applied to calculate and store the pressure in inner nodes along this path. The value obtained by averaging the results obtained for all the paths is the final pressure in each internal node.

(v) Transferring the data from the GPU to the host memory and storing it.

The timeline for applying the Omni3D method in the 100×47×38 voxel grid is shown in figure 2.3. As is evident, using a low cost, Tesla K40c GPU board, which has 2880 745 MHz processors and 12 GB memory, reduces the total computation time to about one minute. The data transfer and memory allocation take 16s; calculating the pressure difference between boundary nodes costs 15s; parallel iterations to obtain the pressure along the boundary takes 10s, and calculating the internal pressure costs 20 seconds. Furthermore, as recent tests have shown, using an advanced GPU Geforce RTX 2080 Ti board and the newer Cuda 8.0 toolkit, reduces the computation time of Omni3D by six times, to about 10 seconds. The pressure increments between boundary nodes are stored in the global memory of the GPU board to save the data transfer time. Consequently, only two applications of PLODI are needed to obtain a converged pressure field, one for the surface values, and the other for internal points. A modified approach, which would maintain the internal pressure differences between nodes during the initial application in step 2 could reduce it to one, however, it requires a much larger amount of memory. The current approach is 180 times faster than pressure calculations using the above-mentioned CPU. Currently, all the computations are performed in single precision (32 bit), for which the peak floating-point performance of the present GPU is 4.29 Tflops. Using double precision, this performance decreases to 1.43 Tflops, causing an increase in computation time to about 3 minutes. The computation time can be further reduced by the implementation of kernels concurrency as well as concurrency between memory copying and kernels when the code is used to compute a time series of the pressure field.

Direct Numerical Simulations (DNS) data for forced isotropic turbulence and turbulent channel flow obtained from the JHU DNS database (Li et al. 2008, Perlman et al. 2007) have been utilized for comparing the Omni3D procedure with other methods, including Omni2D and PPE with different approaches for determining the boundary conditions. The analysis involving forced isotropic turbulence compares: (i) the errors in pressure during integration of the DNS acceleration by the various techniques; (ii) the impact of introducing randomly distributed errors in acceleration in part of the flow field on the pressure in other sections and (iii) the impact of unresolved sub-grid turbulence on the pressure distribution. The channel flow DNS data is used for generating and then translating synthetic particle fields, which are then analyzed at varying resolution and approaches to obtain the corresponding velocity, acceleration, and pressure fields. Comparisons to the DNS results are used for: (i) determining the effect of the spatial resolution of the data, (ii) the effects of boundary conditions used during the analysis, (iii) the impact of regions with elevated acceleration errors on the pressure, and (vi) improvements achieved by avoiding zones with errors exceeding prescribed values. The DNS verification by isotropic turbulent will be presented in section 2.2 and DNS verification by channel flow is in section 2.3.

2.2 DNS Verification, the forced isotropic turbulence

2.2.1 Effects of boundary conditions and integration method

Velocity, pressure, and terms used for forcing the turbulence (denoted as ***f***) for a 64×64×64 grid are fetched from the JHU database. The three-component velocities are denoted by u, v and w in x, y and z directions respectively, the corresponding vectors are marked back as $\boldsymbol{u}$ and $\boldsymbol{x}$. D/Dt means the material derivatives of a quantity, e.g. *Du/Dt, Dv/Dt,* and *Dw/Dt* are the material accelerations. The distribution of material acceleration is calculated by Lagrangian tracking of imaginary particles with zero sizes. These virtual particles are placed on a regular grid at time *t*, and then tracked forward and backward in time. Their subsequent positions are calculated by solving

$$\frac{D\boldsymbol{x}_p}{Dt}(\boldsymbol{x}(t),t)=\boldsymbol{u}_p(\boldsymbol{x}(t),t) \tag{2.3}$$

where $\boldsymbol{x}_p$ and $\boldsymbol{u}_p$ are the particle location and velocity respectively, using second-order accurate Runge-Kutta integration (Yu et al. 2012) with time step equal to the temporal resolution of the DNS data. Results are interpolated onto the original DNS grid using the 6th order Lagrangian interpolation. The material acceleration is obtained using

$$\frac{D\boldsymbol{u}_p}{Dt}(\boldsymbol{x}(t),t)=\frac{\boldsymbol{u}_p(\boldsymbol{x}(t+n\Delta t),t+n\Delta t)-\boldsymbol{u}_p(\boldsymbol{x}(t-n\Delta t),t-n\Delta t)}{2n\Delta t} \tag{2.4}$$

for *n*=1, 2 and 3 and averaging them, neglecting the viscous terms, and accounting for the forcing, $\nabla p=-\frac{D\boldsymbol{u}_p}{Dt}+\boldsymbol{f}$, with the latter being available from the database. Neglecting the forcing term would cause significant errors to pressure, as shown before in Liu and Katz (2006). Four different methods for integrating $\boldsymbol{\nabla}p$ are implemented to obtain the pressure:

(i) The previously described Omni3D.

(ii) Planar integration using Omni2D (Liu and Katz, 2006, 2013) in a series of planes. However, the accelerations used are two components of 3D acceleration, accounting for out-of-plane velocity. They are then matched by applying the same procedure in a selected central perpendicular plane. The pressure distribution along the line intersecting each of the original planes is then averaged to obtain the constant needed for matching this plane with the others.

(iii) Solving PPE

$$\nabla^2 p=-\rho\nabla\cdot\frac{D\boldsymbol{u}}{Dt} \tag{2.5}$$

with Dirichlet boundary condition (BC) on one surface and Neumann (∇p) in the others. The source term is obtained by taking the divergence of the above-mentioned material acceleration.

Prior studies have shown that erroneous data originating from the Dirichlet boundary conditions are significant contributors to errors in the bulk pressure, especially near the boundary (Ghaemi et al. 2012). To reduce this effect, Omni2D is used for determining the pressure distribution along the Dirichlet boundary. Hence, this approach is referred to as PPE-Omni2D in subsequent discussions. The integration is performed iteratively using a Jacobi Poisson solver with second-order central difference discretization.

$$p_{i,j,k}^{n+1} = \frac{p_{i+1,j,k}+p_{i-1,j,k}+p_{i,j+1,k}+p_{i,j-1,k}+p_{i,j,k+1}+p_{i,j,k-1}}{8} + \frac{1}{8}\rho\Delta x^2 (\nabla \cdot \frac{D\boldsymbol{u}}{Dt})_{i,j,k} \tag{2.6}$$

Where, the sub-index of i, j and k indicates along x, y and z directions respectively.

as done in a series of recent papers (e.g. Ghaemi et al. 2012, Ghaemi and Scarano 2013, Villegas and Diez 2014). The reason why we use a Jacobi iteration instead of advanced iteration schemes is that it can be easily parallelized. The convergence criterion is the difference between results of successive iterations of less than 1e-13. To achieve such convergence, the typical number of iterations is 50,000.

(iv) Solving PPE with Dirichlet BC on one surface and Neumann on the others. Following (de Kat and van Oudheusden 2012), the Dirichlet BC is estimated using Bernoulli's Eqn.

$$p_{ref} - p' = \frac{1}{2}\rho\left(u'^2 + v'^2 + w'^2\right) = TKE \tag{2.7}$$

where (u', v', w') are the velocity fluctuation ($u_i=U_i+u_i'$) components in the (x, y, z) directions, respectively, p' is the pressure fluctuation, and p_{ref} is a constant reference pressure needed for the integration. For the DNS data, p_{ref} can be obtained from the database. This approach is referred to in this paper as PPE-Ber1. Note that for the isotropic turbulence data of the JHU DNS database, p'_{RMS}/TKE=0.5. Another approach,

$$p - p_\infty = \frac{1}{2}\rho(U_\infty^2 - U^2) \tag{2.8}$$

has been proposed by Ghaemi et al. (2012), Ghaemi and Scarano (2013) for boundary layer flows. Here p is the value used for the boundary condition; p_∞ and U_∞^2 are reference pressures and velocity, respectively; and U^2 is the instantaneous local streamwise velocity component (squared). They show that the impact of errors introduced by these boundary conditions diminishes with increasing distance from this boundary. For example, it has a small effect on the wall pressure fluctuations if the Dirichlet BC is imposed on a wall-parallel surface located 0.2δ from the wall, where δ is the boundary layer thickness. This approach is referred to as PPE-Ber2 in the discussion about channel flows.

For all the pressure fields obtained using the above-mentioned methods, the spatially averaged pressure over the entire volume, which is used as a reference pressure, is set to zero. The same applies to the DNS data. Sample instantaneous pressure distributions comparing the computed pressure (p) to the original DNS pressure (p_{DNS}), and the associated scaled errors $(p_{DNS}-p)/TKE$ are presented in the first and second rows of figure 2.4, respectively. The various Dirichlet BCs are imposed at y/L=0.28, where L denotes the DNS integral scale. A plot showing the Root-Mean-Square (RMS) of scaled error for each y averaged over 100 samples (time steps) is presented in figure 2.4j. The Probability Density Functions (PDFs) of errors over the entire volume of 100 realizations for the various conditions are shown in figure 2.4(k, l) in linear and log scales, respectively. Since results averaged over the 100 realizations display very similar trends to those observed in individual realization (not shown), the rest of the analysis performed in this section (isotropic turbulence) is based on characterizing the errors in a selected single realization. As is evident, all the instantaneous pressure distributions appear to be similar (figure 2.4a-d), but the errors differ substantially (figure 2.4e-h). The pressure and error distributions for the Omni3D (figure 2.4a, e) and PPE-Omni2D (Figure 2.4c, g) are very similar to each other, but the PDFs indicate that Omni3D has lower errors. The error distribution (figure 2.4g) and RMS value for the Omni2D method are significantly higher than those of Omni3D and PPE-Omni2D over the entire field of view. The examination of the data (not shown here) indicates that it is caused by inadequate matching of planes. Implementation of PPE-Ber1 causes a 0.26 error in the Dirichlet boundary, as expected, but it decreases to 0.01 on the opposite boundary. Evidently applying Omni2D to calculate the Dirichlet BC in applications involving PPE reduces the error substantially over the entire field of view. Another potential alternative method is to specify a Dirichlet boundary condition in a limited number of points, as done by Jeon et al. (2016) and Violato et al. (2011), or presumably, even a single Dirichlet point (PPE-PD). Sample tests performed for a single Dirichlet point display trends that are similar to those of PPE-Omni2D.

2.2.2 Error propagation

To examine the propagation of errors in acceleration, expected to occur in PIV data, randomly distributed errors with a maximum value of $3\nabla p_{max}$ is added to the DNS acceleration field in 10 *x-y* planes located at the center of the sample volume (0.12<*z/L*<0.16). A *y-z* plane view of the local error distribution for the Omni3D method is presented in figure 2.5a. Results for the PPE-Omni2D approach with the Dirichlet BC applied on the *y/L*=0.28 surface are shown in figure 2.5b. The errors for PPE-Omni2D with the Dirichlet BC imposed at *z/L*=0.28 are presented in figure 2.5c. In all cases, the errors propagate into the regions with no acceleration errors. Results for Omni3D are very similar to those of PPE-Omni2D on the Dirichlet surface is located far from the region with high acceleration error (figure 2.5c). However, when the region with imposed errors is adjacent to the Dirichlet surface (figure 2.5b), the errors near this surface are noticeably higher, mostly since the imposed errors contaminate the boundary condition. Corresponding profiles of RMS errors spatially averaged over x-y planes are plotted in figure 2.6. Figure 2.6a shows the profile for Block A marked in figure 2.5b, i.e. far from the Dirichlet boundary, and figure 2.6b presents the results for block B, namely near the Dirichlet boundary. As is evident, away from the Dirichlet boundary, the PPE-Omni2D and Omni3D results share similar error profiles. However, there is a clear difference near the Dirichlet boundary, where the error propagation of the PPE pressure is significantly higher than that of the Omni3D results. If the same comparison is performed using the PPE-Ber1 procedure, the error near the Dirichlet boundary is orders of magnitude higher.

Next, the mechanism of error propagation in the Omni3D integration is elucidated theoretically using a simplified model. As illustrated in figure 2.6c, the domain is divided into high error zone (HEZ), where the acceleration error is 300%, and a low error zone (LEZ), where the error is negligible. Three different types of integration paths are considered, all of them starting from the boundaries and ending in point A, with two of them crossing the HEZ. Path 1 starts outside of HEZ and crosses it entirely. Path 3 starts inside this zone and extends beyond it. Both are expected to contribute to the error in pA. For each path, $p_A = p_{BC} - \rho \sum (\frac{D\boldsymbol{u}}{Dt})_i \cdot \Delta \boldsymbol{l}_i$, with $\Delta \boldsymbol{l}_i$ being the integration step, and p_{BC} is the pressure along the boundary. The uncertainty that this path introduces in point A, $(\varepsilon_P^2)_A$, can be estimated from $(\varepsilon_P^2)_A = \rho^2 \sum \varepsilon_{Du/Dt,i}^2 \Delta l_i^2$, where $\varepsilon_{Du/Dt}^2$ is the acceleration error. Accordingly, the contribution to the error for a path 1 types is ${l_\varepsilon}^2 sec^2\theta \varepsilon_{Du/Dt}^2$, and for the path 3 type is $\boldsymbol{\rho^2}(\frac{l_y}{2} - \left(\frac{l_z}{2} - z_A - \frac{l_\varepsilon}{2}\right) tan\theta)^2 csc^2\theta \varepsilon_{Du/Dt}^2$, considering the error carried is proportional to path length inside the HEZ and assuming uniform error distribution inside HEZ. The total error in point A is the average value obtained from all possible integration paths. The predicted RMS error profile averaged over all values of *x* and *y* is plotted and compared to the Omni3D results in figure 2.6d. The difference between them outside of the high error zone is less than 5%. These results demonstrate that the error propagation is predictable, and as demonstrated later, will guide the development of means to alleviate the impact of high error regions.

2.2.3 Effect of sub-grid stresses

In addition to errors in velocity (discussed later), not resolving the flow field down to the Kolmogorov scale introduces sub-grid scale (SGS) stress (Rogallo and Moin 1984, Lesieur and Mètais 1996, Liu et al. 1994), $\boldsymbol{\tau} = \widetilde{\boldsymbol{u}\boldsymbol{u}} - \widetilde{\boldsymbol{u}}\widetilde{\boldsymbol{u}}$ into the momentum equation

$$\frac{\partial \widetilde{\boldsymbol{u}}}{\partial t} + \nabla \cdot \widetilde{\boldsymbol{u}}\widetilde{\boldsymbol{u}} = -\frac{1}{\rho}\boldsymbol{\nabla}\tilde{p} + \nu \nabla^2 \widetilde{\boldsymbol{u}} + \nabla \cdot (\widetilde{\boldsymbol{u}}\widetilde{\boldsymbol{u}} - \widetilde{\boldsymbol{u}\boldsymbol{u}}) + \widetilde{\boldsymbol{f}} \tag{2.9}$$

where ~ denotes a spatial filter – a box filter in the present analysis. The term $\nabla \cdot \boldsymbol{\tau}$ is introduced by the spatial filtering of the non-linear term in the Navier-Stokes equation. The balance between $\boldsymbol{\nabla}\tilde{p}$ and $D\widetilde{\boldsymbol{u}}/Dt + \nabla \cdot \boldsymbol{\tau}$ - $\nu \nabla^2 \widetilde{\boldsymbol{u}}$ in Eqn. 2.9 indicates the impact of $\nabla \cdot \boldsymbol{\tau}$ on the filtered pressure field ($\tilde{p}$) should be evaluated. The isotropic turbulence DNS velocity field is 3D box-filtered at different filter scales (Δ), ranging from 3 to $15\Delta x$ ($\Delta x = \Delta y = \Delta z$). The acceleration calculated from $\widetilde{\boldsymbol{u}}$, which would be available from under-resolved experimental data, is utilized to reconstruct the pressure field using Omni3D. The results are compared with the box-filtered pressure ($\tilde{p}$) field calculated using the original unfiltered data. Figure 2.7a shows the relative error for the same plane discussed in Figure 2.4 for $\Delta/(\Delta x) = 5$. The spatially averaged RMS error for this sample is $(p\text{-}p_{DNS})_{\mathrm{RMS}}$/TKE=0.03. To verify this error is associated with the SGS stress when the pressure field integrated from $\mathrm{D}\widetilde{\boldsymbol{u}}/Dt + \nabla \cdot \boldsymbol{\tau}$, the scaled error in pressure, shown in figure 2.7b, decreases to 0.4%. Figure 2.7c indicates that the RMS error increases almost linearly with increasing $\Delta/(\Delta x)$. Considering that p'_{RMS}/TKE=0.5 for the isotropic turbulence field, for a filter size of ~$9\Delta x$, the uncertainty in pressure is already in the order of 40% in of p'_{RMS}.

In addition to the spatial resolution of the data, the line spacing used during integration and the number of grid points defining the angles might also affect the accuracy of pressure integration. They do not maintain the original resolution of the data, then implicitly causing spatial filtering. In contrast, one would expect that the computation speed would decrease as the grid becomes coarser. In this context, inhomogeneity in the grid might also affect the accuracy and efficiency of the Omni3D procedure. Several tests are performed to quantify these effects. In the first series, line spacing is fixed at $1.0\Delta x$, but the number of grid points (i.e. angles) is varied from 0.008 times to 3 times the resolution needed for matching the data (M=10242). Two kinds of grids are used, namely a uniform mesh and a graded mesh generated by varying the edge length of the triangles linearly with distance from the North Pole from 0.05 to 2.0 of edge length in the corresponding uniform mesh. The comparison between uniform and graded meshes is aimed at determining whether bias in the number of integration lines introduced by the latter procedure affects the quality of the Omni3D data. All the computations are performed using the original acceleration field calculated from the DNS data. The resulting pressure error and computation time are plotted in figure 2.8a. As is evident (and expected), the error decreases and the computation time increases with an increasing number of grid points. The increase in computation time is linear, at least for the present range, but the decrease in error diminishes when the number of grid points is matched with the data resolution. Hence, there is no advantage in increasing the number of grid points beyond the matching level. Using an inhomogeneous grid increase the error by about 35% for a matched grid. In the second set of tests, the number of grid points is fixed at 10242, and the line spacing is increased from $0.5\Delta x$ to $2.5\Delta x$. The results shown in figure 2.8b indicate that the computation time grows exponentially and the RMS error decreases linearly with decreasing line spacing. For this range, the impact of varying the line spacing on the error is small, implying that there is a limited advantage in increasing the resolution below $1.0\Delta x$. Conversely, increasing the spacing to e.g. $2\Delta x$, increases the error by 5%, and reduces the computation time by 32%.

2.3 DNS Verification, the channel flow

2.3.1 Uncertainty in velocity and pressure based on synthetic particle traces

Velocity, pressure and particle positions are fetched from the JHU DNS Database for a turbulent channel flow at $\mathrm{Re}_\tau = u_\tau h/\nu = 1000$ (J. Graham et al. 2016) where $u_\tau$is the friction velocity and h is half channel height. The concentration of randomly distributed synthetic particles is set to maintain 11 particles per interrogation window, matching the optimum recommended in Atkinson et al. 2011. Hence, it increases with decreasing interrogation volume size. Information about the voxel and interrogation volumes involved in the different cases is provided in Table 2.1. The particle traces have a 3-D Gaussian intensity distribution, which is converted to discrete values in 5×5×5 voxel based on the integration model (Lecordier and

Westerweel 2004). A thin buffer region is added around the sample volume to allow the particles to enter and leave the simulated measurement domain. The particles are placed at time *t*, and then translated based on the DNS velocity forward and backward in time by $\pm\Delta t$ and $\pm 2\Delta t$, where Δt varies to maintain maximum particle displacement of fewer than 12 voxels. The velocity is interpolated using Lagrangian 6th order interpolation to reflect the exact location of the particle center, and its displacement is calculated using the above-mentioned method of Yu et al. (2012). The 5×5×5 voxel intensity distribution is recalculated once the 3D location of the displaced center is determined. Both cross-correlation based PIV and Particle Tracking Velocimetry (PTV) are used to calculate the velocity field. Three voxel sizes are used, namely $20/32\delta_v$ (Case I), $10/32\delta_v$ (Case II), and $5/32\delta_v$ (Case III), where $\delta_\nu = \nu/u_\tau$. For 3D PIV, the interrogation volume is mostly 32×32×32 (D_x, D_y, D_z) voxels with 50% overlap except for one case with 32×16×32 voxels. The corresponding scales in wall units (D_x^+, D_y^+, D_z^+), where$D_x^+ = D_x/\delta_\upsilon$, are also provided. Since $u_\tau \sim 0.044 U_c$, a free stream displacement of 12 voxels implies that the near-wall displacement is about 0.5 voxels and the near-wall displacement gradient is about 0.35, 0.175, and 0.08 voxels/voxel for cases I, II, and III. As discussed later, these values have a substantial effect on the accuracy of near-wall acceleration and pressure measurements. The velocity is calculated using multi-pass cross-correlation with window deformation using the commercial LaVision Davis® 8.1 software. Following de Kat and van Oudheusden (2012) and Liu and Katz (2013), the material acceleration at time *t* is calculated from the five successive 3D particle distributions. The calculated 3D displacements between time *t*-Δ*t* and *t* ($\boldsymbol{\Delta x}_{-\Delta t}$) and between t and *t*+Δ*t* ($\boldsymbol{\Delta x}_{+\Delta t}$) are used for determining the location of the same particle group in previous $(\boldsymbol{x} + \boldsymbol{\Delta x}_{-\Delta t},)$ and subsequent time steps $(\boldsymbol{x} + \boldsymbol{\Delta x}_{+\Delta t},)$. Then, the material acceleration is

$$\frac{D\boldsymbol{u}}{Dt}(\boldsymbol{x}, t) \approx \frac{u(\boldsymbol{x}+\boldsymbol{\Delta x}_{+\Delta t}, t+\Delta t) - u(\boldsymbol{x}+\boldsymbol{\Delta x}_{-\Delta t}, t-\Delta t)}{2\Delta t} \tag{2.10}$$

where $u(\boldsymbol{x} + \boldsymbol{\Delta x}_{\pm\Delta t}, t \pm \Delta t)$ is determined by cross-correlating the images at times t and $t \pm 2\Delta t$.

Table 2.1 Parameters for Synthetic PIV analysis.

	Case I	Case II	Case III
Particle Size	5×5×5	5×5×5	5×5×5
Voxel Number	1000×800×600 $0.63h \times 0.5h \times 0.38h$	1000×800×600 $0.31h \times 0.25h \times 0.19h$	1000×2000×300 $0.16h \times 0.31h \times 0.05h$
Voxel Size	$0.625\delta_v$	$0.313\delta_v$	$0.156\delta_v$
Interrogation Volume $D_x \times D_y \times D_z$	32×32×32 voxels 50% overlap	32×32×32 voxels 50% overlap	a. 32×32×32, 50% overlap b. 32×16×32, 50% overlap
$D_x^+ \times D_y^+ \times D_z^+$	$20 \times 20 \times 20$	$10 \times 10 \times 10$	a. 5 ×5×5 b. 5 ×2.5×5
Vector Spacing	$10\delta_v \times 10\delta_v \times 10\delta_v$	$5\delta_v \times 5\delta_v \times 5\delta_v$	c. $2.5\delta_v \times 2.5\delta_v \times 2.5\delta_v$ d. $2.5\delta_v \times 1.25\delta_v \times 2.5\delta_v$
Particle Displacement	Max: 12 voxels=$7.5\delta_v$ Near Wall: 0.5 voxels	Max: 12 voxels=$3.75\delta_v$ Near Wall: 0.5 voxels	Max: 12 voxels=$1.87\delta_v$ Near Wall: 0.5 voxels

For the PTV-based error analysis, it is based on the known position of particles, i.e. it does not include issues related to improper matching of traces between exposures. Only Case III is used for PTV. The velocity of each particle is calculated using a 2nd order polynomial fit to its centroid ($\boldsymbol{x}_p(t)$) and calculating the time derivative of the fitted displacement. The unstructured results are fitted onto a regular grid using a second-order singular value decomposition (SVD). The principled of SVD is introduced in Golub and Loan (1996), and the application of its 1st order version for interpolation of holographic PTV data is described in Sheng et al. (2006). The 2nd order SVD procedures (Talapatra and Katz 2013) express the spatial distribution of the velocity components based on a 2nd order 3D Taylor expansion, i.e. using both first and second-order spatial derivatives. The ellipsoidal interpolation volume is 32×16×32 voxels, with 3D 50% shift between volumes, and the particle density is increased to make sure that there are enough particles inside each ellipsoid. Using a 2nd order Taylor series expansion in space for the velocity of each particle, this procedure account for the location of this particle relative to the grid point, and the SVD interpolation provides both the velocity and its spatial gradients. The acceleration of each particle is determined from the second derivative of its fitted trajectory, i.e. $Du/Dt(\boldsymbol{x}_p\,, t) = \ddot{\boldsymbol{x}}_p(t)$. Then SVD interpolation is used for mapping the acceleration onto a regular grid.

Figure 2.9a-c show the effect of spatial resolution (cases) on the RMS error in the three velocity components scaled by inner variables ($\boldsymbol{u}^+=\boldsymbol{u}/u_\tau$), and figure 2.9d-f present the corresponding RMS errors in acceleration ($\boldsymbol{a}^+=\boldsymbol{a}\delta_\nu/u_\tau$). The effects of resolution on errors in velocity have been investigated extensively (Atkinson et al. 2011, de Silva et al. 2011, Worth et al. 2010) and are provided here as a basis for discussion about the acceleration errors. As is evident, and expected the RMS errors in velocity decrease with increasing resolution, especially in the viscous and buffer layers ($y^+<30$). The highest errors are associated with streamwise components. The present trends and values are consistent with the synthetic data-based analyses for 2D boundary layers reported by Atkinson et al. (2011), where D_x=D_y=12.5, and the LaVision results for Case B of PIV Challenge No. 2 (Stanislas et al. 2005), where D_x^+=D_y^+=3.12. For all components, there is a striking decrease in error when D_x^+=D_y^+ is decreased to 5.0, and a further decrease when D_y^+ is reduced to 2.5. The improvement is associated with a reduction in the extent of velocity change across the interrogation window, which for boundary layers occurs predominantly in the wall-normal direction. In the present analysis, as D_y^+ is reduced from 10 to 5 and to 2.5, the displacement difference across the window decreases to 5.6, 2.8, and 1.4 voxels, respectively. The PTV-SVD results have by far the lowest errors. As discussed in Talapatra and Katz (2013) for experimental holographic microscopy data, the improvements are caused by accounting for the exact location of each particle in space during interpolation onto a regular grid. The errors in acceleration include the effects of shifting of the interrogation window and velocity calculations. Similar to the trends of the velocity, the highest acceleration errors are associated with the streamwise component, for which $\varepsilon_{Du/Dt}{\sim}\varepsilon_u u_\tau/\delta_\upsilon$, and they decrease with increasing resolution, especially when the D_x^+=D_y^+=D_z^+ is reduced to 5.0. However, unlike the velocity, further reduction in D_y^+ to 2.5 has a minimal effect. Yet, using PTV-SVD at the same resolution achieves further improvements.

Figure 2.10a focuses on the effect of spatial resolution on the spatial RMS error of the dimensionless pressure ($p'^+=p'/\rho u_\tau^2$) over the sample volume calculated using Omni3D. Consequently, the integration includes the viscous terms, i.e. $\nu\nabla^2\boldsymbol{u}-D\boldsymbol{u}/Dt$. As a reference, the plot also includes the profile of the temporal RMS value of pressure fluctuations, p'^+_{RMS} available from the DNS data (Graham et al. 2016). In all the plots, the scales for p'^+_{RMS} are located on the right vertical axis. As is evident, the error in pressure decreases substantially as D_x^+=D_y^+=D_z^+ is reduced to 5. Similar to the trends of the acceleration, the impact of a further decrease in D_y^+ to 2.5 does not influence the results, but the application of PTV-SVD causes a significant reduction in error, to less than 2% of p'^+_{RMS} across the entire boundary layer. The results obtained for the two coarsest interrogation windows are high, reaching 40% of p'^+_{RMS} in the viscous and buffer layers, but decreasing to 20% and 8% for D_y^+=20 and 10, respectively, in the log layer. Keeping the interrogation window at D_x^+=5 maintains an error of ~6% over the entire channel. Note that the error spike at y^+=80 for D_x^+=D_y^+=D_z^+=10 is associated with the specific instantaneous data used in the present study, and is not a feature of the calculation procedures. As a demonstration, Figure 2.10b compares the RMS error for different samples showing that the instantaneous profiles fluctuate and the spike disappears once several realizations are averaged (the diamond represents the data currently used).

Next, the performance of the previously introduced four methods for integrating the pressure is compared for two interrogation window sizes. The discussion starts with the PTV-SVD based results, where the acceleration errors are very low. The viscous terms are included in all cases. As is evident from figure 2.11a-b, the Omni3D and PPE-Omni2D methods give essentially identical results for D_y^+=5, consistent with the results for isotropic turbulence (figure 2.11a). However, for D_y^+=2.5 (figure 2.11b), the Omni3D errors are significantly lower than those of PPE-Omni2D both in the viscous and buffer sublayers as well as near the Dirichlet boundary. In the outer layer, the better performance is (most likely) associated with better matching of the boundary values with those in the inner part of the flow field. To verify this statement, we have repeated the integration using the Omni3D results as a Dirichlet BC for the PPE method (i.e. PPE-Omni3D). In this case, the error decreases to levels that are very close to those of the Omni3D results for the outer layers. The same applies to the (minor) increase in the error of PPE-Omni2D in the inner layer, i.e. this error also diminishes if Omni3D data is used for the Dirichlet BC in the outer layer. The PPE-Ber1 and PPE-Ber2 results are erroneous in the vicinity of the Dirichlet boundary, as expected, but this error diminishes with increasing distance from this surface, matching the PPE-Omni2D near the opposite surface. The decreasing impact of the Bernoulli BC with distance has already been noted by Ghaemi et al. (2012). They observe that the effect on the wall pressure diminishes when the Dirichlet BC is imposed at $y/\delta > 0.2$. This conclusion is consistent with the present findings both for the channel flow as well as for isotropic turbulence. The Omni2D errors are 32% of p'^{+}_{RMS} over the entire flow domain for the coarse data, decreasing to less than 10% with increasing resolution. For the PIV based analysis, the results for the coarse and higher resolution data are presented in figure 2.11c-d, respectively. As expected, in all cases, the errors are much higher than those based on the PTV data. The Omni3D and PPE-Omni2D errors follow very similar trends for both the coarse and finer data, with the significant increase near the wall, and a reduction to ~8% in the outer layer. For the higher resolution data, the error remains at about 5% over the entire domain. The PPE-Ber1 and PPE-Ber2 results increase near the Dirichlet boundary interestingly to the same level as the PTV results, indicating that improvements in the data quality do not compensate for the errors introduced by the boundary conditions. Finally, the Omni2D errors are high across the entire boundary layer, reaching 60% of p'^{+}_{RMS} in the outer boundary and 100% near the wall for the coarse data. Increasing the resolution decreases this error uniformly to ~10%.

The effect of the viscous term is summarized in figure 2.12a for the fine, $D_x^+=D_y^+= Dz^+=5$, and corresponding PTV-SVD data in figure 2.12b. As is evident, not including the viscous term in the buffer and viscous sublayers, increases the error in the near-wall region by about three times to about 12% of p'^{+}_{RMS} for the PIV data, and by five times for the PTV-SVD data. Hence, the improved data quality is overwhelmed by the missing viscous terms. The differences diminish in the log region. These trends are consistent with the findings of Ghaemi et al. (2012).

2.4 Further improvement of Omni3D

As discussed in section 2.2.2, the error propagation by the Omni3D method is predictable when the acceleration error distribution is known. This section explores whether the error in pressure can be reduced if the contribution of integration paths carrying large errors is suppressed. The acceleration error can be quantified from the curl of acceleration in situations where the exact values are not known. (Lynch and Scarano 2014) or $\boldsymbol{\zeta} = \boldsymbol{\nabla} \times (-D\boldsymbol{u}/Dt + \nu\boldsymbol{\nabla}^2\boldsymbol{u})$ if the viscous term is included. For convenience, $\boldsymbol{\zeta}$ is still referred to as an acceleration error in the following analysis. Two ways to remove or weaken the effect of paths-carrying large errors are proposed here. In the first, the "selected path" method (Omni3D-SP), certain path carrying errors exceeding a prescribed level are avoided. This threshold level is determined, e.g. from the spatial histogram of$|\boldsymbol{\zeta}|$. During integration using PLODI, the local magnitudes of $\boldsymbol{\zeta}$ are compared to the selected threshold. Once a high error point is identified, this path is not used during the boundary pressure iteration phases (steps 2 and 3, figure 2.2). Subsequently, for internal pressure calculation (step 4), the integration along this path stops at the error point, and then restarted in the following point, preventing the propagation of this error to the low error zones. Once an integration path is stopped and restarted, further along, the new values do not contain direct information originating from the terminated line. Instead, the algorithm utilizes the pressure at the starting point, which is calculated by integration from all directions (without stopping) except for the stopped ones. Hence, the effects of pressure gradients in the region with bad data are accounted for. In the second, the "weighted path" method (Omni3D-WP), each integration path is given a weight, which is inversely proportional to the average value of $|\zeta|$ along this path. The integration is then performed following the regular procedures in all phases, but using the weighted values.

Several tests have been used to evaluate the impact of these methods. First, figure 2.13a presents the results for the isotropic turbulence data with the strip containing embedded 300% error in acceleration discussed in Section 2.2.2 (figure 2.6a). As is evident, both techniques reduce the RMS error in pressure for regions located outside of the high error zone. The test utilizes the $D_x^+ = D_y^+ = D_z^+ = 10$ channel flow data that has considerable error near the wall (figure 2.9e, figure 2.11c). The histogram-based threshold level is set by specifying that 25% of the data is erroneous, which in this case is concentrated mostly near the wall. The result presented in figure 2.13b shows that Omni3D-WP reduces the error near the wall by as much as 35% in comparison to the original Omni3D data, reducing the uncertainty to 32% of p'^+_{RMS}. The improvements with diminishing levels extend to y^+=120. Omni3D-SP shows limited effect near the wall, but matches the other method close at y^+>50. Interestingly, near the outer boundary, the PPE-Omni2D achieves errors lower than the other techniques. This trend occurs since the Dirichlet boundary condition used for PPE-Omni2D is not affected by the high error zones near the wall, while all the Omni3D procedures involve 3D integration to determine the boundary conditions. Hence, they are influenced by near-wall errors. The jump in error at y^+=70 is associated with the specific DNS data used in the present analysis as shown in figure 2.11b, where the edge of the buffer layer contains a series of small eddies. It disappears when the resolution is increased (figure 2.10) or if the same procedures are used to analyze another set of instantaneous data from the DNS channel flow database. Next, a 300% acceleration error is randomly added to the near-wall region (y^+<50) of the $D_x^+ = D_y^+ = D_z^+ = 10$ results. The resulting RMS error pressure profiles in figure 2.13b show that within the high error region, the weighted path method has the best performance. At y^+>50, both Omi3D-WP and Omni3D-

SP achieve a similar significant reduction in error propagation into the log layer, reducing the RMS error in pressure by 60% compared to Omni3D and by 80% compared to PPE-Omni2D. Finally, the effect of bad spots in the channel flow acceleration is examined by adding a 300% randomly-distributed noise to a cube with a side of $50\delta_v$, centered at y^+=115. The RMS errors in pressure averaged over the entire depth are presented in figure 2.13d. Clearly both Omni3D-WP and Omni3D-SP reduce the error within the high error zone and rapidly suppresses its propagation into regions located outside of it.

Apart from DNS verification, the Omni3D method is applied to the turbulent channel flow over a compliant surface, which will be discussed in the following chapter.

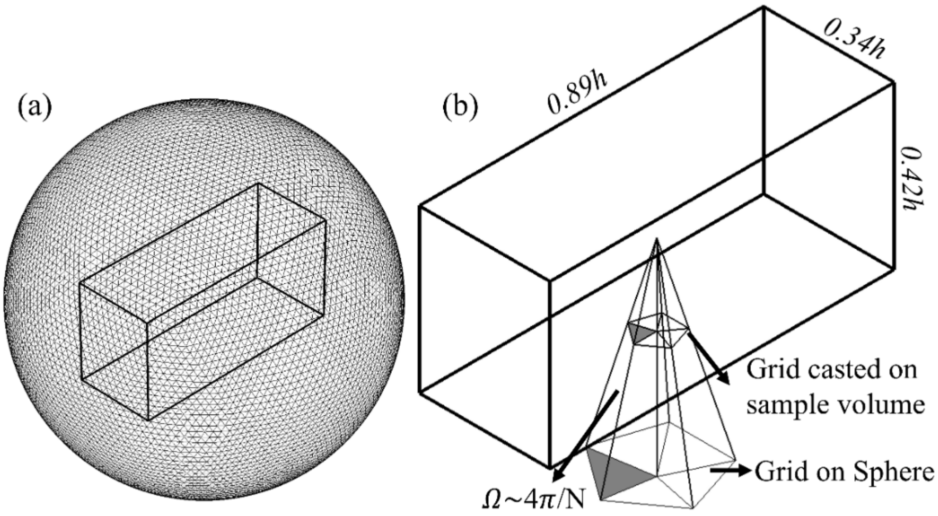

FIGURE 2.1. (a) The grid with 10242 points, and 20480 triangular surfaces used for generating the directions of the parallel line integration paths, and (b) Matching the resolution of the virtual spherical grid with that of the experimental grid on the surface of the sample volume.

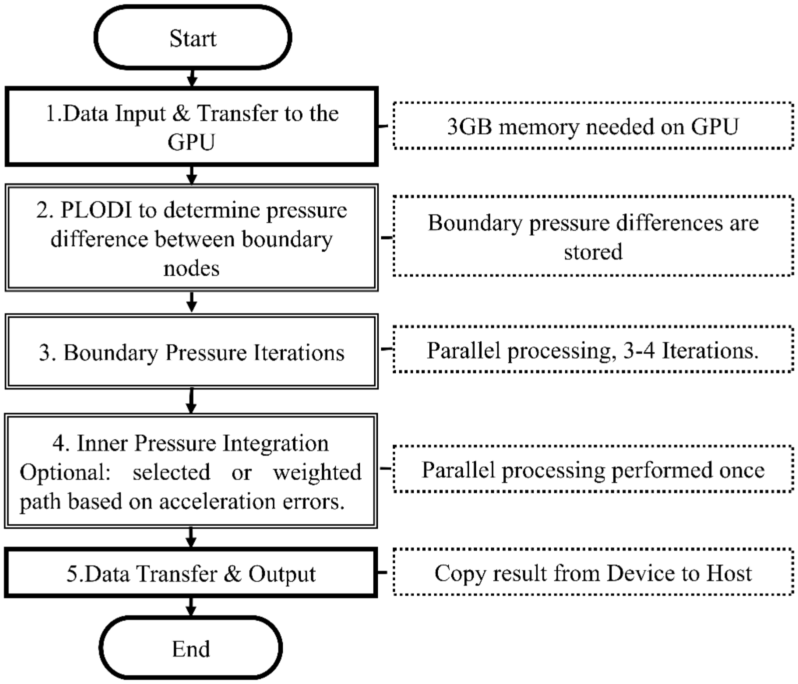

FIGURE 2.2. Flow chart (solid lines) and notes (dotted lines) for the Omni3D integration of acceleration. Double-lines indicate processes running on the GPU board, and single lines, processes run on the CPU.

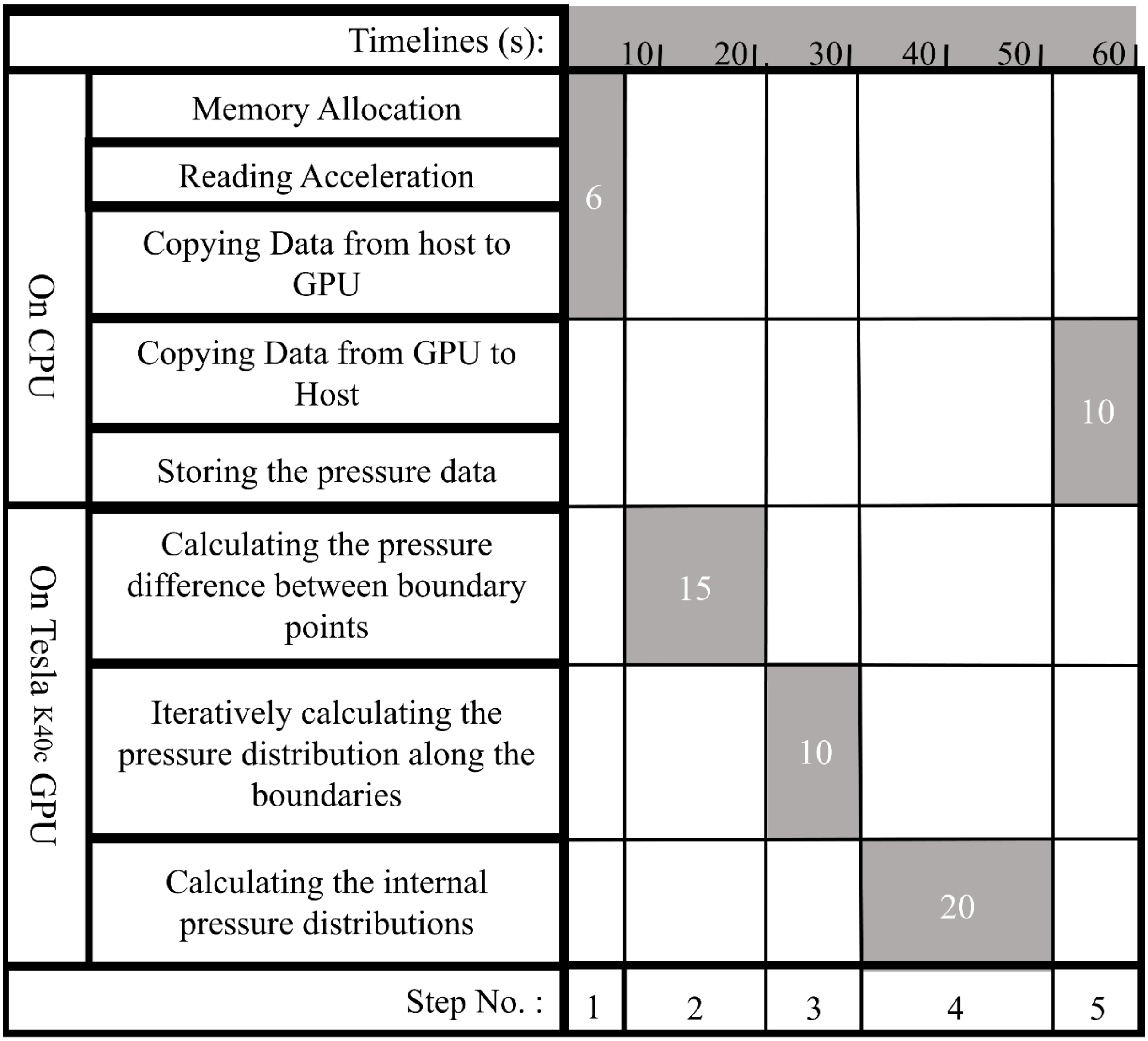

FIGURE 2.3. Timeline in seconds for application of the Omni3D method on the Tesla K40c GPU processor for a 100×47×38 voxel grid.

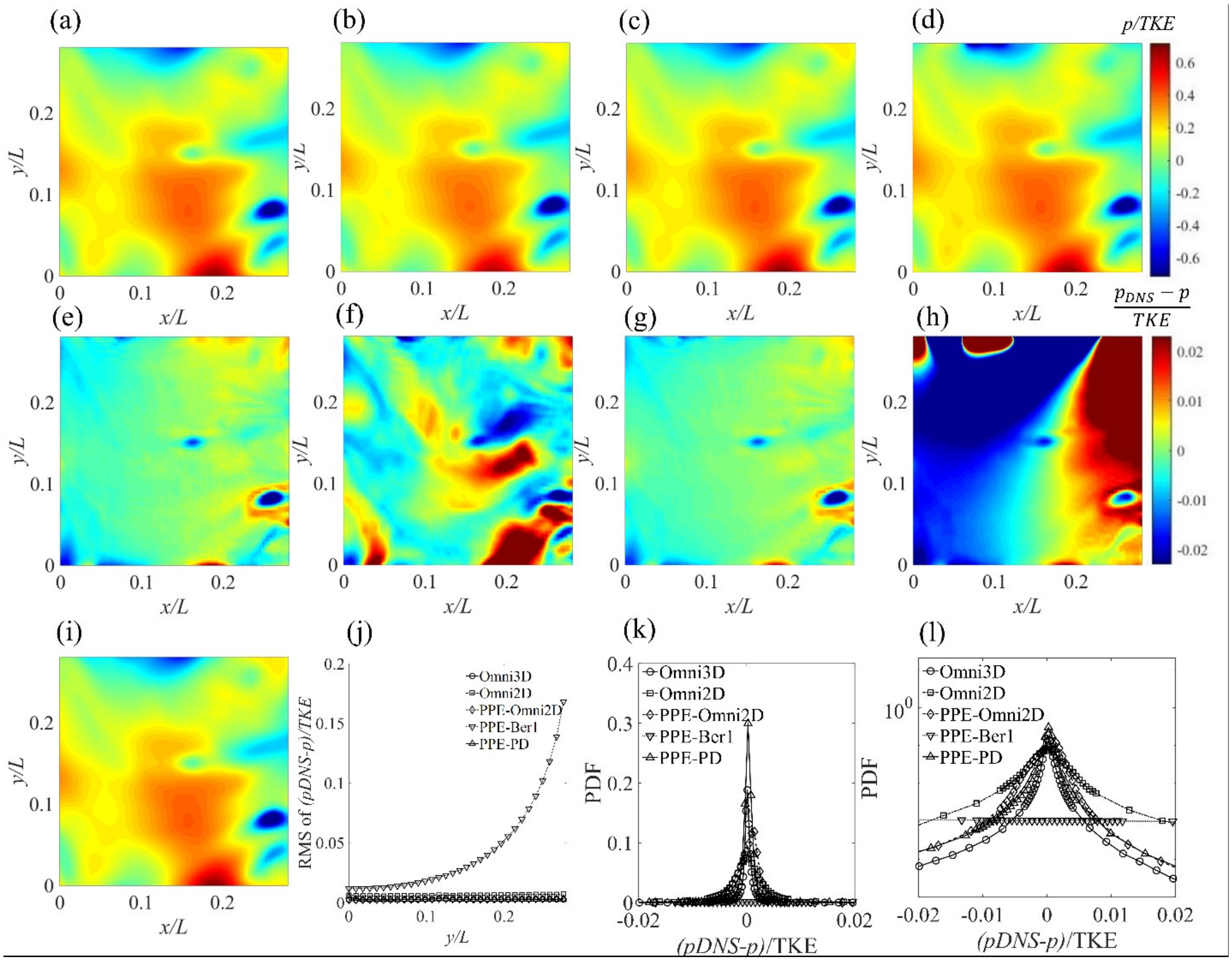

FIGURE 2.4. First row: instantaneous pressure distribution calculated using DNS data of forced isotropic turbulence (shown in i), and second row: the corresponding errors normalized by the turbulent kinetic energy (TKE). The methods used are: (a, e) 3D Omni-directional integration, (b, f) 2D Virtual-boundary Omni-directional integration, (c, g) solving PPE with Omni2D BC, and (d, h) solving PPE with Bernoulli (Ber1) BC. (j) Variations in the RMS error profile of pressure averaged over 100 samples. (k, l) PDF of error in pressure over 100 samples in linear scale and log scale.

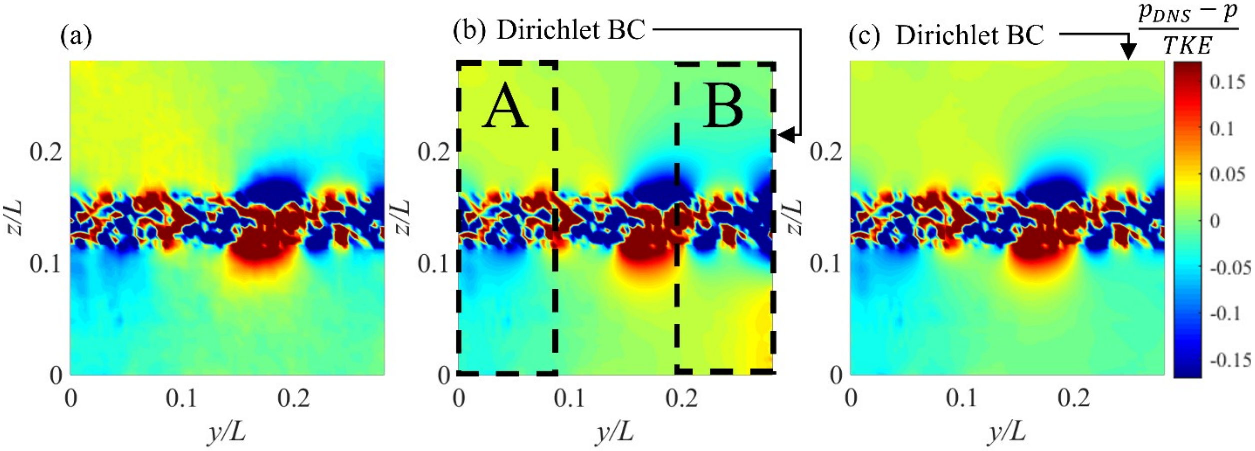

FIGURE 2.5. A sample central plane showing the effect of embedding randomly distributed ±300% error in acceleration at $0.12 < z/L < 0.16$ on the pressure distribution in the isotropic turbulence. The pressure is calculated using: (a) Omni3D, (b) PPE-Omni2D with Dirichlet BC on the $y/L=0.28$ surface, and (c) PPE-Omni2D with Dirichlet boundary condition on the $z/L=0.28$ surface.

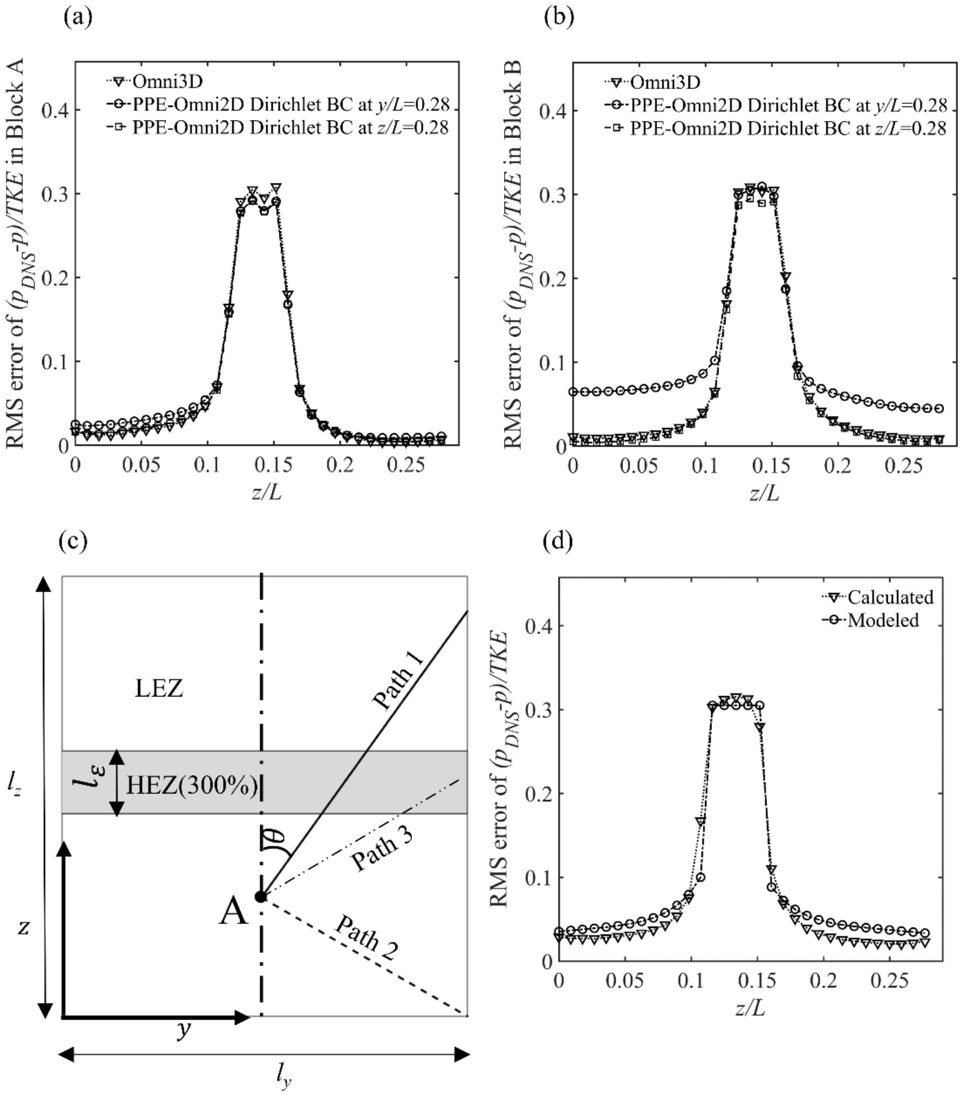

FIGURE 2.6. Spatially averaged RMS error profiles over (x, y) planes of the isotropic turbulence with an embedded error at $0.12<z/L<0.16$: (a) for block A in figure 2.5, and (b) for block B in figure 2.5. (c) Illustration of paths dissecting the high error zone (HEZ) at different angles, and (d) a comparison between modeled and calculated error profiles.

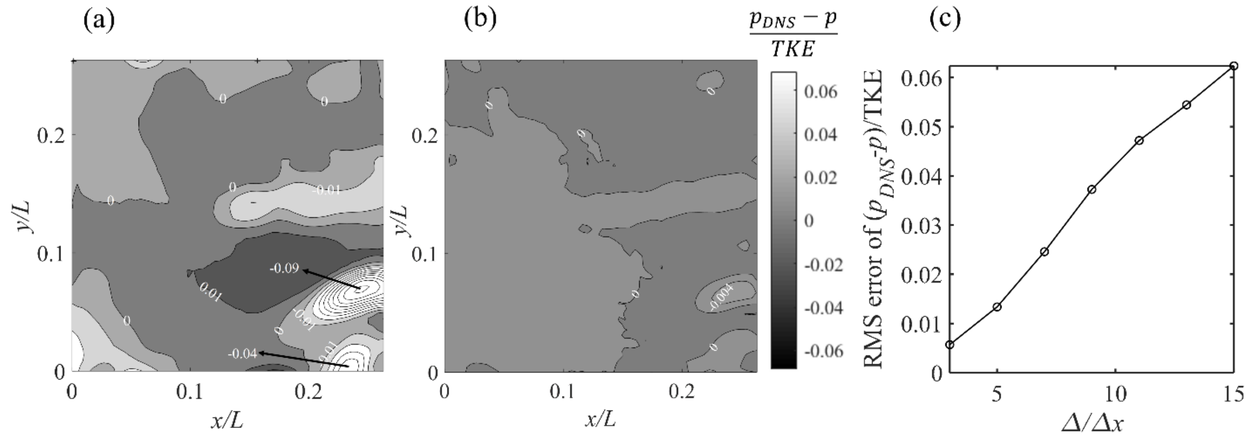

FIGURE 2.7. The SGS stress effects on the pressure calculations for isotropic turbulence: (a) A sample plane showing the error caused by integrating $D\tilde{\boldsymbol{u}}/Dt$ using 5×5×5 box-filtered data (increment between lines – 0.01), and (b) the corresponding negligible error caused by integrating $D\tilde{\boldsymbol{u}}/Dt + \nabla \cdot \boldsymbol{\tau}$, and (c) effect of filter size on the spatially averaged RMS error of pressure.

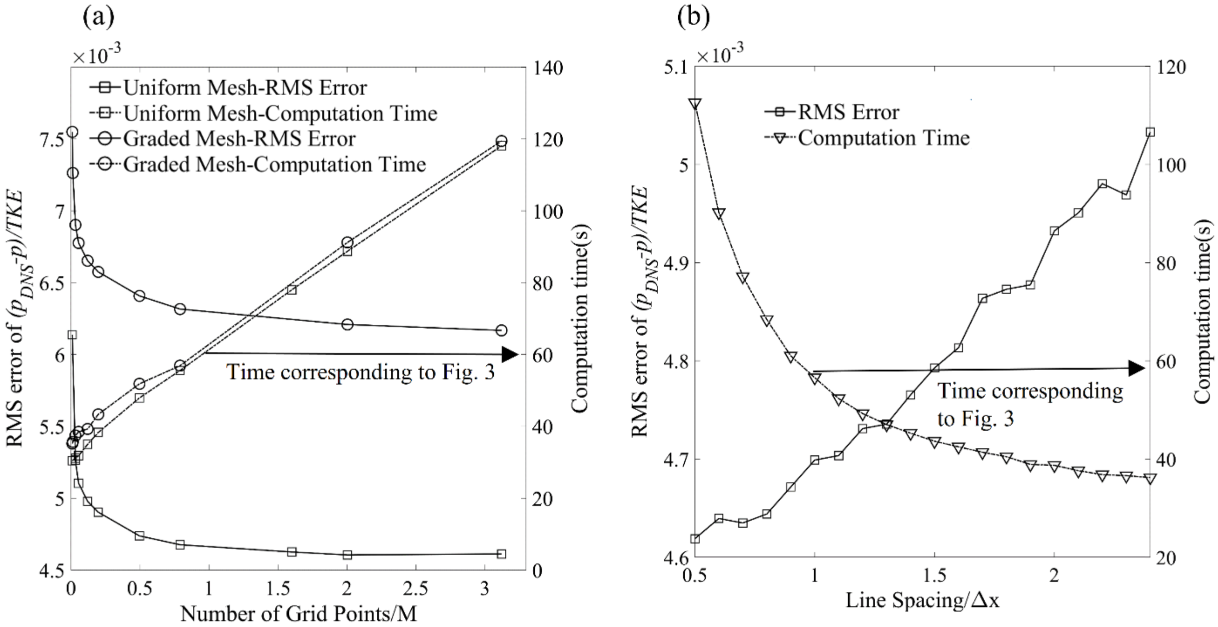

FIGURE 2.8. Effects of: (a) the number of grid points and mesh uniformity, and (b) parallel line spacing on the spatial RMS error in pressure and computation time using Omni3D.

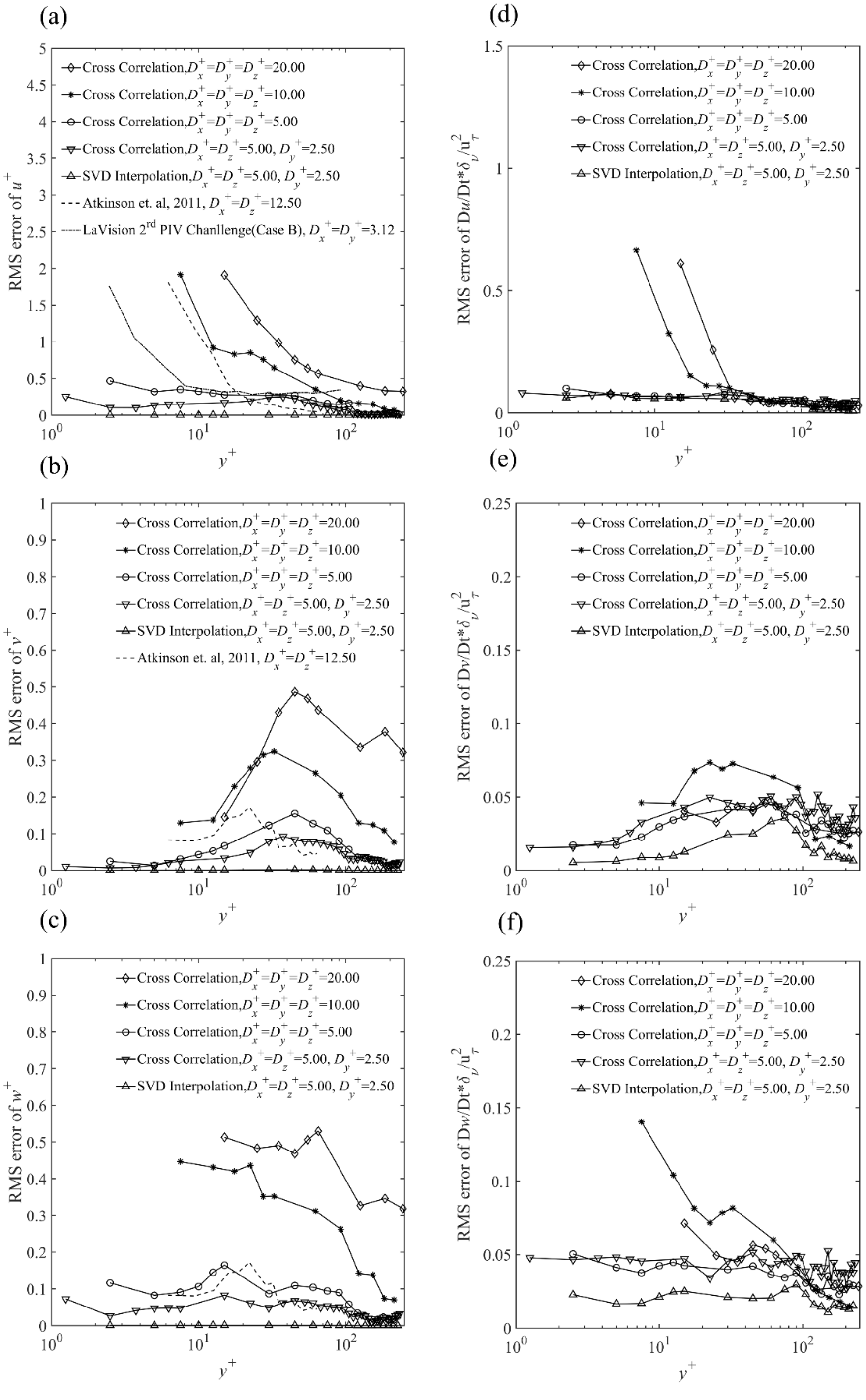

FIGURE 2.9. Effects of data resolution and velocity calculation method on the accuracy of (a) *u*, (b) *v*, (c) *w*, (d) D*u*/Dt, (e) D*v*/Dt, and (f) D*w*/Dt for the synthetic channel flow data generated from the JHU database.

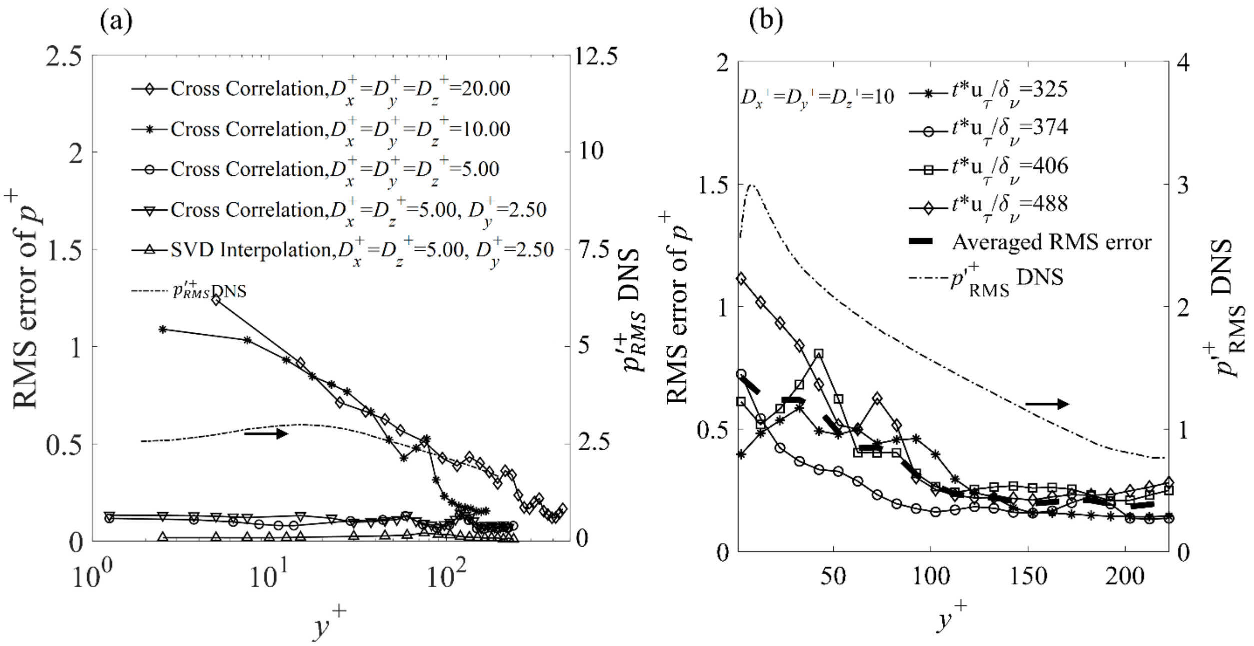

FIGURE 2.10. (a) Effects of data resolution and method for calculating the velocity on the spatial RMS error in channel flow pressure. (b) Variations of spatial RMS error in channel flow pressure for different samples. For all the samples, $D_x^+=D_y^+=D_z^+=10$. dashed-dotted line: DNS temporal RMS pressure fluctuations, with scales located at the right axis indicated by the arrow.

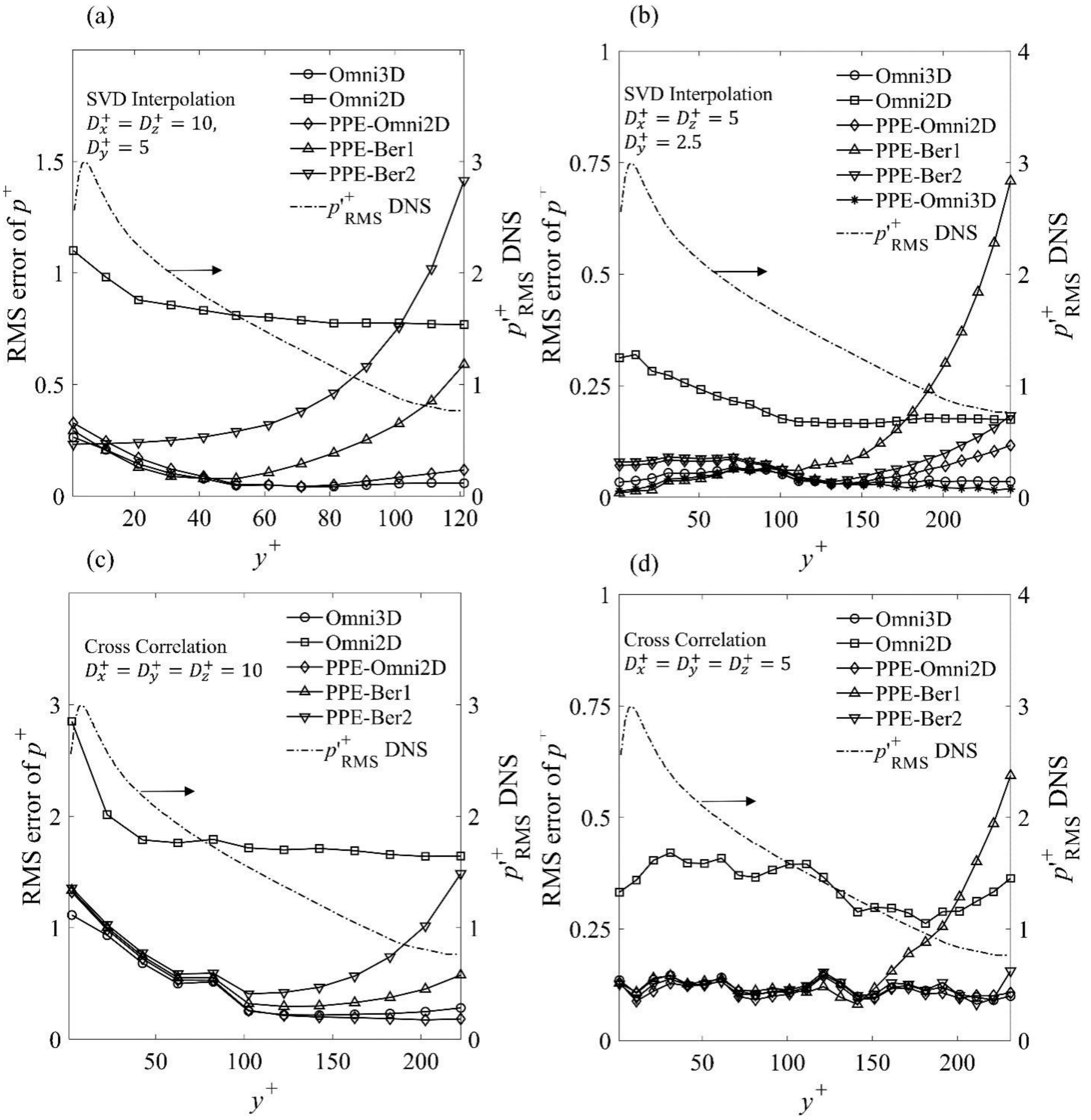

FIGURE 2.11. Effects of data resolution, a method for calculating the velocity, and integration procedure on the spatial RMS error in channel flow pressure: (a) PTV-SVD data with $D_x^+ = D_z^+ = 10, D_y^+ = 5$; (b) PTV-SVD data with $D_x^+ = D_z^+ = 5, D_y^+ = 2.5$; (c) Cross-correlation 3D PIV with $D_x^+ = D_y^+ = D_z^+ = 10$, and (d) Cross-correlation 3D PIV with $D_x^+ = D_y^+ = D_z^+ = 5$. dashed-dotted line: DNS temporal RMS pressure fluctuations, with scales located at the right axis indicated by the arrow.

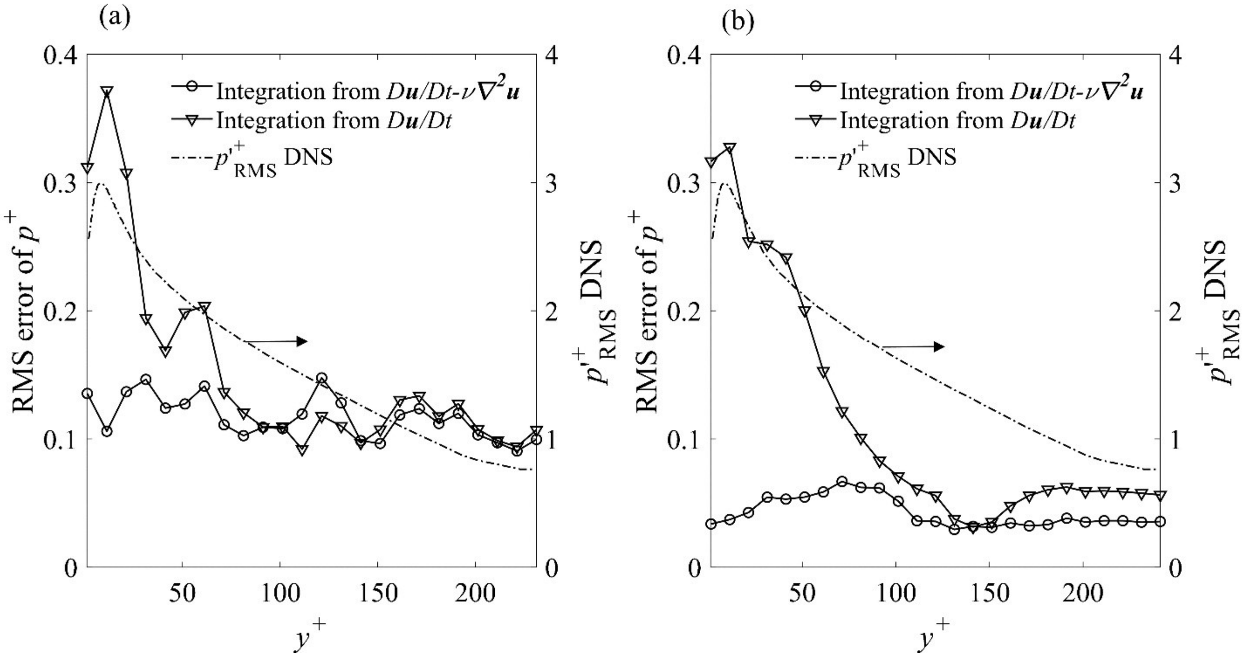

FIGURE 2.12. Effect of viscous stress on the spatial RMS error of channel flow pressure for (a) Cross-correlation with $D_x^+ = D_y^+ = D_z^+ = 5$, and (b) PTV-SVD with $D_x^+ = D_z^+ = 5, D_y^+ = 2.5$. dashed-dotted line: DNS temporal RMS pressure fluctuations, with scales located at the right axis indicated by the arrow.

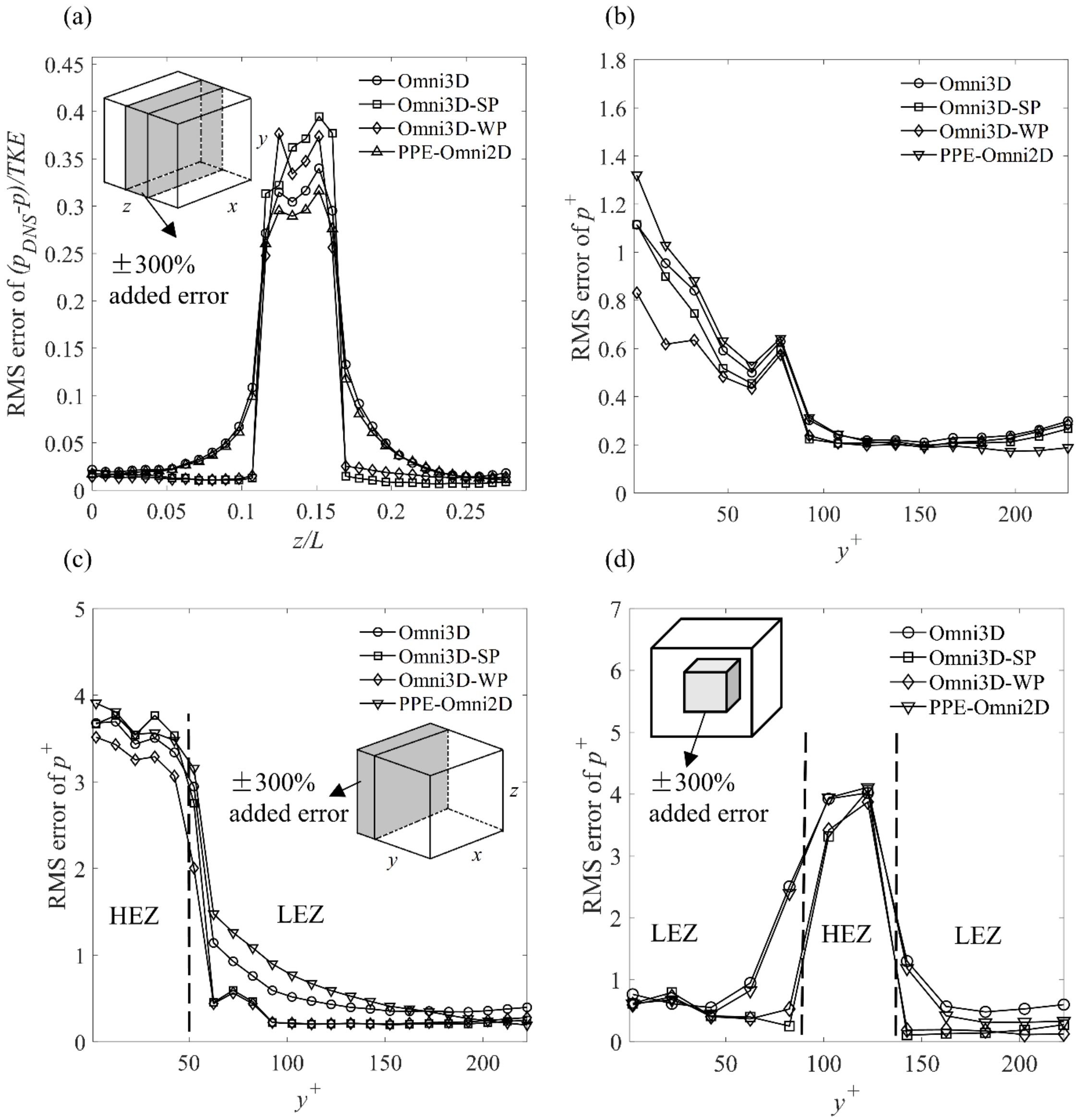

FIGURE 2.13. Effect of implementing the selected paths (Omni3D-SP) and weighted paths (Omni3D-WP) methods, both based on the magnitude of $\nabla \times \frac{Du}{Dt}$, on the spatial RMS error in pressure for: (a) isotropic turbulence with ±300% acceleration error embedded at $0.12<z/L<0.16$, (b) synthetic channel flow data with $D_x^+=D_y^+=D_z^+=10$, (c) data in (b) with ±300% acceleration error embedded at $y^+<50$, (d) data in (b) with ±300% acceleration error embedded in the central cube with side of $50\delta_v$.

Chapter 3 Experimental application of Omni3D

This chapter aims at discussion of the experimental application of Omni3D to turbulent channel flow over a compliant surface. In the experiment, time-resolved simultaneous measurement of the 3D flow by TPIV and 2D surface deformation by MZI is performed. 3D material accelerations are calculated from the TPIV measurements, subsequently, 3D pressure distributions are reconstructed from the material accelerations using Omni3D. Statistics of pressure including power spectral density and RMS pressure profiles are presented and compared with DNS results and Tsuji et al. (2007). Correlations between velocities, pressure, and deformation reveal turbulent coherent structures associated with deformations.

3.1 Experiment of turbulent channel flow over a compliant surface

3.1.1 Experimental facility and the compliant surface

The experiments have been performed in the by-pass channel of an index-match facility at Johns Hopkins University. A detailed description of the test facility can be found in published papers by scholars (Hong *et al*. 2011, 2012; Talapatra *et al*. 2012, 2013; Joshi *et al*. 2014; Zhang *et al*. 2015, Zhang et al. 2017). The relevant parts of the channel are sketched in figure 3.1a, not drawn to scale. Figure 3.1b presents a photo of the downstream half of the channel. The overall internal dimensions of the channel are 3300×50.8×203.2 mm^3 in the streamwise (*x*), wall-normal (*y*), and spanwise (*z*), directions, respectively. The corresponding instantaneous velocity components are denoted as *u*, *v* and *w*, respectively. A settling chamber containing honeycombs and screens are located upstream of the channel, which is followed by a nozzle with an area ratio of 4:1 for reducing the in-flow turbulence level. The mean flow speed in the channel is monitored by measuring the pressure drop across the nozzle using two pairs of pressure taps. Downstream of the test section, a mild diffuser with an expansion angle of less than 7° links the channel with the main loop.

The channel contains four removable windows spanning its entire width, two on the top and two on the bottom, for installing walls with different shapes, roughness, and material properties. The compliant wall assembly is flush-mounted to the bottom downstream section of the channel, with its leading-edge located 1900 mm ($75h$) downstream of the channel entrance, establishing a fully developed channel flow upstream of the measurement domain. The compliant wall is made from a homogeneous layer of transparent polydimethylsiloxane (PDMS). It is 1250 mm long in the x-direction, spans the entire width of the channel (203.2 mm), with a thickness of l_0=16 mm. The PDMS layer is attached to a 9 mm thick acrylic wall, which is strengthened from below by six equally spaced aluminum ribs mounted in the spanwise direction.

The working fluid in the channel is an aqueous solution of sodium iodide (NaI, 62% by weight). The fluid density, ρ, is 1.8×10^{3} kg/m^3 and its kinematic viscosity, ν, is 1.1×10^{-6} m^2/s. The refractive index of the NaI solution, n_{NaI}, is 1.493, which is very close to that of the acrylic channel. This refractive index matching minimizes undesired light reflections at the rigid channel wall. The refractive index of the NaI solution is also different from that of the compliant material (n_{PDMS}=1.413), which is crucial for measuring surface deformation using interferometry. In the present experiments, the channel centerline velocity, U_0, is 2.5 m s^{-1}, and the friction velocity, u_τ, determined from a linear fit of the total shear stress profile, is 0.102m/s. The resulting viscous length scale, $\delta_\nu=\nu/u_\tau$, is 11 μm, and the corresponding time scale, $\tau_\nu=\nu/u_\tau^2$, is 105.7 μs. The friction Reynolds number, Re_τ, is 2300. Following the usual convention, a superscript + is used to denote quantities normalized by u_τ and τ_ν.

The compliant material selected for this study (PDMS) is widely utilized in many other fields, such as biomechanics and microfluidics. Some previous studies attempting to reduce drag (e.g., Hess *et al*. 1993; Lee *et al*. 1993a, b) adopted the same material, but pre-mixed it with silicone oil, resulting in a much smaller shear modulus (~ 200-300 Pa). Since the high-amplitude static-divergence wave occurs when U_∞ exceeds several times of c_t (Gad-el-Hak *et al*. 1984) and usually leads to an increase in drag (Hansen *et al*. 1980), we have opted to start our work using PDMS without additives. The material comes from Dow Corning, Sylgard® 184 silicone elastomer kit. It consists of two components in liquid form, i.e., a base and a curing agent. After premixed at 10:1 (base to curing agent) weight ratio, the mixture is slowly poured into an acrylic mold with the proper dimensions. The mold is kept under vacuum to minimize air entrapment, and the mixture takes about 48 hours to cure and becomes a solid layer. The channel bottom wall assembly is integrated with this mold, eliminating the need to glue the PDMS layer on the acrylic plate. The mechanical properties of the PDMS have been measured by Rheometrics Solids Analyzer (RSA II), using other molded samples of the same material, curing temperature and base-to-curing agent ratio, with maximum strain, applied less than 2%. After 16 days of aging, the frequency-averaged moduli are E'=0.93 MPa and E''=0.07 MPa. The density of the PDMS, ρ_s, is 1.03×10^3 kg m^{-3}. The Poisson's ratio is not directly measured, the present value of σ=0.5 is based on Mark (1999). The resulting shear modulus, estimated using $G=E'/2(1+\sigma)$ is 0.31 MPa, and the shear wave speed calculated from $C_t=(G/\rho_s)^{1/2}$ is 17 ms^{-1}. The magnitude of C_t is significantly higher than the channel centerline velocity (U_0=2.5 ms^{-1}), suggesting the present compliant wall is "stiff", and the large-amplitude static-divergence waves are not expected to develop under current conditions. A prediction by the Chase model shows the magnitude deformation is in sub-microns, which is several orders smaller than a wall unit. Thus, a one-way coupling of the flow and deformation is expected.

3.1.2 Experimental setup

The volumetric time-resolved velocity measurements have been performed using the TPIV system shown in figure 3.2. Background information on TPIV can be found in e.g. Elsinga *et al*. (2006) and Scarano (2013). Briefly, the TPIV is a variation of the widely used (planar, 2D) particle image velocimetry (PIV). In TPIV, instead of illuminating particles with a thin laser sheet (<1mm) and recording images with a single camera, a thick sample volume (~10mm) is illuminated and several cameras are utilized to record images from multiple directions. The orientations of all cameras need to be carefully calibrated. Afterward, 3D particle distributions are reconstructed, followed by volumetric correlation to estimate 3D velocity distributions. This volumetric measurement technique is popularized by Elsinga *et al*. (2006) and widely used in many recent studies. In particular, the applications in boundary layers and channel flows are discussed in, e.g., Schröder *et al*. (2008, 2011), Atkinson *et al*. (2011), Schäfer *et al*. (2011).

The dimensions of the present sample volume are 30×10×10 mm^3 ($2778\times926\times929\ \delta_v^3$) in the x, y and z directions, respectively. It is located 1010 mm ($39.8h$) downstream of the leading edge of the compliant wall, and 2910 mm ($114.6h$) from the entrance to the channel. These length scales assure that the channel flow is fully developed before reaching the sample volume (Antonia & Luxton 1971; Hong *et al*. 2011). However, the 4:1 aspect ratio of the cross-section is not sufficient for establishing a 2D channel flow free from side effects (Dean 1978; Monty 2005; Hong *et al*. 2011). The flow is seeded with silver-coated hollow glass spheres (Potters Beads, SH400S20). The mean particle diameter, d_p, is 13 μm ($d_p^+=1.2$), and its density, ρ_p, is 1.6×10^3 kg m^{-3}. The particle relaxation time $\tau_s=d_p^2\rho_p/(18\rho\nu)$ is 7.6 μs, and the corresponding Stokes number, τ_s/τ_ν, is 7.2×10^{-2}. Thus, the particles are expected to follow the turbulent channel flow, except for very close to the wall.

The flow is illuminated by a high-speed Nd: YLF laser (Photonics model DM60-527) at 6kHz. The laser beam is expanded into a thick slab, and Mirror M1 on top of the channel directs 99.9% of the light to the sample volume. Mirror M3 located under the channel reflects the majority of the laser energy back to the sample volume to increase the illumination intensity. Images of the particles are recorded by four high-speed cameras (pco.dimax) located on both sides of the channel at the same elevation as the sample volume. The size of the image is 1200×600 pixel and the sampling rate is 6000 frames per second (fps), synchronized with the laser by a pulse generator (Quantum Composers, 9600+). The TPIV data is analyzed using the LaVision Davis 8.2 software and a cross-correlation volume of 48×48×48 with a 75% overlap is used. Subsequently, 3D pressure is obtained using the Omni3D method described in the above chapter.

The MZI is integrated into the TPIV system as shown in figure 3.2. Mirrors M1 and M3 located on the top and under the channel, respectively, are polished on both sides, allowing transmission of 0.1% of the laser energy through them. The light transmitted through M1 serves as a reference beam, and the light passing through the channel and M3 is the object beam. As the latter propagating through the transparent PDMS, the wall deformation alters the optical path length of the light, affecting its phase distribution. The resulting interference fringe patterns are recorded by a fifth high-speed camera (pco.dimax) at 3000 fps using 1584×1024 pixel arrays for a total of 7838 frames, corresponding to a duration of 2.6 sec ($2.5\times10^4\tau_v$). No lenses are used in front of the camera, and the magnification of the interferogram is 1:1, resulting in a field-of-view (FOV) of 17.4×11.3 mm^2 ($1611\times1046\ \delta_v^2$) in the x and z directions, respectively. The fringe spacing is about 34 pixels (374μm or $34\delta_v$).

3.2 Pressure reconstruction from TPIV

The instantaneous pressure field is spatially integrated from its gradient, $\nabla p = -\rho(D\boldsymbol{u}/Dt - \nu \nabla^2 u)$, using the measured velocity distributions to calculate the material acceleration ($D\boldsymbol{u}/Dt$). Although calculated to determine its magnitude/influence, the viscous diffusion term is neglected since the ratio between the viscous term and material acceleration is of the order of 10^{-5} based on the present TPIV data, in agreement with observations by van Oudheusden et al. (2007) and Ghaemi et al. (2012), the latter for boundary layers. The pressure reconstruction involves two steps, i.e. calculation of material acceleration and pressure integration. As discussed in Liu & Katz (2013) and de Kat & van Oudheusden (2010), and already used in the synthetic PIV test in Chapter 2, the material acceleration is calculated from five consecutive 3D particle distributions. The volume-pressure is reconstructed using Omni3D. Further reduction in errors can be achieved by avoiding (circumventing) regions where the acceleration errors are particularly high using Omni3D-WP and Omni3D-SP. These regions can be readily identified based on local closed-loop integration of material acceleration. The r.m.s. value of the relative integration error (only) is 0.46 %, a negligible effect in comparison to that caused by errors in material acceleration. Similar to procedures used for estimating ε_u, the uncertainty in material acceleration is estimated from the r.m.s. value of its curl, $\nabla \times (Du_i'/Dt)$. Provided that the viscous terms in the Navier–Stokes equation can be neglected, $\nabla \times (Du_i'/Dt)$ should be equal to zero. Assuming isotropy, $\varepsilon(D u_i'/Dt)/l \approx \langle(\nabla \times (Du_i'/Dt))^2\rangle^{1/2}$, where ε represents uncertainty. Using the present data, the estimated uncertainty in material acceleration is 32 ms^{-2}, which is approximately 45 % of the spatially averaged r.m.s. value of $D u_i'/Dt$. Since the pressure is integrated from its gradient and averaged over multiple integration directions, the relationship between $\varepsilon(p)$ and $\varepsilon(\nabla p)$ can be estimated as $\varepsilon(p) \approx \varepsilon(\nabla p)N_p l/(N_p M)^{1/2} \approx \rho N_p l/(N_p M)^{1/2}\, \varepsilon(Du_i'/Dt)$, where N_p is the number of grid points along one integration path and M is the number of grid points on the spherical virtual grid, as mentioned in Chapter 2. Thus, N_pM is the total number of integration paths. The values of N_p and M depend on the location of the sample point but vary by 10 % across the sample volume. Using the current parallel line omni-directional integration procedure, the spatially averaged values for N_p and M are 33 and 10242, respectively. Substituting these values in the equation for $\varepsilon(p)$, the corresponding uncertainty in instantaneous pressure is 0.7 Pa, which is less than 2% of the spatially averaged r.m.s. value of pressure fluctuations. This analysis does not fully account for the effect of limited spatial resolution very near the wall. In the following sections, we will briefly discuss the pressure calculated using the Omni3D method and related correlations between pressure, velocity, and deformation. Details about the deformation measurement, deformation modes as well as advection speed can be found in Zhang et al. 2017.

3.3 Statistics of pressure, and pressure-flow correlations

Sample instantaneous realizations of pressure field calculated by Omni3D-WP, Omni2D, PPE-Omni2D, and PPE-Ber1 superimposed on the velocity vectors (diluted by 2) are plotted in figure 3.3a-d, respectively. As done for the synthetic data, in all cases, the spatially averaged pressure is set to zero. In general, as expected, the pressure minima are typically associated with vortical structures, and the near-wall maximum is located at the transition from a sweeping to an ejection event, consistent with findings by Kim and Adrian (1999), Ghaemi and Scarano (2013), Joshi et al. (2014). The near-wall pressure peak of the Omni2D results are substantially higher than those of the others, but the other three appear to be qualitatively similar. Corresponding profiles of the RMS values of pressure fluctuations are presented in figure 3.4 along with published DNS data retrieved from two databases, including the previously mentioned JHU data for Re_τ=1000 (Graham et al. 2016), and the data provided by Jimenez and Hoyas for Re_τ=2003 (Jimenez and Hoyas 2008). As is evident, the Omni2D profile deviates significantly from the rest of the experimental and numerical results. For a significant fraction of the sample area, the Omni3D, Omni3D-WP, PPE-Omni2D, and PPE-Ber1 fall between the DNS-based profiles. In the outer region, the PPE-Omni2D results curve upward and those of the PPE-Ber1 have the lowest values, presumably because of the corresponding conditions along the Dirichlet boundary. In the inner part, y^+<100, all the experimental results turn upward well beyond the DNS data, consistent with the large errors expected for the present coarse resolution. However, the Omni3D-WP profile is lower than others at y^+<250 and remains within the DNS domain down to y^+=80. This trend adds confidence to the validity of the Omni3D-WP results all the way to the end of the buffer layer.

Spatial streamwise spectra calculated using FFT without any windowing or detrending from the instantaneous pressure distributions along streamwise lines are presented in figure 3.5. They are compared to spatial spectra calculated directly from the JHU DNS pressure field calculated in the same way, as well as to experimental temporal pressure spectra measured using a transducer by Tsuji et al. (2007) for nearly the same Re_τ as the present study. All the spatial spectra are averaged over the spanwise direction as well as over time, hence each curve represents an average of 266,000 lines for the experimental data, and 60,000 lines for the DNS results. The vertical lines show the wavenumber corresponding to the TPIV window size ($80\delta_v$). Results are provided for two elevations. At y^+=200 (figure 3.5a), all the experimental spectra except for the Omni2D results, collapse and fall close to those of Tsuji et al. (2007) up to a wavenumber of ~40% of that corresponding to the interrogation volume size. They also have a range of wavenumbers with the expected slope of -1.6. The JHU DNS spectrum seems to follow a similar shape, but all the values are lower, presumably because of the differences in

Reynold's number. At the upper boundary (*y/h*=0.41, figure 3.5b), the PPE-Ber1 results are substantially lower than the rest, and as prescribed (Eqn. 2.7), are quite similar to the *u'u'* spectrum. Furthermore, as prescribed, the Omni2D and the PPE-Omni2D nearly collapse. The Omni3D and Omni3D-WP spectra overlap and have the closest agreement with the Tsuji et al. (2007) data up to ~30% of the interrogation volume size wavenumber. Hence, the pressure obtained from the experimental data could be used for calculating pressure spectra provided the effects of low-pass filtering by the interrogation window is accounted for. Finally, it would be of interest to compare the pressure-vertical velocity spatial correlations, $R_{v,p}(\Delta x, \Delta y) = < p'(x, y = 0.05h, z) v'(\boldsymbol{x} + \Delta \boldsymbol{x}, \boldsymbol{y} + \Delta y, z\,) > / p'_{RMS} v'_{RMS}$, where < > indicates ensemble averaging. The vertical velocity component is selected since multiple previous studies have shown that it has the highest correlation with the pressure (Panton et al. 1980, Kobashi and Ichijo 1986, Joshi et al. 2014, Naka et al. 2015). The comparisons presented in figure 3.6 demonstrate that all the pressure integration techniques included (Omni3D-WP, Omni3D, PPE-Omni2D, and PPE-Ber1) reproduce spatial correlation maps with similar shapes, which are consistent with the above-mentioned published data (e.g. Panton et al. 1980). However, the magnitude of the correlation peak obtained using Omni3D-WP is higher than the others. Although it's not shown here, when the pressure at *y/h*=0.18 is used for the correlations, the corresponding positive correlation peak increases to 0.16, consistent with the value obtained by Joshi et al. (2014) at the same elevation.

3.4 Turbulent coherent structures associated with the deformation

This section examines briefly the conditional correlations between deformation and flow structure based on spatial correlations between the surface deformation and flow variables (velocity, pressure, vorticity, etc). The correlations are calculated the same way as $R_{v,p}(\Delta x, \Delta y)$ as discussed in section 3.3. To highlight phenomena, in many of the correlations, we impose a condition of, e.g. deformation larger or smaller than its RMS value, i.e., $d(x_0,y_0,z_0)>d_{RMS}$ or $d(x_0,y_0,z_0)<-d_{RMS}$, respectively. The condition is indicated in the definition of the variable. In such cases, the RMS values are still calculated from the original un-conditioned data.

3.4.1 Deformation and pressure correlation

Distributions of deformation-pressure conditional correlations based on large positive ($d>d_{RMS}$) event, i.e. $R_{d,p}|_{d>dRMS}$, for the (Δx, Δy, $\Delta z=0$) and ($\Delta x=0.1h$, Δy, Δz) planes are presented in figure 3.7a and b, respectively. Results conditioned on $d<-d_{RMS}$ events, $R_{d,p}|_{d<-dRMS}$, are shown in figures 3.7c and d, respectively. In all cases, the correlations are calculated for all surface points and then spatially averaged. As is evident, for positive deformation (bump), the negative correlation peak is located at $\Delta x/h\approx0.1$ and $\Delta y/h\approx0.12$, i.e. the deformation lags behind the negative pressure correlation peak by ~$0.1h$ in the streamwise direction. A second positive correlation peak with a lower magnitude is located upstream, representing a high-pressure region. The streamwise separation between the positive and negative correlation peaks is about $0.25h$, suggesting that the length scale of the pressure field relevant to the deformation is about $0.5h$. It appears that structures affecting the wall deformation are located in the log-layer, at nearly the same elevation of the Reynolds shear stress peak. The y-z distribution of correlation in figure 3.7b is presented in a plane ($\Delta x=0.1h$) that coincides with the streamwise peak in figure 3.7a. The y-z correlation peak is located at the same elevation as that in the perpendicular plane and centered around $\Delta z=0$. The distributions corresponding to negative deformation (figures 3.7c and d) appear to be quite similar to those associated with positive deformation, with the same streamwise and wall-normal offsets. However, since $d<-d_{RMS}$, a negative correlation indicates positive pressure.

3.4.2 Phase lag between deformation and pressure

This section is aimed at explaining the streamwise offset (~$0.1h$) as discussed in the previous section between pressure and deformation. It involves both the effects of damping by the compliant wall, as well as the structure of the pressure field in the boundary layer. Starting with the damping effect, one can use the Chase (1991) model to estimate phase lag. It requires knowledge of the viscoelastic properties of the compliant material, which are characterized by using complex moduli, i.e., $E'+iE''$, (e.g., Fung 1965; Ferry 1970). The key parameter is the frequency-dependent loss tangent, $\zeta=E''/E'$. To estimate the damping-induced phase lag, we start with $\zeta=0.3$ according to our measurement and others(Fitzgerald *et al*. 1998; Conte *et al*. 2002; Kulik *et al*. 2009; Du *et al*. 2013; Rubino *et al*. 2016) but repeat the calculation for other values as well. Detailed descriptions about the loss tangent of the present material and others can be found in Zhang et al. 2017.

The inclination of pressure also contributes to the phase lag. The structure of the pressure field in the channel flow can be inferred from the two-point correlation of pressure, $R_{p,p}$, which is plotted in figure 3.8a-d for reference points located at $y_0/h=0.02$, 0.15, 0.24 and 0.33, respectively. Consistent with many previous results (e.g., Kim 1989; Tsuji *et al*. 2007; Ghaemi *et al*. 2013; Joshi *et al*. 2014), the correlation contours are inclined at a rather large angle relative to the mean flow. By calculation, the estimated inclination angle around $y_0/h=0.12$ is 68°. A linear extrapolation of this line to $y=0$ suggests that the wall pressure lags by $0.048h$ behind the field pressure at $y_0/h=0.12$.

Another more accurate approach to determine pressure phase lag involves the calculation of the wavenumber-frequency cross-spectra of pressure at two different elevations,

$$C_{p,p}\left(k_x,\omega;y\right)=\left[\int p\left(x,y,z_0,t\right)e^{-ik_xx}e^{-i\omega t}dxdt\right]^*\left[\int p\left(x,y=0.12h,z_0,t\right)e^{-ik_xx}e^{-i\omega t}dxdt\right] \quad (5.2)$$

Here, * denotes complex conjugate. The magnitude of the complex $C_{p,p}$ quantifies the level of correlation between the two signals. Its argument is the phase difference, $\Delta\Phi(y)=\Phi_{0.12h}-\Phi$, between the pressure at $y_0/h=0.12$ and other elevations, as a function of k_x, ω and y. Taking into account the fact that different modes are not equally correlated, the characteristic streamwise offset is estimated from the $|C_{p,p}|$-weighted average of $\Delta\Phi/k_x$ over the entire spectrum. The procedure is performed separately for each spanwise location and then averaged. The resulting profile of $\Delta x_{p,p}=\Delta\Phi/k_x$ is presented in figure 3.9. Evidently, the wall pressure lags by $0.077h$ behind the pressure at $y/h=0.12$. This value is higher than the result obtained from extrapolating the two-point correlations, because the magnitude of $R_{p,p}$ is dominated by local events, where the correlations are high. Hence, it is biased towards small-scale pressure events. Conversely, the spectral-based weighted-average value of $\Delta x_{p,p}$ favors highly correlated events across two elevations, namely large scale structures as the distribution of $|C_{p,p}|$ demonstrates.

Figure 3.10 compares the measured streamwise offset (gray horizontal line) to the distribution of Δx_ζ (for $\zeta=0.3$) and to the combined effect of material damping and pressure field structure $\Delta x_\zeta+\Delta x_{p,p}$. The latter is provided for two values of ζ to show that they do not have a significant effect on the conclusions. As is evident, the phase lag between pressure and deformation appears to be caused in part (~24%) by material damping, but for the most part by hydrodynamic phase lag between the pressure in the log layer, where the correlation peaks, and the wall pressure.

3.4.3 Flow structures associated with the deformation

Correlations between surface deformation and flow velocity and/or vorticity distributions have been used in efforts aimed at identifying coherent flow structures associated with the wall shape. Here again, trends associated with large positive ($d>d_{RMS}$) and large negative ($d<-d_{RMS}$) deformations are displayed and discussed separately. The conditional correlations between wall deformation and three components of the velocity in selected planes are presented in figures 3.11-3.12. Among them, figure 3.11 shows *d-u* and *d-v* correlations in an *x-y* plane located at $\Delta z/h=0$. Figure 3.12 represents the distribution of *d-w* correlations in *y-z* planes at two streamwise locations, $\Delta x/h=0$, where the deformation is measured, and $\Delta x/h=0.1$, which is selected based on the maxima of *p-d* correlations. In these plots, the deformation is high-pass filtered at $\omega h/U_0=4.3$, but the velocity is not, to account for the effects of structures larger than the field of view. The analysis is performed for all planes and then spatially averaged. In addition to correlations, figures 3.11 and 3.12a and b also show the conditionally averaged projection of streamlines onto the *x-y* and *y-z* planes, respectively, calculated from the corresponding velocity components. In general, all the correlations associated with dimples are higher than those corresponding to bumps. Out of the velocity components, v' has the strongest correlation with the wall shape, followed by u' and w'.

For positive deformations, the streamlines and signs of correlations in figures 3.11a and c appear like a swirling flow with $\omega_z'<0$ centered at $\Delta x/h\approx0.1$ and $\Delta y/h\approx0.11$, coinciding with the peak of $R_{d,p}|_{d>dRMS}$ in figure 3.7a. Above the deformation, where the correlation values are high, there is a steep ejection-like flow (Q2, with $u'<0$ and $v'>0$). In the correlation maps involving spanwise velocity (figure 3.12a and c), the magnitudes are quite low. Based on the streamlines in figure 3.12a, and the signs of $R_{d,v}|_{d>dRMS}$ in figure 3.11c, the flow direction above the deformation peak ($\Delta x/h=0$) is consistent with "anti-splatting", i.e. a flow converging from both spanwise directions and turning upward. Although the signs of $R_{d,w}|_{d>dRMS}$ at $\Delta x/h=0$ and $\Delta x/h=0.1$ are similar, the vertical velocity at the latter is nearly zero. For negative deformations, both the streamlines and distribution of correlation in figures 3.11b and d show a sweeping flow (Q4, with $u'>0$ and $v'<0$) above the deformation, and a transition between an upstream sweeping flow and a downstream ejection at $\Delta x/h\approx0.1$. The zero-crossing of $R_{d,v}|_{d<-dRMS}$ at $\Delta x/h\approx0.1$ coincides with the streamwise plane of maximum deformation-pressure correlation. The y-z plane distribution of $R_{d,w}|_{d<-\sigma d}$ and streamlines at $\Delta x/h=0$ (figure 3.12b) show a splatting flow impinging on the surface and turning outward in the spanwise direction.

Given the connections established between deformation and pressure as well as between deformation and velocity, the "loop" is closed by showing the distributions of conditional pressure-velocity (unfiltered) correlation in figure 3.13. They are based on the pressure measured at $y_0/h=0.12$, where $\Delta x=\Delta y=0$. We follow the same procedures described for the deformation-velocity correlations, including spatial averaging over all planes, and calculation of the projection of conditionally averaged streamlines. To facilitate comparisons with figure 3.11, the left columns show results for $p<-p_{RMS}$, and the right column corresponds to $p>p_{RMS}$.

The main difference between deformation-velocity and pressure-velocity correlations is the height of the peak. In the velocity-deformation correlations, the center of the swirl for $d>d_{RMS}$ is located at $\Delta y=0.1$, whereas the swirl center for $p<-p_{RMS}$ and the saddle point at the center of the $p>p_{\mathrm{RMS}}$ plot shift upward with the pressure measurement point, demonstrated in figures 3.13. Although the shapes of streamlines differ, the main flow feature for $p<-p_{RMS}$ (distributions of $R_{p,u}|_{p<-pRMS}$ and $R_{p,v}|_{p>pRMS}$ and corresponding streamlines) is a large scale swirl, similar to that observed for $d>d_{RMS}$ in figure 3.11, with the streamwise shift noted. In the same manner, the primary phenomenon for $p>p_{RMS}$ is a saddle point with the flow above it resembling a sweep-ejection transition, consistent with the trends observed for $d<-d_{RMS}$. It should be noted that formation of a pressure maximum at the sweep to ejection transition has been seen in several prior studies, e.g. Kim (1983, 1989), Kobashi & Ichijo (1986), Ghaemi & Scarano (2013), Joshi *et al*. (2014), and Naka *et al*. (2015) and it's also shown in the instantaneous plot of velocity vectors and pressure in figure 3.3.

The conditional correlations between deformation and vorticity components have been calculated in order to further characterize flow structures associated with the deformation. figures 3.14a and b shows the spanwise vorticity–deformation correlations conditioned on $d>d_{RMS}$ ($R_{d,\omega z'}|_{d>dRMS}$) and $d<-d_{RMS}$ ($R_{d,\omega z'}|_{d<-dRMS}$) respectively. The peak of $R_{d,\omega z'}|_{d>dRMS}$ is located at $\Delta x/h \approx 0.1$ and $\Delta y/h \approx 0.1$, very close to the center of the spiral streamlines in figure 3.11a and c and the pressure-deformation correlation peak (figure 3.7a). It is characterized by $\omega_z' < 0$, suggesting that the bump is located preferentially behind/upstream of a spanwise vortex. To determine whether this vorticity is indeed associated with vortices, we also calculate the distribution of the conditional correlation between deformation and λ_2, which is a popular method for identifying vortices introduced by Jeong & Hussain (1995). Results for $d>d_{RMS}$, presented in figure 3.14c, show that $\Delta x/h \approx 0.1$ is characterized by negative values of λ_2, confirming the preferred presence of a vortex. Distributions of $R_{d,\omega z'}|_{d>dRMS}$ and $R_{d,\omega z'}|_{d<-dRMS}$ in x-z planes for $\Delta y=0.1$ are shown in figure 3.15a and b, respectively. For $d>d_{RMS}$, the correlation peaks at $\Delta z=0$, but it has a broader spanwise extent than $d<-d_{RMS}$ case. A consistent trend is also observed for a lower elevation, e.g., $\Delta y=0.05$, shown in figure 3.15c and d. Hence, the ejection regions above bumps are preferentially associated with negative spanwise vortices located downstream of the positive deformation.

For negative deformations, figure 3.14b shows a positive ω_z' region, also at $\Delta x/h \approx 0.1$ and $\Delta y/h \approx 0.1$. However, the corresponding values of $R_{d,\lambda 2}|_{d<-dRMS}$ at $\Delta x/h \sim 0.1$, which are presented in figure 3.14d, are negative. Hence, λ_2 is preferentially positive, i.e. the dimples are not associated with the presence of vortices, consistent with the shape of streamlines. This observation indicates that the $\omega_z'>0$ regions at the sweep-ejection transition around $\Delta x/h=0.1$ are associated with low vorticity magnitude. It is presumably caused by a decrease in near-wall velocity gradients as the flow is slowing down under the influence of adverse pressure gradients, culminating with separation/ejection.

Additional confirmation can be obtained by plotting the conditionally averaged flow field under the same conditions. Figure 3.15c shows iso-surfaces of $\overline{\omega_x' h/U_0}$ =-0.17 and 0.25, as well as $\overline{\omega_z' h/U_0}$ =-0.2 in different colors (overbar indicates conditionally averaged variable). It confirms the preferred presence of an inclined quasi-streamwise vortex as well as a counter-rotating (negative) vortex on the other side of the deformation, located at a distance of $\Delta z=0.15h$ ($\Delta z^+=350$) from the conditioning point. It also shows the region with high $\overline{\omega_z' h/U_0}$ at the head of the hairpin. Finally, figure 3.15c also shows several conditionally averaged vortex lines originating from the vicinity of the vorticity conditioning point, passing through the hairpin head, and turning back into the other leg. Clearly, the positive deformation is located upstream of a negative spanwise vortex and flanked by streamwise vortices of opposite signs, consistent with the features of a hairpin-like structure. If the analysis is repeated by imposing $\omega_x'(0,0.08h,-0.05h)<0$, the 3D depiction appears to be quite similar except for a swap in the size of the iso-surfaces of $\overline{\omega_x' h/U_0}$, corresponding to the location of the conditioning point.

(a)

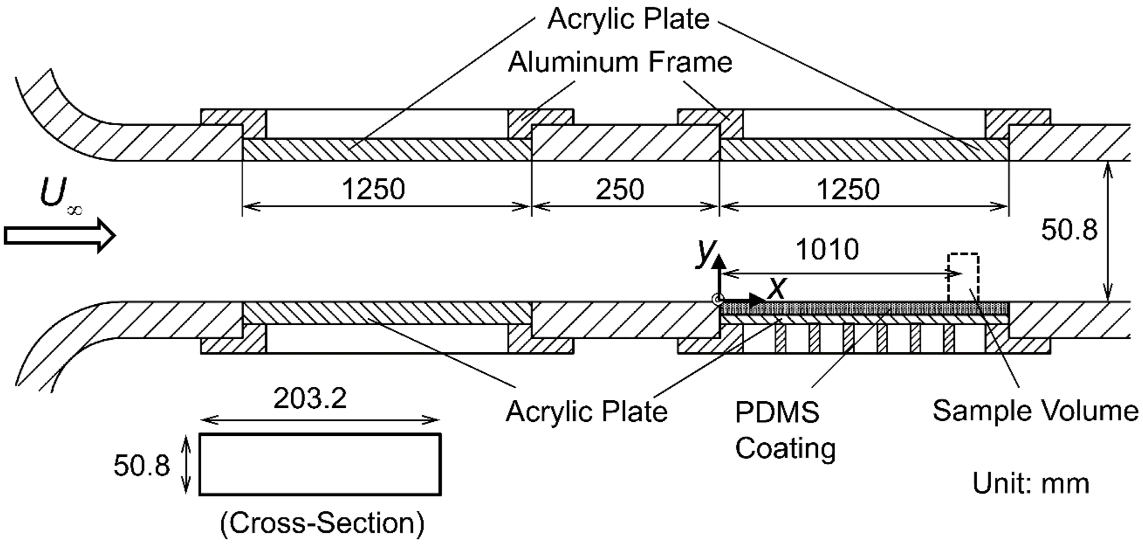

(b)

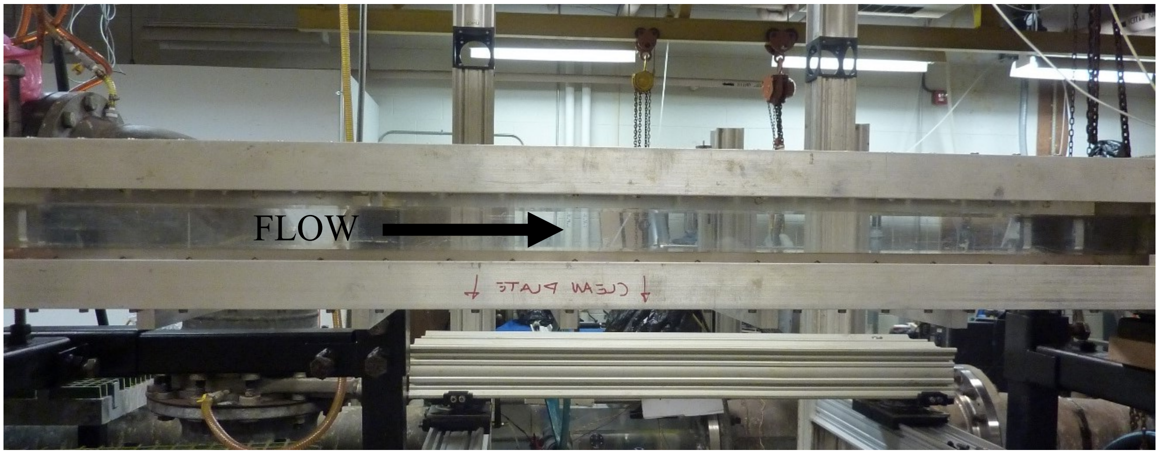

FIGURE 3.1(a) Channel dimensions and location of sample volume (drawn not to scale). (b) A photo of the downstream half of the test section.

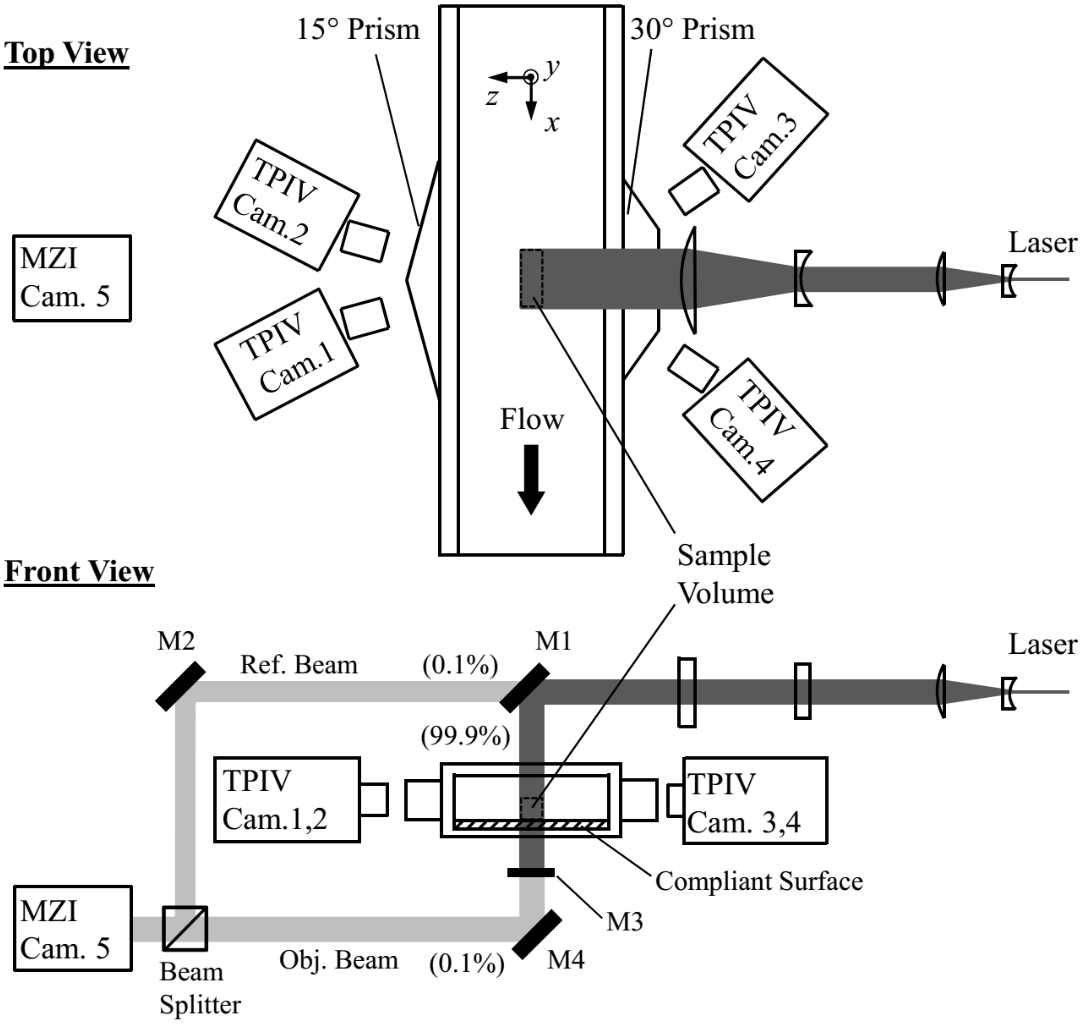

FIGURE 3.2 Optical setup of the combined TPIV/MZI system.

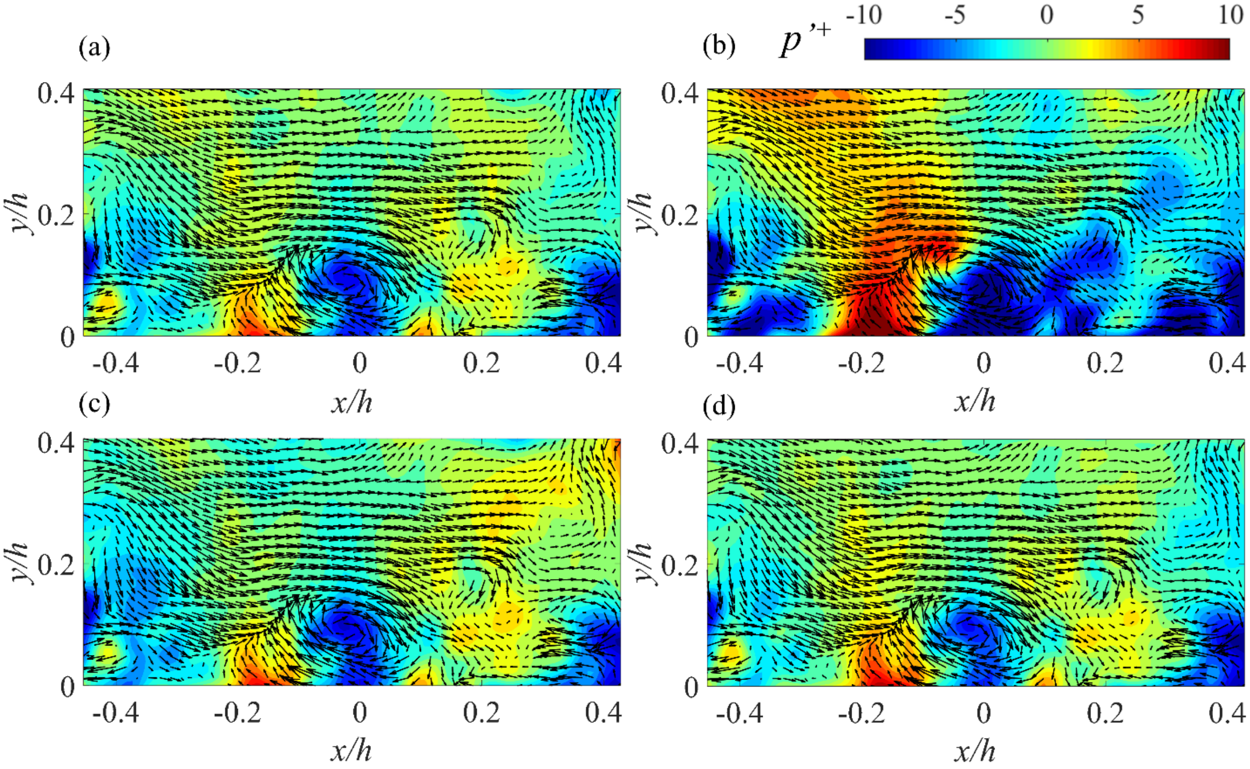

FIGURE 3.3 Pressure calculated from under-resolved experimental data. ($D_x^+ = D_y^+ = D_z^+ = 80$) Computed instantaneous pressure field combined with velocity vectors calculated using: (a) Omni3D-WP, (b) Omni2D, (c) PPE-Omni2D, and (d) PPE-Ber1.

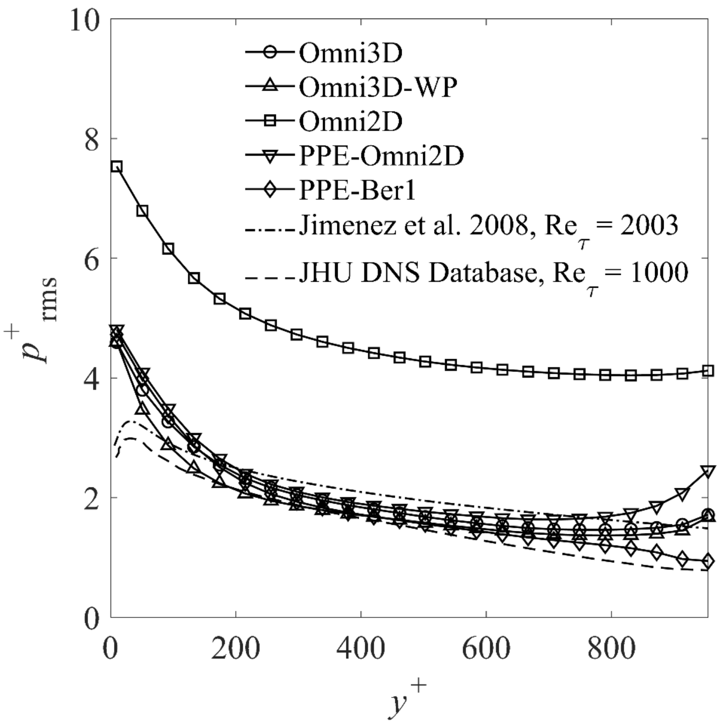

FIGURE 3.4 Profiles of the experimental ($D_x^+ = D_y^+ = D_z^+ = 80$) temporal RMS pressure fluctuations calculated using several integration methods in comparison to available DNS data.

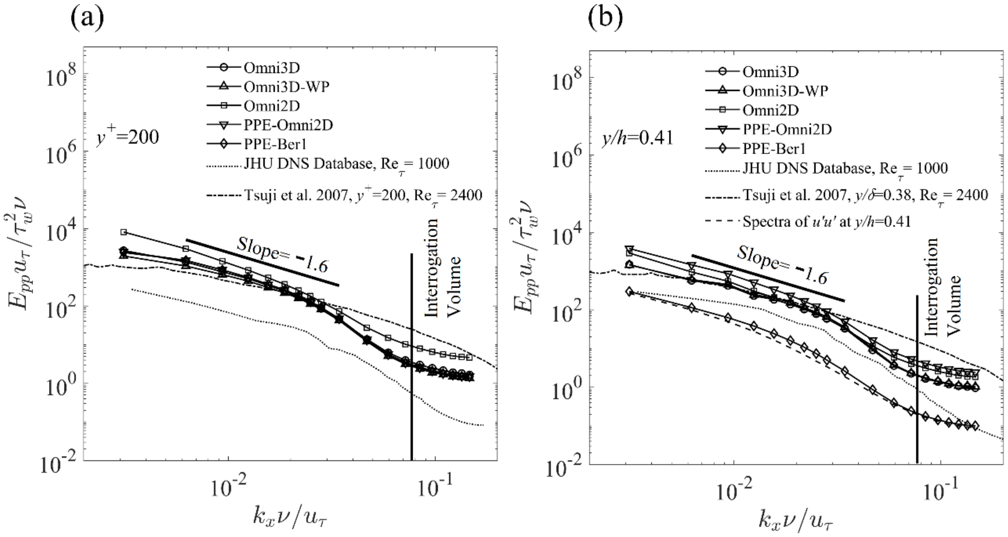

FIGURE 3.5 Ensemble and spanwise-averaged streamwise pressure spectra calculated from experimental data using several methods in comparison to the experimental wall data of Tsuji et al. (2007), DNS data of Kim et al. (1999) and the JHU DNS data (Graham et al. 2016). Elevations are: (a) y^+=200, and (b) *y/h*=0.41, at the top surface.

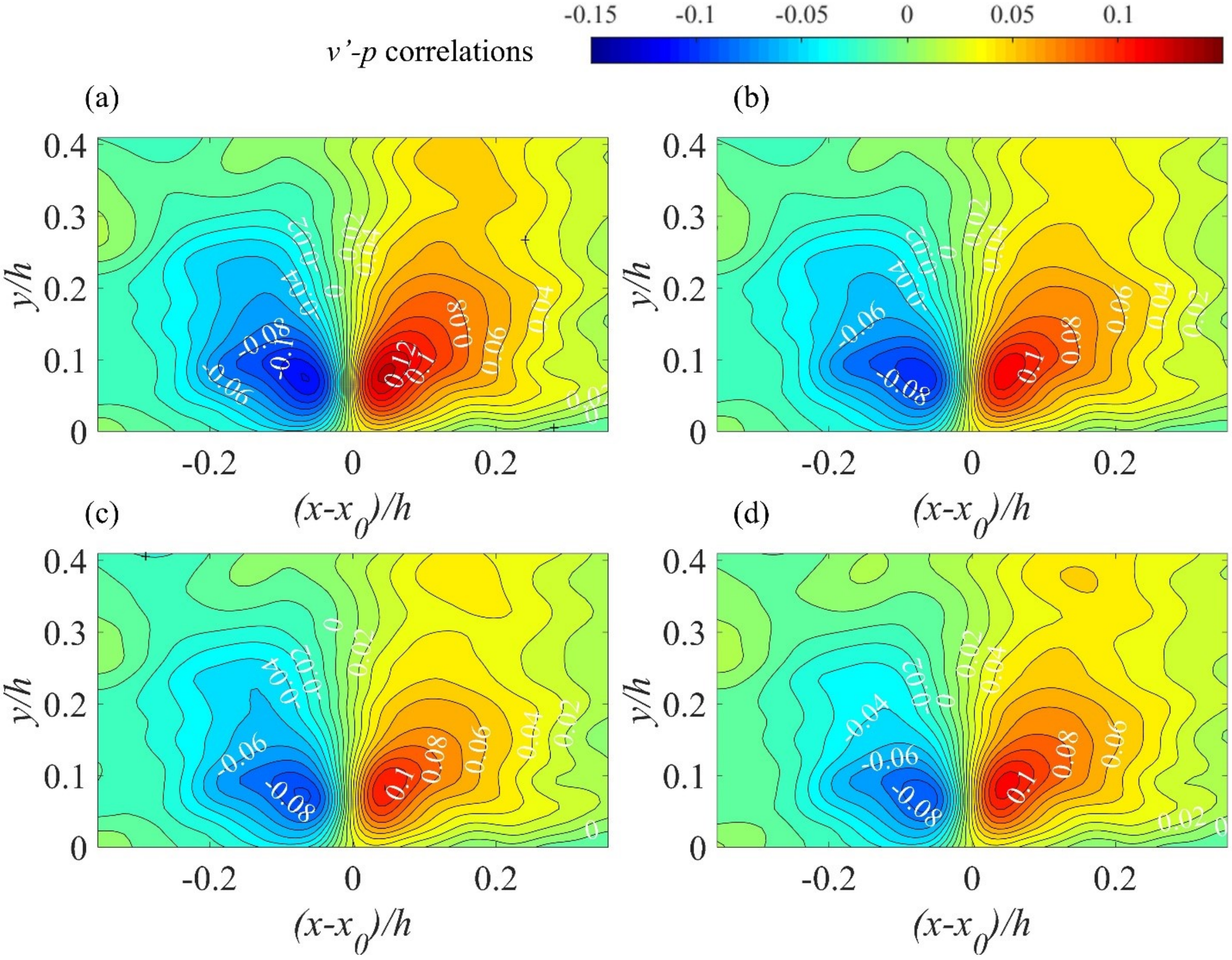

FIGURE 3.6 Spatial correlation of wall-normal velocity fluctuation and near-wall pressure (*y/h*=0.05) calculated using: (a) Omni3D-WP, (b) Omni3D, (c) PPE-Omni2D, and (d) PPE-Ber1. The incremental increase between lines: 0.01.

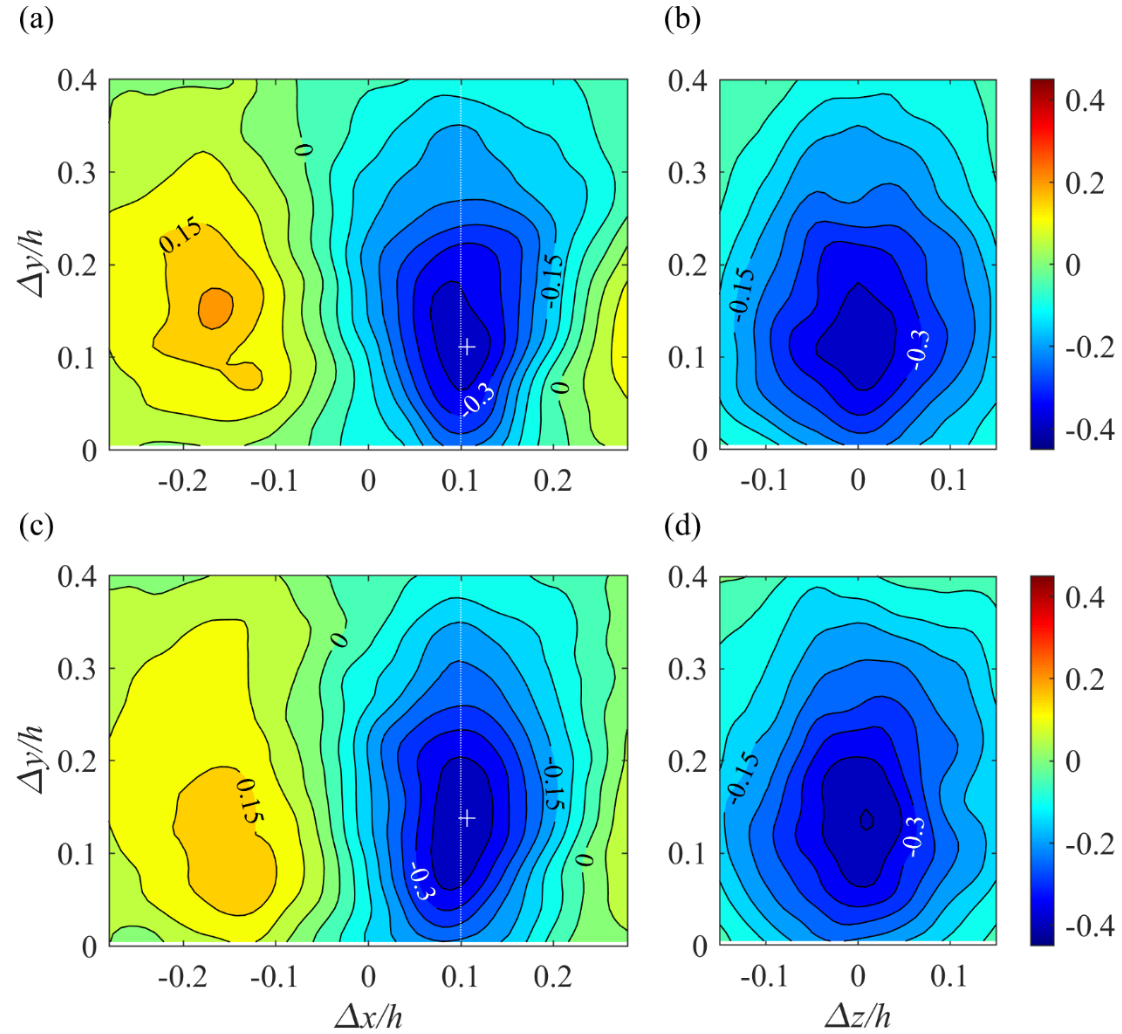

FIGURE 3.7. Conditional correlations between the detrended and high-pass filtered (at $\omega h/U_0$=4.3) deformation at (0, 0) and pressure, based on (a, b) strong positive deformation ($d>d_{RMS}$), and (c, d) strong negative deformation ($d<-d_{RMS}$). The y-z planes in (b, d) correspond to $\Delta x/h$=0.1, which is marked by dashed lines in (a, c). The position of peak value is indicated by a +.

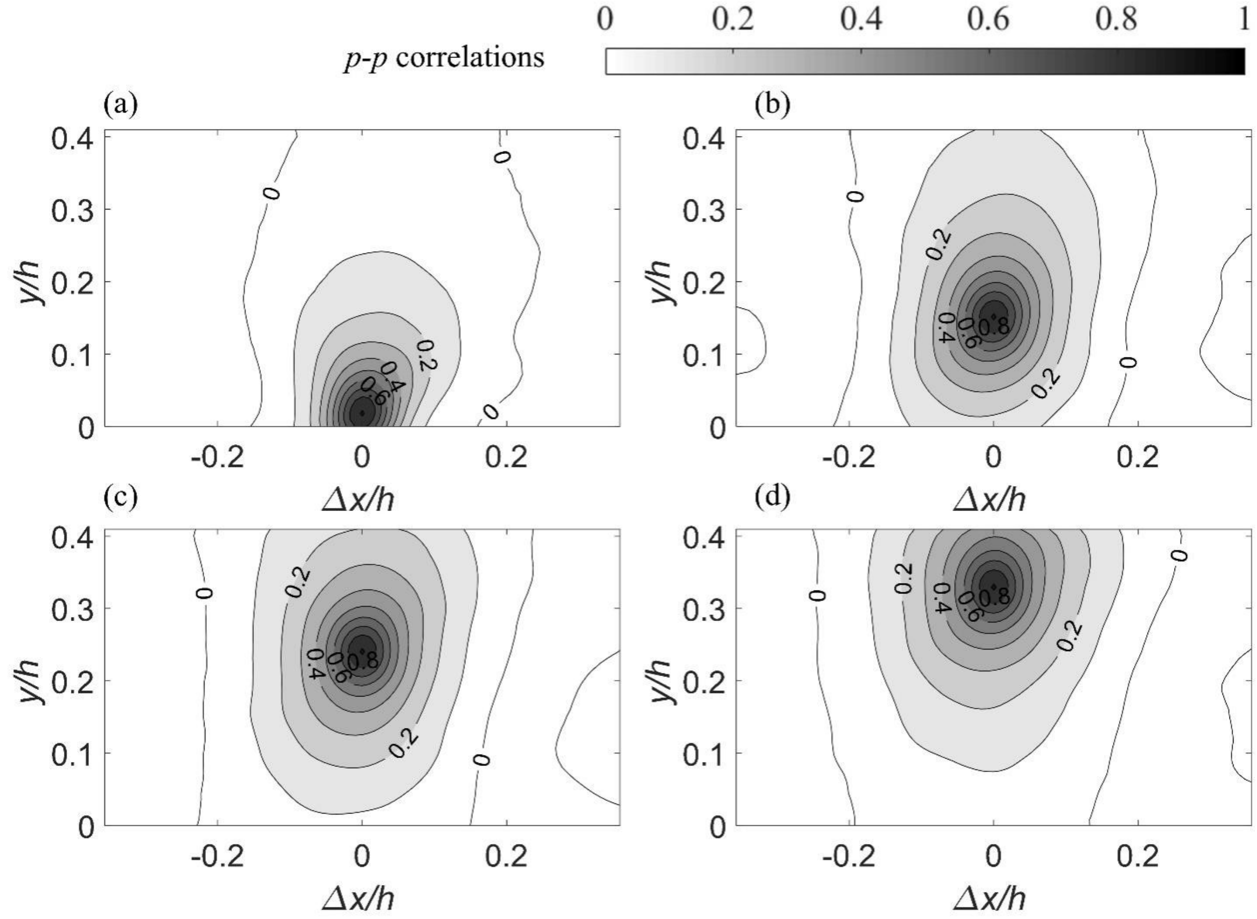

FIGURE 3.8. Sample two-point correlations of pressure ($R_{p,p}$) with reference point located at (a): y_0=0.02*h*; (b) y_0=0.15*h*; and (c) y_0=0.24*h*; (d) y_0=0.33*h*.

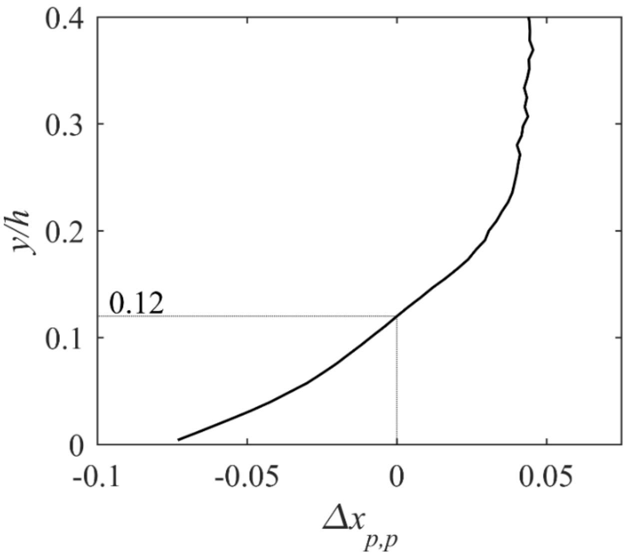

FIGURE 3.9. Profile of the average streamwise offset between the pressure at y_0/h=0.12 and that at other elevations. The values are calculated from the amplitude-weighted argument of pressure-pressure cross-spectrum.

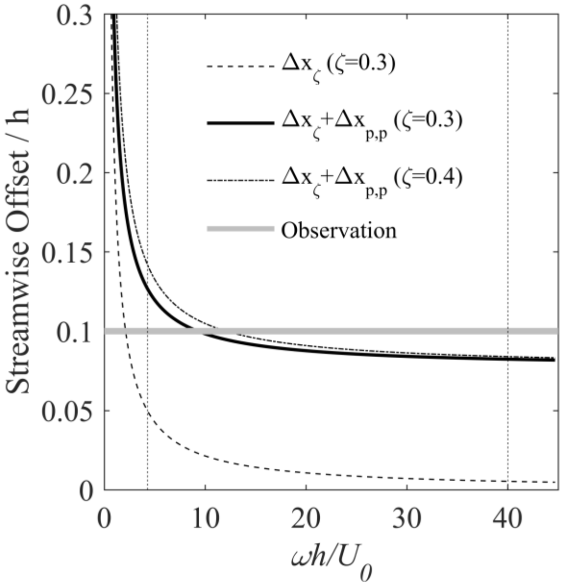

FIGURE 3.10. A comparison of the measured streamwise offset of the deformation-pressure correlation peak to that caused by damping only, and the combined effects of hydrodynamic phase lag and material damping. The latter is provided for two values of loss tangent.

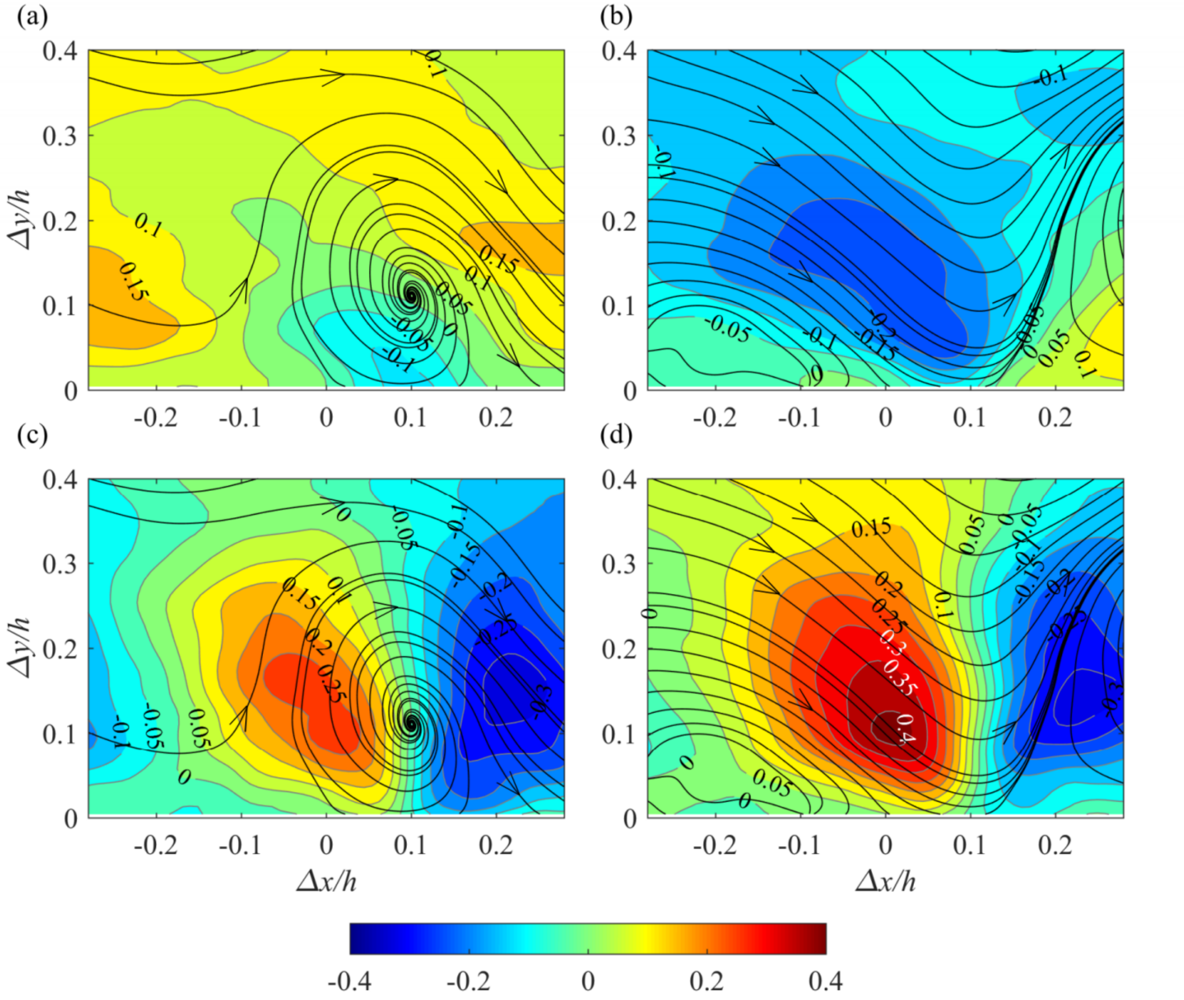

FIGURE 3.11. Conditional deformation-velocity correlations at (Δ*x*, Δ*y*, Δ*z*=0) for positive (left column) and negative (right column) deformations: (a) $R_{d,u}|_{d>dRMS}$, (b) $R_{d,u}|_{d<\text{-}dRMS}$, (c) $R_{d,v}|_{d>dRMS}$, (d) $R_{d,v}|_{d<\text{-}dRMS}$. The streamlines show the corresponding conditionally averaged flow fields.

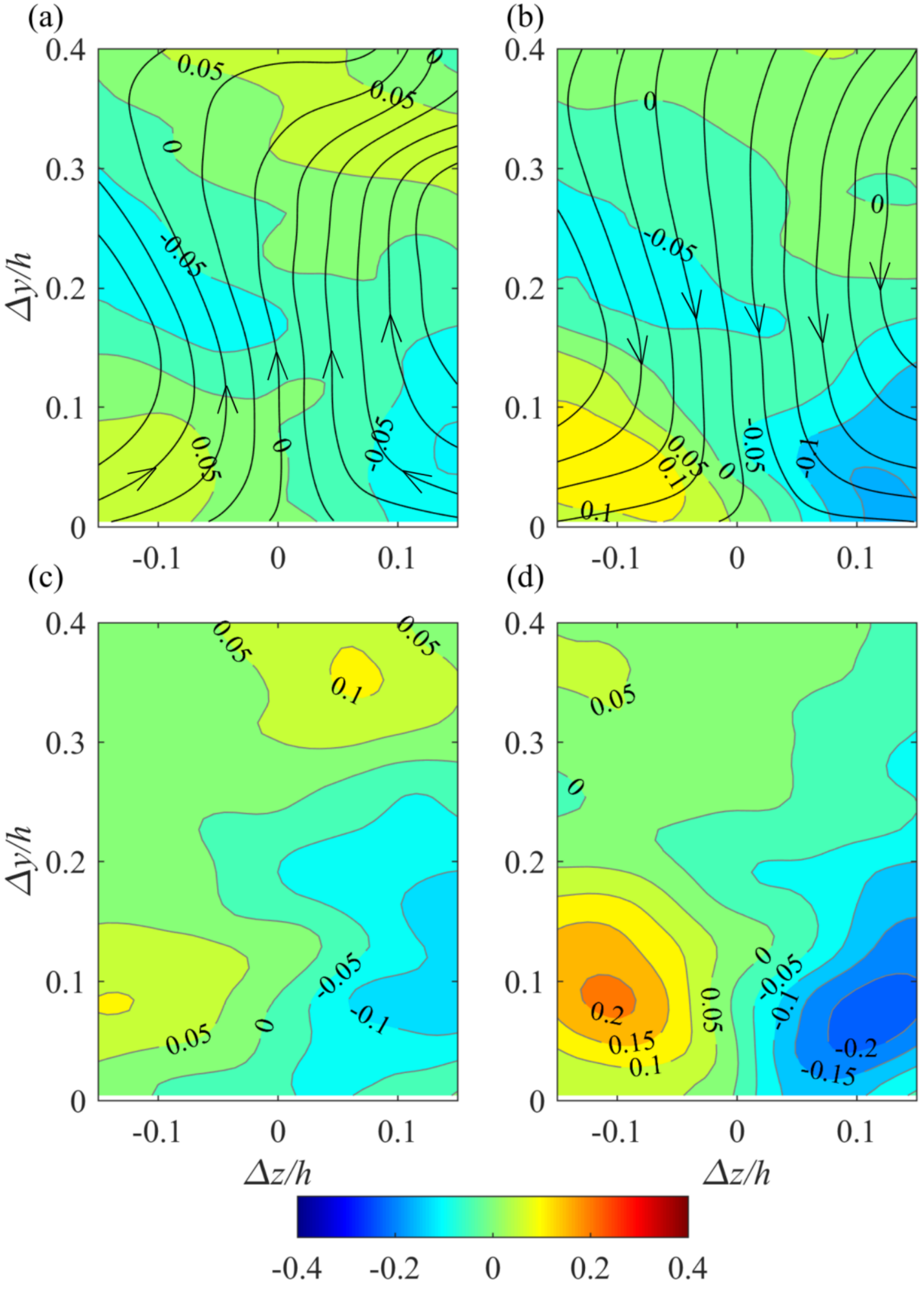

FIGURE 3.12. Conditional deformation-spanwise velocity correlations for positive ($R_{d,w}|_{d>dRMS}$, left column) and negative ($R_{d,w}|_{d<-dRMS}$, right column) deformations. Top row (a, b): $\Delta x=0$; and bottom row (c, d): $\Delta x=0.1h$. The streamlines show the corresponding conditionally averaged flow fields.

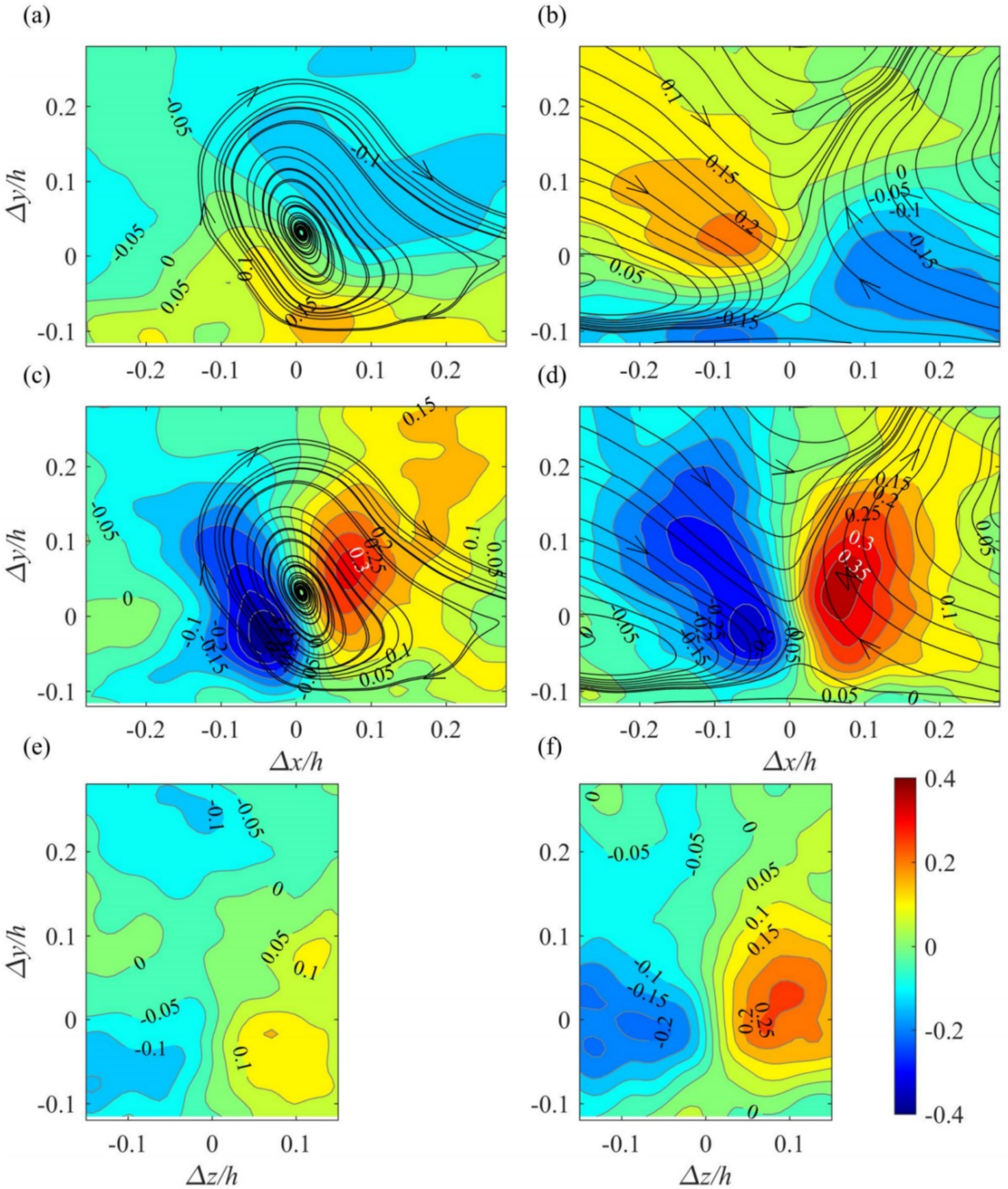

FIGURE 3.13. The pressure-velocity conditional correlations with reference pressure located at (0, 0.12*h*, 0). (a) $R_{p,u}|_{p<-pRMS}$, (b) $R_{p,u}|_{p>pRMS}$, (c) $R_{p,v}|_{p<-pRMS,}$ (d) $R_{p,v}|_{p>pRMS}$, (e) $R_{p,w}|_{p<-pRMS}$, and (f) $R_{p,w}|_{p>pRMS.}$ (a-d) show the (Δ*x*, Δ*y*, Δ*z*=0) plane. (e and f) show the (Δ*x*=0.1*h*, Δ*y*, Δ*z*) plane. The same color scale applies to all plots.

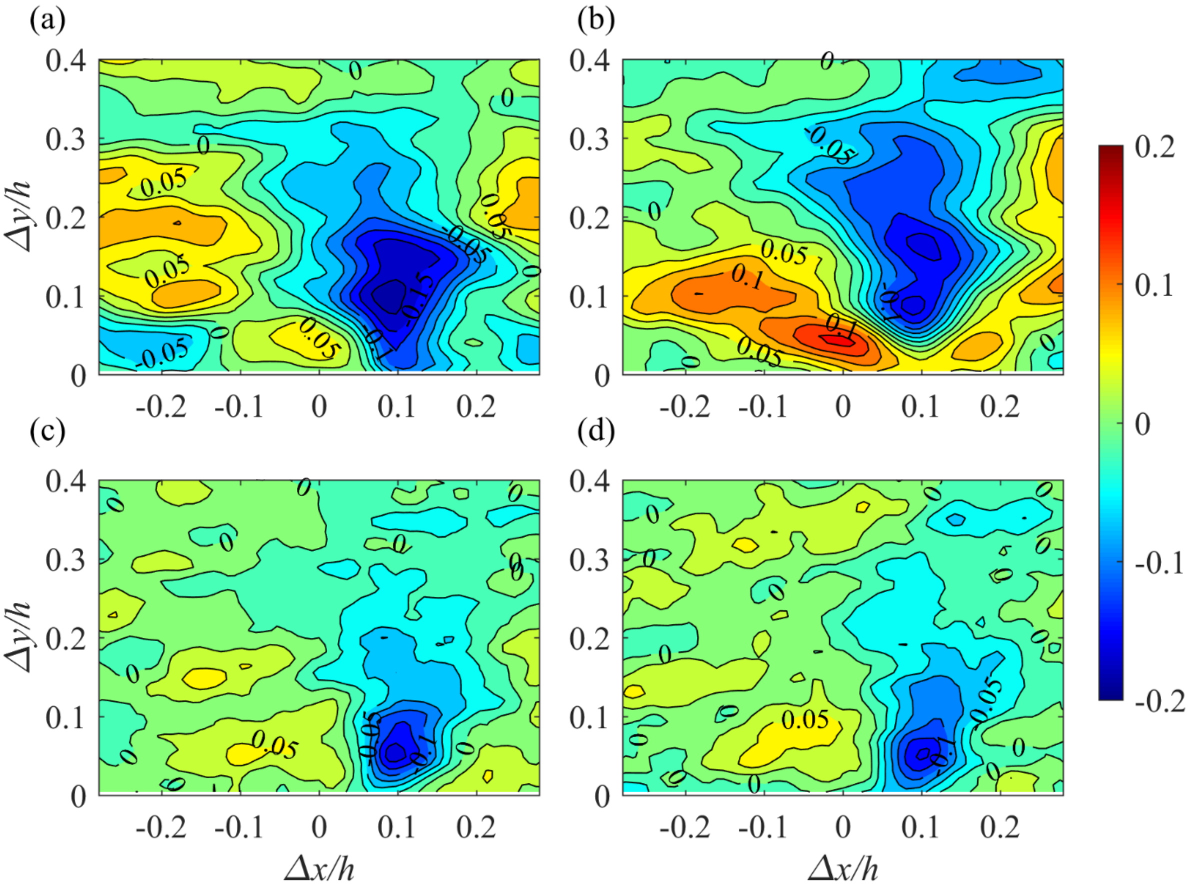

FIGURE 3.14. Conditional deformation-spanwise vorticity correlations, and (c, d) corresponding deformation-λ_2 correlations: (a) $R_{d,\,\omega z'}|_{d>dRMS}$, (b) $R_{d,\,\omega z'}|_{d<-dRMS}$, (c) $R_{d,\,\lambda 2}|_{d>dRMS}$ and (d) $R_{d,\,\lambda 2}|_{d<-dRMS}$.

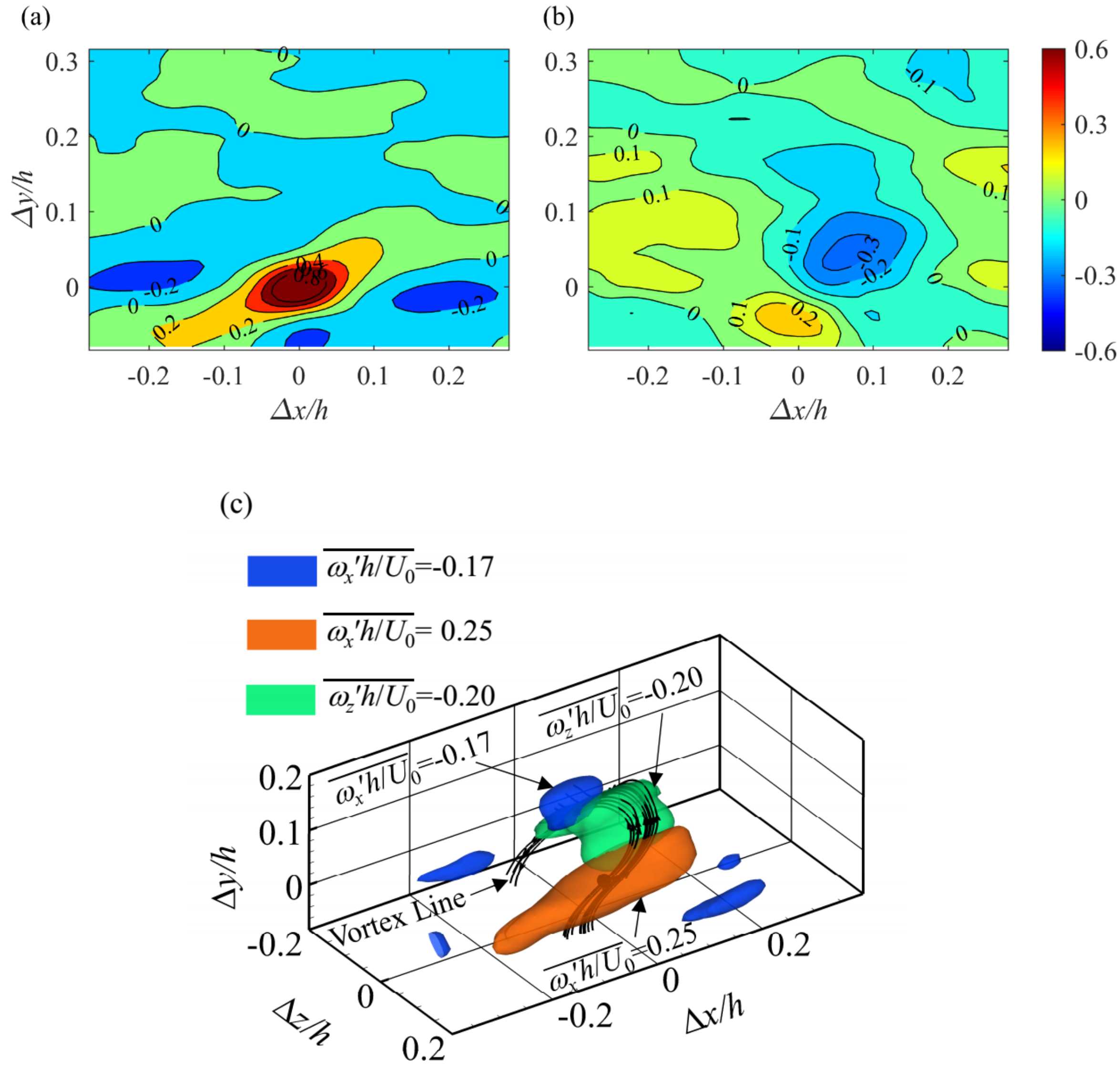

FIGURE 3.15. Results of analysis conditioned on $d(0,0)>\sigma_d$ and $\omega_x'(0, 0.08h, 0.05h)>0$: (a) d-ω_x' correlation in the $\Delta z/h$=0.05 plane; (b) d-ω_z' correlation at $\Delta z/h$=0; (c) iso-surfaces of $\overline{\omega_x' h/U_0} = -0.17$, $\overline{\omega_x' h/U_0}$ =0.25 and $\overline{\omega_z' h/U_0}$ =-0.20, along with the corresponding vortex lines

Chapter 4 Turbulent boundary layer over a softer compliant wall

As discussed in chapter 3, since the magnitude of compliant wall deformation (~43 nm) is much smaller than a wall unit (11 μm), no significant difference is observed between the rigid smooth wall turbulent boundary layer and compliant wall turbulent boundary layer regarding mean velocity profiles and turbulent statistics (Zhang et al. 2017). To ensure two-day couplings, either a softer compliant surface or a higher flow speed is required. Limited by the capability of the current water tunnel, increasing the flow speed to close to 17 m/s (the shear wave speed of previous material) could not be done. Thus, a softer compliant surface whose shear wave speed is comparable to the maximum flow speed of the water tunnel is needed. In this chapter, we will talk about the construction of a softer compliant surface and subsequent experimental measurement of the deformation and the turbulent boundary layer velocities.

4.1 Design of experimental conditions and construction of softer compliant surface

Following Zhang et al. (2017), a Matlab-based code for calculating the response of visco-elastic material based on the Chase (1991) model has been used for determining the desired material properties, including the Young's and shear Moduli, loss coefficient, and coating thickness. Our objectives have been to, (i) have a deformation amplitudes of a few wall units, (2) a range of wavenumbers that falls within a convenient field of view of the imaging systems (~70 mm), and (3) a peak response frequency of less than 2 kHz allowing full use of the camera resolution. Multiple iterations have led to the selection of a material whose response to excitation by pressure with a constant amplitude of ρu_τ^2 is portrayed in the wavenumber-frequency spectrum presented in figure 4.1.

Here, ω is the frequency multiplied by 2π, k is wavenumber, l_0 is the thickness of the coating, and C_t is the material shear speed, E is the Young's Modulus, ρ is the fluid density, and u_τ is the boundary layer friction velocity discussed before. The frequency and wavenumber are presented both in dimensional and dimensionless forms, and the amplitude is normalized by $\rho u_\tau^2 l_0/E$. Note that this spectrum assumes a uniform excitation amplitude. And constant material properties. Further analysis later in this paper accounts for the variations in properties and pressure fluctuation amplitude with frequency. Based on this prediction, at a free stream velocity of 6 m/s, friction velocity of 0.21 m/s, and E~158 kPa (based on the measurements below figure 4.2), the maximum deformation peak is around 24 μm, several times larger than the corresponding wall unit (~5 μm). Hence, provided the material is excited at the proper frequency and wavenumber, a two-way coupling of the flow with the deformation should be expected. Furthermore, for a layer thickness of 5 mm, the wavelength of peak response ($3l_0$) is 15 mm, and the corresponding frequency is 480 Hz. Hence, a field of view of 70×35 mm^2 and an image acquisition rate of 2 kHz should be sufficient to resolve the 2D surface deformation.

To facilitate the characterization of the surface deformation using Mach-Zehnder Interferometry (MZI) (Zhang et al. 2017), we have opted to use a silicone-based transparent coating made of Polydimethylsiloxane (PDMS). The material properties are then varied/controlled by mixing the PDMS with a silicone gel. The compliant surface is manufactured by mixing Dow Corning Sylgard™ 184 (PDMS) and Sylgard™ 527 (gel), Using a PDMS to gel mass ratio of 1:7.5, the data provided by Palchesko et al. (2012) suggests that the storage modulus of this material should be around 80 kPa. Samples of this material have been manufactured and then sent to the Naval Surface Warfare Center, Carderock Division to measure their properties at the relevant range of frequencies for varying frequencies (Technical report No. TR180613-02). The dynamic tests are performed with a frequency range of 0.01 Hz to 1000 Hz at a temperature from -50 °C to +50 °C in a 5 °C step. The complex elastic modulus, E^*, as a function of the angular frequency ($\omega=2\pi f$) can be determined using

$$E^*(\omega) = E_0 \frac{i\omega^m \Gamma(1-m) e^{-i(1-m)\pi/2}}{[1+(i\omega\tau)^\alpha]^\beta} + E_{\infty}\{1 - \frac{1}{[1+(i\omega\tau)^\alpha]^\beta}\}, \tag{4.1}$$

which has six measured temperature-dependent, Havriliak-Negami coefficients, namely E_∞, E_0, m, τ, α, and β (Hartman et al. 1993). Based on the measured values (E_∞=556 kPa, E_0=158 kPa, m=0.0029, $\tau=2.57\times10^{-4}$, α=0.739, $\beta=6.54\times10^{-5}$), the static storage modulus of this material is E_0=158 kPa, and the shear speed estimated using $C_t=\sqrt{E/2(1+\nu_p)\rho_s}$, is 7.85 m/s, where ν_p=0.4995 is the Poisson Ratio. Figure 4.2a summarizes the experimental measurements of storage modulus and loss tangent for this material as a function of frequency. This compliant surface is softer than the one described in Zhang et al. (2017), where the storage modulus is ~0.94 MPa, and the sheer speed, 17 m/s. We also performed a dynamic test of the material's properties using the facility of Johns Hopkins University (Rheometrics Solids Analyzer, RSA II). The facility, which has been used for measuring the properties of the previous compliant material, is capable of measuring dynamic modulus from 0.1 Hz to 20 Hz. The measured storage modulus is about 120 kPa for the same temperature, a little smaller than the result from the Surface Warfare Center, Carderock Division. To compare, the measured loss tangent together with a loss tangent of the previous material and others are provided in figure 4.2b. The loss tangent measured is apparently smaller than the previous material.

There are serval other ways to make a softer compliant surface. Lee et al. (1993a, b) constructed a compliant surface by adding 91 percent by weight of 100 cSt oil (Dow-Corning 200 series Silicone oil) to 9 percent of PDMS. The shear modulus measured is found to be 230 Pa. The corresponding peak-to-valley surface displacement is 1.67 μm and the RMS value is

0.32 µm at a Reynolds number of R_θ=900($R_\theta = \frac{U_0\theta}{\upsilon}$, θ is the boundary-layer momentum thickness). Recently, gelatin is used by Huynh et al. (2019) to measure the spatial-temporal response of a compliant-wall, turbulent boundary layer system to dynamic roughness forcing. The Young modulus is found to be 2.4 kPa, which is consistent with the material used by Gad el Hak (1986).

A special 5 mm wide molding chamber which already contains the acrylic wall of the water tunnel has been constructed. The mixture is poured into this chamber while it is kept below atmospheric pressure (87.5 kPa) to minimize the formation of bubbles, and allowed to cure at room temperature (~25 °C). The typical curing time is about 48 hours. The dimension of the compliant coating is 583×177×5 mm^3 in length, width, and thickness, respectively. The refractive index of this material measured using a refractometer (Waterproof Digital Refractometer Brix) is 1.406, and its density, as proved by the manufacturer and measured by the Naval Surface Warfare Center, Carderock Division, is around 0.855 g/cm^3. To hold the compliant surface attached to the water tunnel window, the periphery of the (50.8 mm thick) acrylic window has a 12.7 mm wide overhanging rim and threaded holes (figure 4.3a,b). We have not used any chemical bonding between the compliant material and the acrylic to prevent potential distortion of MZI images. It should be noted that there are many ways to generate chemical bonding between the acrylic wall and the compliant surfaces. The author tried using a primer (Dow Corning PR-1204 RTV prime coat clear) about 1 μm in thickness. The primer worked well, however, unsure about the optical properties of the primer, it’s not chosen for the current experiment. The current design works effectively for flow speeds up to 7 m/s, but have partially peeled off after serval hours at 5.9 m/s, requiring repeated installations. A separate mold with a thickness of 3.14 mm has been used for preparing samples for testing the material properties.

4.2 Test Facility and MZI Experimental Setup

The experiments have been performed in a new water tunnel extension/bypass of the Johns Hopkins University refractive index-matched test facility. A schematic of this water tunnel is presented in figure 4.4. The working fluid is an aqueous sodium iodide (NaI) solution, whose refractive index (1.4876) is matched with that of acrylic, but not that of the compliant material. The density of the fluid is $\rho = 1.86\times10^3$ kg/m^3 and its dynamic viscosity is $\nu = 1.1\times10^{-6}$ m^2/s. The flow in this system is driven by two pumps. The main driver is either an axial waterjet pump or a replica of an axial compressor connected to a 60 Hp motor. These devices have been subjects for several studies by themselves (Tan et al. 2015, Li et al. 2017, Huang et al. 2017, 2019). Additional power is provided by a 20 Hp auxiliary axial pump. The highlighted new extension consists of a long diffuser, a 406×348 mm settling chamber containing screens and a honeycomb, a nozzle with an area ratio of 4.6,1, a test section with windows on all sides, and another diffuser expanding back to original 30.5 cm pipe. The size of the test section is 838×152×203 mm^3 in the streamwise(x), wall-normal(y) and spanwise(z) directions, respectively. It consists of a stainless steel frame and 50.8 mm thick acrylic windows. The present experiments have been performed at speed ranging between 1.2 and 6.9 m/s, the latter being well below the maximum level. The 5 mm thick compliant surface is embedded in the bottom window. The boundary layer is tripped upstream of this surface using a series of 5 mm high grooves (figure 4.3a,c), which are similar to those used in Ling et al. (2016) to establish a fully developed turbulent boundary layer. The velocity and deformation measurements are performed 496 mm downstream of the beginning of the compliant surface and 508 mm downstream of the tripping grooves.

Figure 4.5 is a sketch of the setup for measuring the wall deformation using Mach-Zehnder interferometry (MZI). Details on the data analysis procedures of associated uncertainty are provided in Zhang et al. (2015). The beam of a high-speed Nd, YLF laser (Photonics model DM60-527) is attenuated by an ND 0.9 filter and then split into reference and object beams. The object beam is expanded to a diameter of about 10 cm and directed across the test section and the compliant wall using 20 cm diameter mirrors and lenses. This beam is then reduced to about 2 cm, and directed to the camera. Using 10 cm diameter lenses and mirrors, the reference beam bypasses the test section and is then combined with the object beam by a non-polarizing beam splitter before illuminating the camera. The optical path lengths of the two beams are matched by varying the path of the reference beam until the interference fringes appear (figure 4.6a). The 2016×1012 pixels interferograms are recorded at 2 kHz by a PCO.dmax camera, resulting in a field of view of 70×35 mm^2 in the x and z directions, respectively. As discussed in Zhang et al. (2015), the fringes are enhanced using spatial correlation-based filtering, and the phase distributions are measured directly from the enhanced images. In the present data, the typical fringe spacing is 0.35 mm, defining the lateral resolution, but the uncertainty in the wall-normal direction is about 20 nm, i.e. ranging between 2.0 to 0.1% as the deformation increases from 1 to 20 μm. A total of 7000 fringe patterns are captured for each flow condition, namely at six freestream velocities of 1.2, 1.9, 3.2, 4.5, 5.3 and 5.9 m/s.

A sample raw fringe pattern is shown in figure 4.6a, and the enhanced image, using the correlation-based fringe enhancement method (Zhang et al. 2015, 2017) is presented in figure 4.6b. The latter still has a few noisy spots with fringe discontinuity, preventing the use of simple phase unwrapping to determine the phase distribution. For these regions, the phase unwrapping is performed using a branch-cut method, i.e. the noisy spots are circumvented (Goldstein et al. 1988; Ghiglia & Pritt 1998), as described in Zhang et al. (2017). Once the phase distribution is determined over the entire image, the deformation map is calculated by spatial differentiation of adjacent iso-phase lines. Samples of instantaneous deformation for U_0 ranging between 1.2

to 5.9 m/s, corresponding to $E/\rho U_0^2$ ranging from 59 to 2.4 are provided in figure 4.7. Several trends are evident. First, in agreement with the Rosti and Brandt (2017), at low speed, the typical surface pattern is aligned in the streamwise direction, but with increasing velocity, the waves become preferentially aligned in the spanwise directions. Second, the amplitude of deformations increases rapidly with decreasing $E/\rho U_0^2$. A corresponding plot quantifying this observation is presented in figure 4.8. It shows both the temporal root mean square deformation ($d_{t,\mathrm{RMS}}$) at each point and then averaged over the entire field of view, the spatial root mean square of deformation ($d_{s,\mathrm{RMS}}$) averaged over time, as well as the time-average of the positive peak deformation (amplitude) in each realization. The values of $d_{t,\mathrm{RMS}}$ and $d_{s,\mathrm{RMS}}$ are also provided in Table 4.1. The average peak increases from a submicron value at $E/\rho U_0^2 = 59.0$ to 18 μm at $E/\rho U_0^2 = 2.4$. As will shown in the next section, the corresponding wall units decrease from 21 μm to 5 μm. Hence, while one-way coupling between deformation and flow might be expected for $E/\rho U_0^2 = 59.0$, the two-way coupling is likely to occur for $E/\rho U_0^2 = 2.4$. However, as will be shown later, low levels of two-way coupling occur also at the lowest velocity.

Third, the length and width of deformation peaks appear to increase with velocity (decreasing $E/\rho U_0^2$). These trends are elucidated in figure 4.9 using streamwise wavenumber-frequency spectra, $E_{dd}(k_x,\omega)$, where the amplitude is normalized by $[l_0 d_{t,\mathrm{RMS}}]^2/U_0$, k_x is the streamwise wavenumber, and ω is the frequency in rad/s. The scales on the right and top sides of each plot provide the corresponding dimensionless frequency ($\omega l_0/U_0$), and wavenumber ($k_x l_0/U_0$). At this point, we opt to use l_o as the length scale instead of e.g. the boundary layer thickness as a basis of comparison with the Chase (1991) model (figure 4.1). The vertical lines mark the wavenumber corresponding to $3l_0$, the range where the model predicts a peak response (figure 4.1). After subtracting the mean value and detrending the data along each streamwise line (similar to Zhang et al. 2017), these spectra are calculated in the streamwise direction and time for each spanwise location using Fast Fourier Transform (FFT) and then averaged over all spanwise planes. Each plot clearly shows an advected band with a phase speed of about $0.66U_0$, as illustrated by the dashed lines in all the plots. This speed is slightly lower than the slow-mode reported by Kim and Choi (2014) and in our previous experiment for a harder material (Zhang et al. 2017), namely $0.72U_0$. However, unlike our previous experiment, the present spectra do not show deformations traveling at the freestream velocity. In addition, at low speeds, the k_x-ω spectra have a band with high frequency and a very low wavenumber, which will be discussed later.

Table.4.1 Measured Boundary layer parameters and RMS values of compliant wall deformation, velocity, and acceleration.

	U_0 (m/s)	1.2	1.9	3.2	4.5	5.3	5.9
Stiff Wall	u_τ(m/s) from log fit	0.0528	--	0.1098	--	--	0.2009
	δ_ν(μm) from log fit	20.8	--	10.0	--	--	5.47
	Re_τ from log fit	1440	--	2795	--	--	4931
	u_τ(m/s) from viscous sublayer	0.0507	--	0.1161	--	--	0.2046
	δ_ν(μm) from viscous sublayer	21.7	--	9.48	--	--	5.38
	Re_τ from viscous sublayer	1383	--	2955	--	--	5022
Compliant Wall	u_τ(m/s) from log fit	0.0526	--	0.1216	--	--	0.2110
	δ_ν(μm) from log fit	20.9	--	9.08	--	--	5.21
	Re_τ from log fit	1435	--	3095	--	--	5179
	$E/\rho U_0^2$	59.0	23.5	8.3	4.2	3.0	2.4
	u_τ^3/ν (m/s^2)	132	--	1423	--	--	7786
	$d_{t,RMS}$(μm)	0.084	0.17	0.62	1.4	1.7	2.8
	$d_{s,RMS}$(μm)	0.071	0.15	0.51	1.3	1.6	2.7
	$d_{t,RMS}^+$	0.004	--	0.06	--	--	0.54
	$\dot{d}_{t,RMS}$(m/s)	2.3e^{-4}	2.2e^{-4}	8.3e^{-4}	2.1e^{-3}	2.6e^{-3}	4.4 $^{-3}$
	$\dot{d}_{t,RMS}^+$	0.004	--	0.007	--	--	0.021
	$\ddot{d}_{t,RMS}$(m/s^2)	1.67	1.54	3.95	10.4	12.2	23.9

Corresponding plots of $E_{dd}(k_z,\omega)$ are presented in figure 4.10. Here, the FFTs are calculated in the spanwise directions and then averaged over all the streamwise planes. In this case, there is no evidence of an advection band, as expected. The primary spectral peaks have low wavenumbers that do not seem to vary significantly with velocity, but their frequency does increase and remains centered at around $\omega l_0/U_0 \sim 1.7$. In addition, at low velocities, the k_z-ω have another low wavenumber, high-frequency spectra band, which seems to coincide with the main band as the frequency of the latter shifts to higher values with increasing velocity. Finally, figure 4.11 shows the time-averaged two-dimensional spatial spectra, namely $E_{dd}(k_x, k_z)$. In this case, the results are normalized by the time-averaged spatial RMS values (after subtracting the spatial mean and detrending), which are also given in Table 4.1. Again, the spectra contain two peaks, which are distinct at low speeds, but the boundary between them becomes fuzzy with increasing velocity. The first peak is located at $k_z=2\pi/3l_0$ and very low k_x. The second peak seems to be centered at low k_z and k_x slightly higher than $2\pi/3l_0$, the predicted location of the peak in the Chase (1991) model. Otherwise, the (k_x,k_z) spectra do not seem to vary significantly with velocity. This trend implies that the wavelengths of the surface deformation in both directions are not associated with the flow scales. Hence, using the complaint wall thickness as a reference length scale is justified. The velocity affects the amplitude of these waves and their streamwise advection speed.

The next discussion compares the one-dimensional temporal spectra of deformation to predictions by two one-dimensional linear models, namely those of Chase (1991), and Benschop et al. (2019). The experimental results for all the present speeds are presented in figure 4.12. Figure 4.12a shows the results for the entire range of measured wavenumbers, and figure 4.12b covers only the advected bands, i.e. the spectral range corresponding to advection speeds varying between 0.46 to $0.86U_0$, as illustrated in figure 4.9a. These spectra are calculated for every physical point in the sample area (after subtracting the mean value and detrending) and then spatially averaged. The frequency is normalized by U_0/l_0, and consequently, consistent with the trend evident in figure 4.9, all the main spectral peaks collapse to $\omega l_0/U_0 \sim 1.7$. The energy is normalized by the corresponding RMS values, hence the normalized peaks do not differ substantially in magnitude. The existence of the previously-discussed high-frequency energy at low speeds is evident only in figure 4.12a, i.e. this range does not involve advected modes (as will be demonstrated later). In addition, all the spectra have a plateau at low frequency.

The Chase (1991) model (referred to subsequently as the Chase model) solves the one-dimensional Helmholtz Eqn. for the behavior of a viscoelastic layer with a given thickness, shear modulus and loss tangent, which can be frequency-dependent. The harmonic boundary conditions include flow-induced pressure and shear, but the model also accounts for the acoustic impedance of the fluid medium. The results are given as closed-form equations for the spatial distribution material deformation. The Benschop et al. (2019) model (referred subsequently as the Benschop model) also solves the Helmholtz Equation for given material properties, but the harmonic boundary conditions involve only pressure and shear stress. The results are also given as analytic expressions as a function of material properties, frequency, and wavenumber. Both models predict that the impact of pressure is higher than that of the shear, hence the present discussion focuses on the effect of pressure. In applying these models, one has to consider the frequency-dependent amplitude of pressure excitation by the flow, as well as the frequency-dependence of the material properties (figure 4.2). As noted before, the k_x-ω spectrum presented in figure 4.1, which has been used for guiding the selection of the present material assumes excitation at a uniform amplitude and fixed material properties. In this section, the analysis is repeated using both models, but this time it accounts for the characteristic pressure spectrum in a turbulent boundary layer as well as the measured frequency-dependent material properties. We have selected two pressure spectra for rigid wall boundary layers, the semi-theoretical one introduced by Goody et al (2004), and the one available from experimental wall pressure measurements by Tsuji et al (2007). Unfortunately, at the present time, we do not have wall relevant wall pressure spectra for a flow modulated by the compliant wall, which would be more appropriate for this discussion. The experimental pressure spectra provided in Zhang et al. (2017) for an-order-of-magnitude-harder complaint wall do not differ significantly from the rigid wall results as shown in Wang et al. (2019). In Benschop et al. (2019), the comparison is based on the experimental frequency spectrum. However, the dependence on wavenumber is modeled as advection at a frequency-dependent speed, which is assumed to decrease with increasing frequency. The present analysis is based on the measured k_x-ω spectra for two types of excitations, the first covers only the advected bands between 0.46 to $0.86U_0$ (figure 4.9a). The second analysis is based on the measured k_x-ω spectra filtered at $k_x<200$.

Figure 4.13 compares the two temporal pressure spectra used in the present analysis. In both cases, these spectra are Reynolds number-dependent. The Goody (2004) spectra are given as an empirically-determined analytic expression, and the Tsuji (2007) results are reproduced from the figures. They are both normalized using inner variables in figure 4.13(a). As is evident, with such scaling, differences exist mainly at low frequencies, but trends collapse at high frequency. The pressure spectra are also plotted in outer variables (figure 4.13b), showing a collapse at low frequency for Goody's pressure spectra. A comparison of wavenumber-frequency spectra obtained using the Chase and Benschop models is presented in figures 4.14a and b, respectively. Both are based on the measured frequency-dependent material properties and the Goody's (2004) amplitude at the present highest Reynolds number. For the Chase model, the effect of accounting for the frequency dependence of excitation and properties can be observed by comparing figure 4.14a to figure 4.1. As is evident, the primary difference occurs at low frequency, where the reduction in excitation amplitude (predominantly) and to a lesser extent the changing material properties, reduce the response. In figures 4.14a and b, both models show a response peak at a wavelength corresponding to three times the compliant coating thickness. However, the points of peak response differ, with the Benschop prediction having a higher frequency, and the Chase model showing a higher amplitude. However, the Benschop model has a broad area with an elevated response at low wavenumbers and high frequency, peaking around $\omega\nu/u_\tau^2 \sim 0.2$, although both have an elevated response in this range. Comparisons between the predictions of these models and the experimental results for the above-specified advection bands (figure 4.9a) at three different velocities are presented in figure 4.15a-c. The experimental data also consists only of the advected band. Corresponding results for excitation at low wavenumber (k<200 rad/m) are presented in figure 4.16a-c, with the experimental results also low-pass filtered at the same wavenumber. The (1D) model predictions are provided for three pressure spectra, namely a pressure field with a uniform amplitude of $p' = \rho u_\tau^2$, as well as the Goody (2004) and Tsuji et al. (2007) results (figure 4.13). The Goody spectra are calculated for the specific Re_τ, while for the Tsuji spectra we use the Re_τ=1435 spectrum for the present lowest speed, and the results for Re_τ=3490 for higher speeds. In all cases, the analysis also accounts for the frequency dependence of the material properties. The frequency is normalized by inner variables at the bottom x-axis, and the energy, by the total experimental RMS value (all frequencies and wavenumbers) and inner variables. Normalization of the frequency in outer variables are also provided in the top x-axis. Consequently, the comparison examines also the amplitude of the model predictions.

For the advected bands, figure 4.15 demonstrates that around the spectral peak there is a good agreement between the measured events and the predictions of both models when the pressure is based in the Goody (2004) spectra. At low frequency, the Benchop results are higher and they tend to flatten more than the Chase predictions. Yet, neither model flattens to the same extent as the experimental data. At high frequency, the Chase predictions are higher with either Goody or Tsuji spectra, but the difference is larger the latter. These trends are consistent with those of the k_x-ω spectra in figure 4.14. The magnitudes of the experimental high-frequency results appear to be more consistent with the Benchop model combined with Goody or Tsuji spectra. In all cases, predictions based on a flat pressure spectrum give significantly higher values than those based on experimental data.

As for the trends at low wavenumbers, figure 4.16 shows that the Benschop predictions are higher than those of the Chase model, consistent with the low k_x range in figure 4.14. Also as expected, results for the flat pressure spectrum are higher than predictions based on the Goody or Tsuji pressure spectra. In general, trends of the experimental results differ from those of either model with maxima centered at different frequencies. Furthermore, the experimental results have a plateau or increase at high frequency, depending on velocity, in contrast to the model predictions. In terms of magnitude, for most of the spectra, the measured levels seem to fall in the same range as the Benschop model, higher than those calculated based on the Goody pressure spectrum and lower than that based on the Tsuji spectrum. We have also compared the experimental spectra to the model predictions for spatially low-pass filtered spanwise waves (not shown). Similar to figure 4.16, trends of the measured and modeled spectra do not agree. Furthermore, since this mode is not caused by the flow, a prediction by the flat pressure should be better. The predictions show a peak response at high frequency. Careful examination of this peak indicates it's associated with deformation whose wavelength is $3l_0$ propagating at the shear speed.

To elucidate the surface pattern associated with each of the above-mentioned spectral ranges, figure 4.17 provides a series of sample images. The unfiltered data presented in figure 4.17a-c is selected to show that spanwise-propagating waves persist even at high velocities, although they are not as obvious as those at low speed when the amplitude of advected modes increases. Spatially low-pass filtered samples for k_x<200 are displayed in figure 4.17d,e, and f for low and high velocity, respectively. The spanwise-propagating wave, with its crest aligned in the streamwise direction, is dominant at low speed. Its frequency is high (figure 4.9a), centered around 3000 rad/s, and the dominant spanwise wavenumber is 400 rad/m (figure 4.11a), i.e. the corresponding advection speed is 7.5 m/s, very close to the measured shear speed for the compliant wall. It appears that this phenomenon involves shear waves propagating laterally and presumably reflected from the wall of the water tunnel. In the k_x-k_z spectra (figure 4.11a), the peak wavenumber of the spanwise shear wave corresponds to a wavelength of $3l_0$, consistent with the model predictions, although the temporal spectra (figure 4.16a) do not agree. When the velocity is increased (figure 4.17e,f), the surface structure becomes two dimensional with both streamwise and spanwise waves, but clearly, the spanwise waves are still evident. Band-pass-filtered samples focusing on the (previously discussed) advected bands, corresponding to advection speeds ranging between $0.46U_0$ to $0.86U_0$, are presented in figure 4.17g,h and i. These waves seem to have a lattice structure, but with a crest preferentially oriented in the spanwise direction. This spanwise preference seems to increase with velocity, in agreement with the low Reynolds number DNS results of Rosti and Brandt (2017). The characteristic wavelength of these waves is also about $3l_0$, consistent with both models and the measured advected band in the k_x-ω spectra (figure 4.9). In summary, the spanwise waves, which are dominant at low speeds, preferentially propagate at the shear speed and have a preferred wavelength of $3l_0$. These waves persist at high speed but appear to be overwhelmed by the advected mode, which also has a preferred wavelength of $3l_0$, but their propagation speed is affected by the flow. As the shear speed and tunnel velocity get closer, the amplitude of these waves grows rapidly.

4.3 Near wall turbulent flow over the softer compliant surface

First of all, to characterize the boundary layer thickness, a low-resolution stereo-PIV (SPIV) which can resolve the outer layer is performed. The setup of SPIV is illustrated in figure 4.18. The light source is an Nd-YAG laser (532 nm) whose beam is expanded to a 1 mm thick laser sheet. The image pairs are recorded using two Imprex ICL-B6640 interline transfer camera that has a 6600×4400 pixel array. Using a 105 mm lens and an extension tube, the images are recorded at a magnification of 0.62, resulting in a pixel resolution of 8.9 μm/pixel. The flow field is seeded with 13 μm diameters, silver-coated glass spheres, which is the same as used in the experiment of turbulent channel flow over a compliant surface (chapter 3). Flow field at three free stream speeds: 1.2 m/s, 3.2 m/s and 5.9 m/s are measured. "Standard" SPIV cross-correlation procedures are performed using LaVision® Davis 8.4 software and the mean velocity profiles are plotted in figure 4.19. In the near-wall region, the boundary layer of the compliant wall starts to deviate from that of a smooth wall case. However, limited by the spatial resolution, details about the near-wall flow is not clear. Thus, a higher resolution 2D PIV measurement is performed to characterize the boundary layer profile at the buffer region and the viscous sublayer.

Figure 4.20 is a sketch for the higher-resolution 2D PIV setup. The same lens and optics as the SPIV are used, except an additional extension tube is placed in front of the camera to increase the magnification. The images are recorded at a magnification of 1.67, resulting in a pixel resolution of 3.3 μm/pixel. The flow field is seeded globally using 2 μm diameters, silver-coated glass spheres - Potters Industries Conduct-O-Fil® SG02S40 particles. These particles have a density of 4 g/cm^3, but owing to their size, they are expected to have a negligible slip relative to the surrounding flow (Melling 1997, Adrian 1991, Grant 1996). The delays between exposures, 40, 15, and 8 ms for freestream speeds of 1.2, 3.2, and 5.9 m/s, respectively, have been selected to maintain a maximum particle displacement of about 12 pixels. For each case, 17000 pairs of particle images have been recorded to facilitate high-resolution measurements of the mean velocity using the "sum-of-correlation" (Westerweel et al, 2004) method. Using a correlation window of 3×3 pixels with a 50% overlap maintains an ensemble average of 500 particles per window. This analysis focuses on the inner part of the boundary layer, extending from the wall up to 116, 330, and 660 wall units ($\delta_\nu = \nu/u_\tau$, details follows), while maintaining a window resolution of $0.5\delta_\nu$, $1.0\ \delta_\nu$ and $2.0\ \delta_\nu$ at U_0=1.2, 3.2, and 5.9 m/s, respectively. An in-house GPU-based code has been used for this analysis. Prior to application, the analysis has been calibrated using synthetic PIV data and compared to the results obtained using the LaVision® Davis 8.4 code, showing essentially no differences in results. The associated uncertainty in mean velocity is well below 1%. Standard 2D cross-correlation analysis using the LaVision® Davis 8.4 software has been used to obtain the turbulence statistics. These calculations have been performed using multi-pass correlations with a final window size of 32×32 pixels, with a 50% overlap. Consequently, the Reynolds stress measurements are under-resolved, and results are restricted to the log layer.

Figure 4.21 compares the mean velocity profiles above the smooth wall (figures 4.21a, b, and c) to those above the compliant layer (figures 4.21d, e, and f) at three velocities or $E/\rho U_0^2$. Both the 2D PIV and the sum-of-correlation results are presented. They nearly overlap except for the lowest points where the standard results are too coarse. In all three cases, the rigid wall velocity profiles are consistent with those of a typical classical turbulent boundary layer with a viscous sublayer, buffer layer, log region that expands with increasing Reynolds number, and parts of the outer layer. The boundary layer parameters, including u_τ and δ_v evaluated from a fit to the log layer and measured directly from the velocity profile in the viscous sublayer ($y^+<5$), as well as boundary layer thickness and Re_τ, are presented in Table 4.1. For the complaint wall profiles, u_τ is calculated from a log layer fit.

To highlight the effect of the compliant wall, figures 4.21d, e, and f, compares the velocity profiles to the standard viscous sublayer and log layer using the same constants as those of the smooth wall. As Table 4.1 shows, except for the lowest velocity, where the values of u_τ are very close to those of the smooth wall, for the higher speeds, the complaint wall increases the friction velocity by about 20%. The velocity profiles begin to deviate from those of the typical boundary layer even at the lowest velocity (figure 4.21d), although the difference is quite small and the viscous sublayer is retained for the most part. Substantial deviations occur at U_0=3.2 m/s (figure 4.21e) and 5.9 m/s (figure 4.21f) when the amplitude of the deformation (figure 4.8) are $0.69\delta_v$ and $3.6\delta_v$. Both show lower momentum in the log layer, and a sharp decrease in velocity at $y^+=10$ at U_0=3.2 m/s, and $y^+=13$ at U_0=5.9 m/s. Closer to the wall, the velocity gradients are small, which does not indicate low wall stress since the boundary is not stationary. Figure 4.22 compares the three velocity profiles to the DNS results of Rosti and Brandt (2017) for much lower Reynolds numbers, and except for one case, involves lower values of $E/\rho U_0^2$. Yet, their profile for $E/\rho U_0^2=2.92$ and the present results for $E/\rho U_0^2=2.4$ (highest velocity) appear to have similar trends in the region of a sharp decrease in velocity in the inner part of the boundary layer. However, their zone of high-velocity gradients extends to a higher elevation. They also show that with decreasing $E/\rho U_0^2$, the region of sharp gradients shifts to a higher elevation, reducing the momentum in the log layer as well.

Profiles of Reynold's normal and shear stresses are compared to those of the smooth wall in figure 4.23. Owing to the limited spatial resolution of the present 2D PIV measurements, the results are presented only for the lowest and intermediate freestream velocities, and are limited to the elevation where the resolution-dependent uncertainty is below $0.5u_\tau$ (Wang et al. 2019). For the highest velocity, the interrogation window size is $20\delta_\nu$, making the results questionable for the relevant inner part of the boundary layer. This problem will be addressed in future studies by performing measurements at a higher resolution using e.g. holographic microscopy (Sheng et al. 2006, Gao and Katz 2018). Results for the smooth wall are consistent with expectations. Even for the lowest velocity, above the compliant wall (figure 4.23b), there is a sharp increase in $<v'v'>$ and $<u'u'>$ near the wall, which does not involve an increase in $-<u'v'>$, i.e. the correlation among the components involved. This trend becomes stronger with increasing velocity (figure 4.23d), where the value of $<v'v'>$ over the complaint wall (at the lowest data point) is three times higher than that of the smooth wall, and $<u'u'>$ is 15% higher. In this case, the shear stress also increases near the wall, but not at the same rate as the individual components. Rosti and Brandt (2017) also report an increase in turbulence levels near the wall, especially $<v'v'>$, as well as an increase in the shear stress at a slower pace compared to the individual components. These trends raise questions on the structure of the turbulence and associated length scales.

Glimpses at the extent of changes to the log layer turbulence (y^+=600) are provided in figures 4.24 and 4.25 that compare u'-u' and v'-v' two-point correlations above the compliant coating to those of the smooth wall. As is evident, for both components, with increasing velocity or wall deformation amplitude relative to the wall unit, the correlation length scales diminish rapidly, suggesting that interactions with the wall “scramble” the turbulence, making it much less coherent. However, the effects of wall deformation on the turbulence structure are evident even at the lowest velocity, i.e. when the deformation amplitude is much smaller than a wall unit ($0.024\delta_v$, see figure 4.8). At the intermediate freestream velocity (figures 4.24d and 4.25d), when the deformation amplitude is comparable to a wall unit ($0.69\delta_v$), the wall motions are sufficient to cause a typical 20% and 15% reduction in *u'-u'* and *v'-v'* correlations at the same distance, respectively. When the deformation exceeds a wall unit ($3.6\delta_v$), *u'-u'* and *v'-v'* correlations decrease by 55% and 40% respectively. Clearly, even extremely small deformations are sufficient to cause two-way coupling with the mean flow and turbulence in the boundary layer. A reduction in the characteristic correlation length scales with decreasing $E/\rho U_0^2$ has been observed also in the Rosti and Brandt (2017) simulations. Yet, the find an increase in the spanwise length scales that have not been measured in here, which they attribute to the preferred spanwise alignment of the deformation. A discussed before, in this study, the tendency towards a preferred spanwise alignment has only been observed with increasing velocity.

4.4 Conclusions and Discussions

Expanding on a previous effort, the present measurements focus on a compliant surface that is soft enough to deform at scales that modify the boundary layer structure achieving two-way coupling. The surface properties are also selected, using a theoretical analysis introduced by Chase (1991), to fit within the wavenumber and frequency range of the data acquisition systems, enabling us to cover most of the important phenomena. The results show that the complaint wall deformation begins to impact the velocity profile when the amplitude of deformation is only a few percent of the wall unit. When the amplitude is comparable to a wall unit or larger, the wall deformations cause a sharp decrease in momentum in the inner part of the boundary layer (less than 10 wall units). The turbulence level increases substantially, especially the wall-normal component, but the associated length scales decrease, i.e. the turbulence becomes more scrambled. The increase in turbulence level and decrease in *u'-u'* and *v'-v'* correlations with decreasing $E/\rho U_0^2$ are consistent with trends described in Rosti and Brandt (2017). Furthermore, for the only case where their and our $E/\rho U_0^2$ have the same magnitude, their velocity profile in the inner part of the boundary layer also shows a very similar sharp decrease at 4-10δ_v. However, their range of high-velocity gradients extends to a higher elevation, possibly because of the difference in Reynolds number. The corresponding present value of $\dot{d}_{t,RMS}^{+}$ is 0.021, whereas their's is =0.075, i.e. they are within the same order of magnitude.

The present values of $\dot{d}_{t,RMS}^{+}/d_{t,RMS}^{+}$ decrease from 1 to 0.04 with increasing freestream velocity (table 1). Hence, following the discussions in Kim and Choi (2014), Xia et al. (2017) and Benschop et al. (2019), the wall velocity should affect the flow-wall interactions at low speeds, but not at high speeds, where the wall is expected to be impacted most by the displacement wave. Yet, the magnitude of $\dot{d}_{t,RMS}^{+}$ is small over the entire present range of test conditions, varying between 0.004 to 0.021, suggesting that the wall velocity is not playing a major role at any speed. The corresponding magnitudes of $d_{t,RMS}^{+}$, which vary from 0.004 to 0.54, support the postulate that the displacement is more important than the wall velocity at high speed. It is not clear, however, what affects the changes to the flow structure at low and intermediate speed, where both $d_{t,RMS}^{+}$ and $\dot{d}_{t,RMS}^{+}$ are small. Another possibility involves pressure fluctuations induced by the oscillating boundary. The magnitudes of wall acceleration $\ddot{d}_{t,RMS}$, also presented in table 4.1, are also significantly smaller than the corresponding values of u_τ^3/ν or U_0^2/δ. Yet, in boundary layers, including those over a stiff compliant wall ($E/\rho U_0^2$ ~220) reported in Zhang et al. (2017), the pressure fluctuations have the highest correlations with the wall-normal velocity fluctuations. Considering that the compliant wall causes a sharp increase in <*v'v'*> even at the lowest velocity (figure 4.23d), it is not unreasonable to postulate that the near-wall pressure fluctuations also increase. Such observations should provide the rationale for performing detailed pressure fluctuation measurements near the compliant surface, which we hope to perform in future studies.

It should be noted that trends of the mean velocity profile are inconsistent with those of a turbulent boundary layer over a rough wall (e.g. Hong et al. 2011, 2012, Jimenez 2003, Perry et al. 1987, Burattini et al. 2008, Djenidi et al. 2008, Lee & Sung 2007), where the semi-log plotted velocity profile plateaus in the inner part of the boundary layer. Furthermore, above rough boundaries, the turbulence level peaks about four roughness heights away from the wall. It then decreases as the wall is approached, but rises again very close, i.e. less than one roughness height, to the roughness elements (Ikeda & Durbin 2007, Talapatra & Katz 2012). In contrast, above the compliant wall, the velocity drops sharply and the turbulence is high well above the surface deformations. Hence, referring to the compliant wall as a rough surface does not account for the important dynamic interactions.

Wavenumenr-frequency and two-dimensional spectra show that the wall deformations consist primarily of two modes. The first is an advected mode that travels with the flow at 66% of the free stream velocity for all frequencies and wavenumbers, i.e. we do not observe a scale-dependent advection. This velocity magnitude corresponds to the transition between the buffer layer to the log layer at y^+=60-80. In the prior experiments reported in Zhang et al. (2017), the advection speed for a channel flow with a stiffer wall is 72% of the centerline velocity. While this mode has a broad range of wavelengths, the wavelength of the spectral peak is $3l_0$. It also has a lattice-like structure, with preferential alignment on the spanwise direction. Frequency spectra for this mode nearly collapse if the frequency is scaled using the freestream velocity and the compliant wall thickness. The second mode propagates predominantly in the spanwise direction and is concentrated in the low wavenumber and high-frequency range. The k_z-ω and k_x-k_z spectra show that this mode also has a characteristic wavelength of $3l_0$, and travels at the shear speed of the compliant material irrespective of the freestream velocity. When the tunnel speed is of the same order as the shear speed, the two modes coincide in the k_z-ω spectra. At low speeds, the spanwise-propagating mode is dominant, but with increasing velocity, the advected modes take over. However, the spanwise mode persists at all velocities.

Both the present results and the simulations by Rosti and Brandt (2017) for much lower Reynolds numbers and softer materials show that the surface patterns are preferentially aligned in the streamwise direction at low velocity, and in the spanwise direction at high velocity. They attribute the low-velocity behavior to the effects of low-speed streaks, which commonly occur in turbulent boundary layers. However, as noted above, the present measurements and analysis suggest that the streamwise-aligned pattern is associated with spanwise propagating shear waves, which maintain the same wavelength with increasing Reynolds number, in contrast to trends of low-speed streaks, which have a typical wavelength of ~$100\delta_v$ (Smith and Metzler 1983, Brereton and Hwang 1994). Furthermore, for the present conditions, the width of the low-speed streaks should be at least an order of magnitude smaller than the measured wavelength. In the Rosti and Brandt (2017) low Reynolds number simulations, $3l_0 \sim 270\delta_v$, i.e. the expected width of low-speed streaks are of the same order of magnitude as $3l_0$.

Benschop et al. (2019) fit their RMS values of deformation for several speeds and material properties to the following empirical relation, $d_{t,\mathrm{RMS}}=0.031 l_0 p'_{\mathrm{RMS}}/G$. Here, $G=E/[2(1+\nu_\mathrm{p})]$ is the shear modulus (ν_p is the Poisson Ratio) and p'_{RMS} is the RMS pressure fluctuation estimated by them using empirical data provided by Goody (2004), namely $p^+_{rms}= 0.0309 +$

$0.745(ln(R_T))^2$ where $R_T=u_\tau/U_0Re_\tau$. The present values of p'_{rms}/G, namely 2×10^{-3} - 5×10^{-3} are an order of magnitude smaller than those of Benschop et al. (2019) since the compliant material is stiffer. Our measured RMS level (figure 8) for the lowest velocity agrees with this empirical relation, but results deviate with increasing velocity, reaching values that are more than three-time higher at U_0=5.9 m/s. The Rosti and Brandt (2017) RMS values normalized by inner variables are at the same level as our measurement for the matched $E/\rho U_0^2$.

Results of two previously-published one-dimensional linear models of wall deformation by Chase (1991) and by Benschop et al. (2019), which solve the same Helmholtz equations, but with different boundary conditions, are used for elucidating the present trends. Both models predict a peak response at a wavelength of $3l_0$ and at a frequency corresponding to the shear speed of the material. Differences predominantly occur at low wavenumbers and high frequency. In comparing the frequency spectra to the model predictions, we account for the frequency-dependence of both the material properties and the turbulent boundary layer pressure spectrum (Goody 2004, and Tsuji et al. 2007). For the advected mode, the models reproduce the spectral peak. Furthermore, the experimental amplitude most closely agrees with the Benschop model prediction using the Goody (2004) pressure spectrum, but the corresponding Chase (1991) results are not substantially different. If a uniform pressure spectrum is used instead, the predicted amplitude is substantially higher. In contrast, this approach does not reproduce the low wavenumber fraction of the k_x-ω spectrum, especially the high-frequency part. Yet, for excitation at a constant amplitude, both models predict a peak response at a wavelength of $3l_0$ and frequency corresponding to the shear speed by the Chase model or slightly above it by the Benschop model. Hence, especially at low speed, when the excitation amplitude is low the surface should be expected to resonate at its peak response conditions, consistent with the experimental results. The remaining question involves the preferred alignment of such waves. Considering the rectangular shape of the compliant surface, a wave reflected from its boundaries travel a much shorter distance in the spanwise direction, suggesting that the spanwise-propagating wave would be stronger. The validity of these claims will be investigated in future studies.

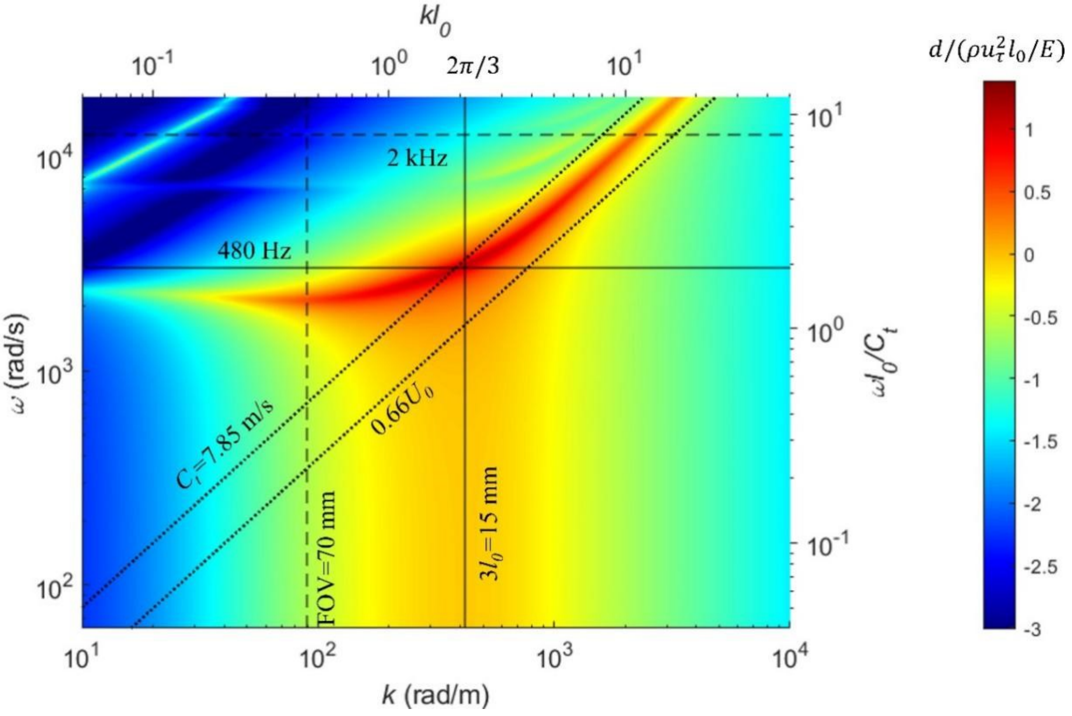

FIGURE 4.1. The amplitude of deformation (normalized by $\rho u_\tau^2 l_0/E$) in response to constant pressure perturbation with an amplitude of ρu_τ^2, as predicted by the Chase (1991) model.

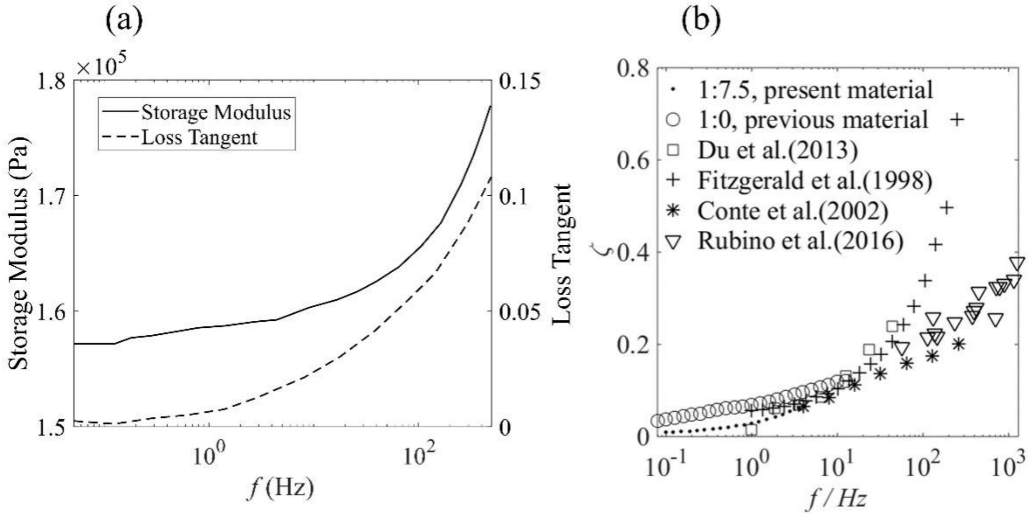

FIGURE 4.2. (a) The frequency-dependent storage modulus and loss tangent of the compliant surface measured at T=25℃. (b) The loss tangent of the present material comparing with previous material and others.

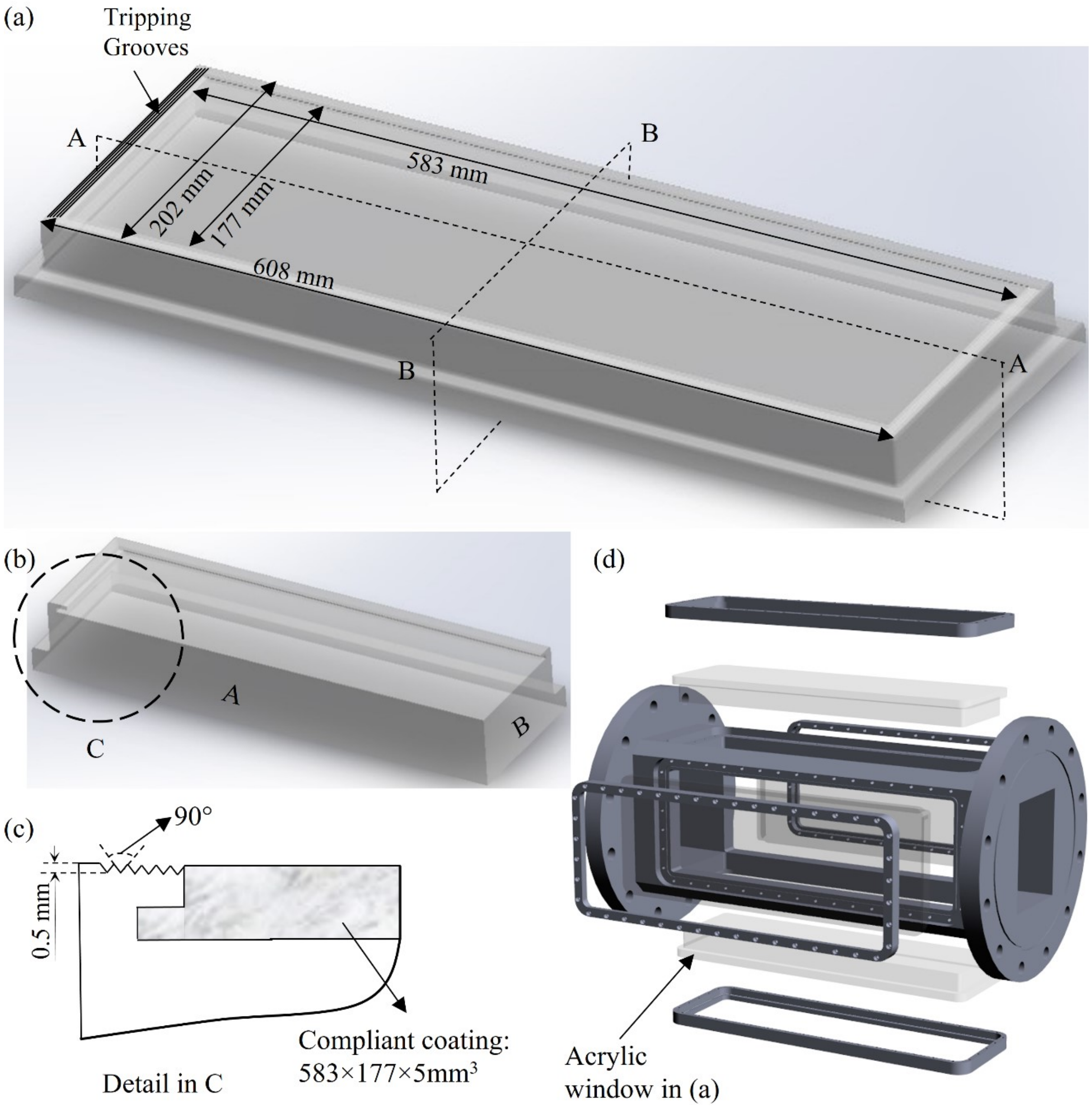

FIGURE 4.3. The window containing the compliant coating: (a) a full view of the window, showing the location of the tripping grooves, (b) a section view of the window with planes A and B indicated in (a), and (c) the upstream end (view C) showing the tripping grooves and compliant coating installed. (d) A schematic showing how the window is assembled in the test section.

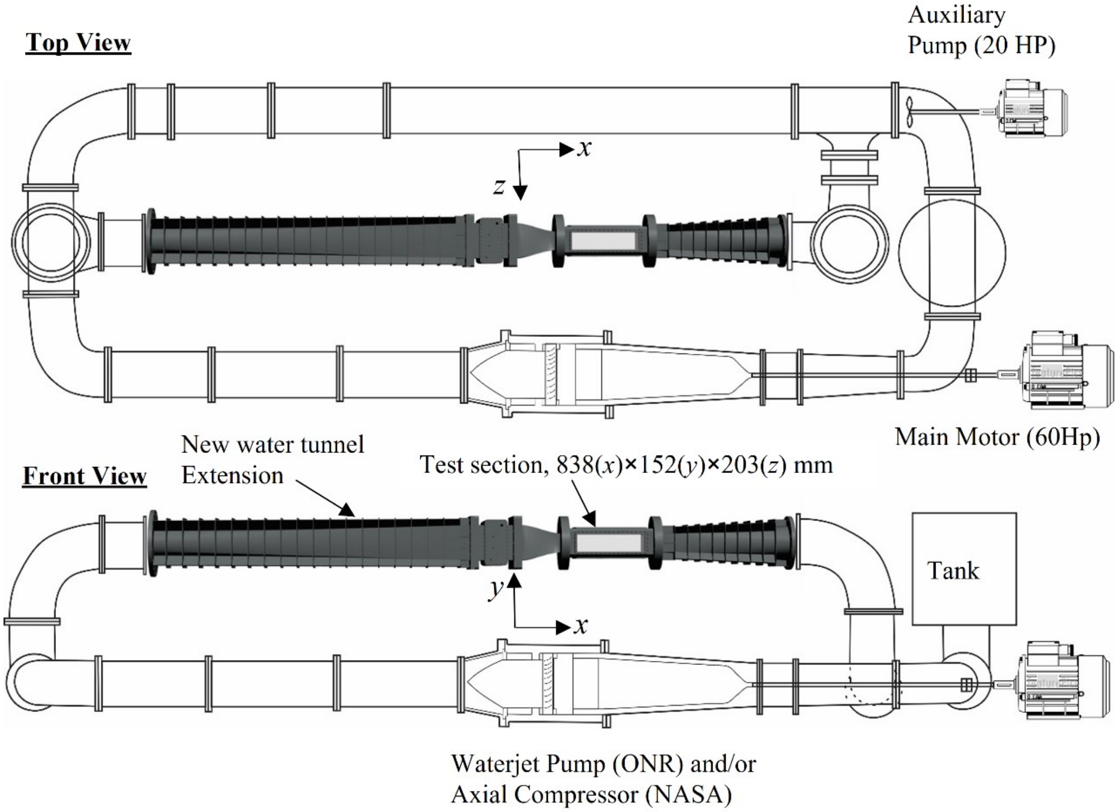

FIGURE 4.4. Schematics of the new refractive index-matched water tunnel.

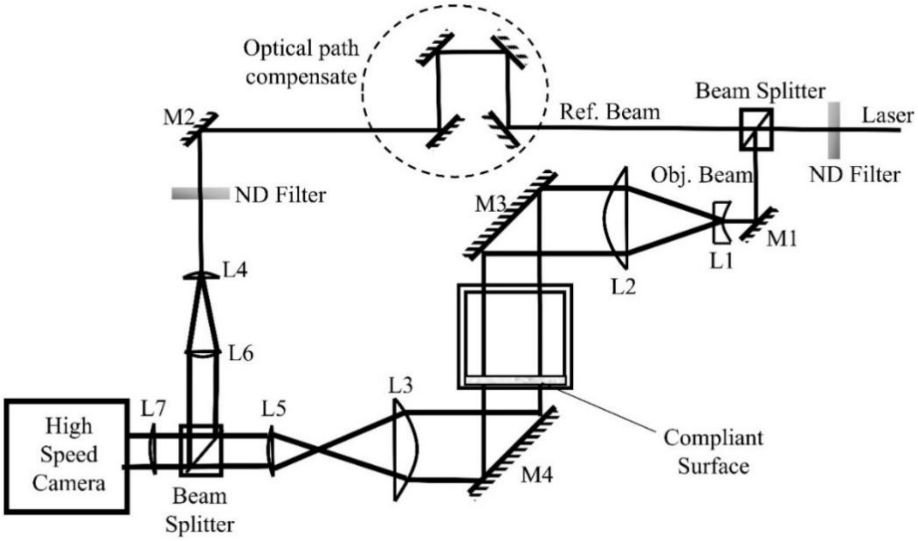

FIGURE 4.5. Setup of the large field of view Mach-Zehnder Interferometer used for measuring the 2D surface deformation.

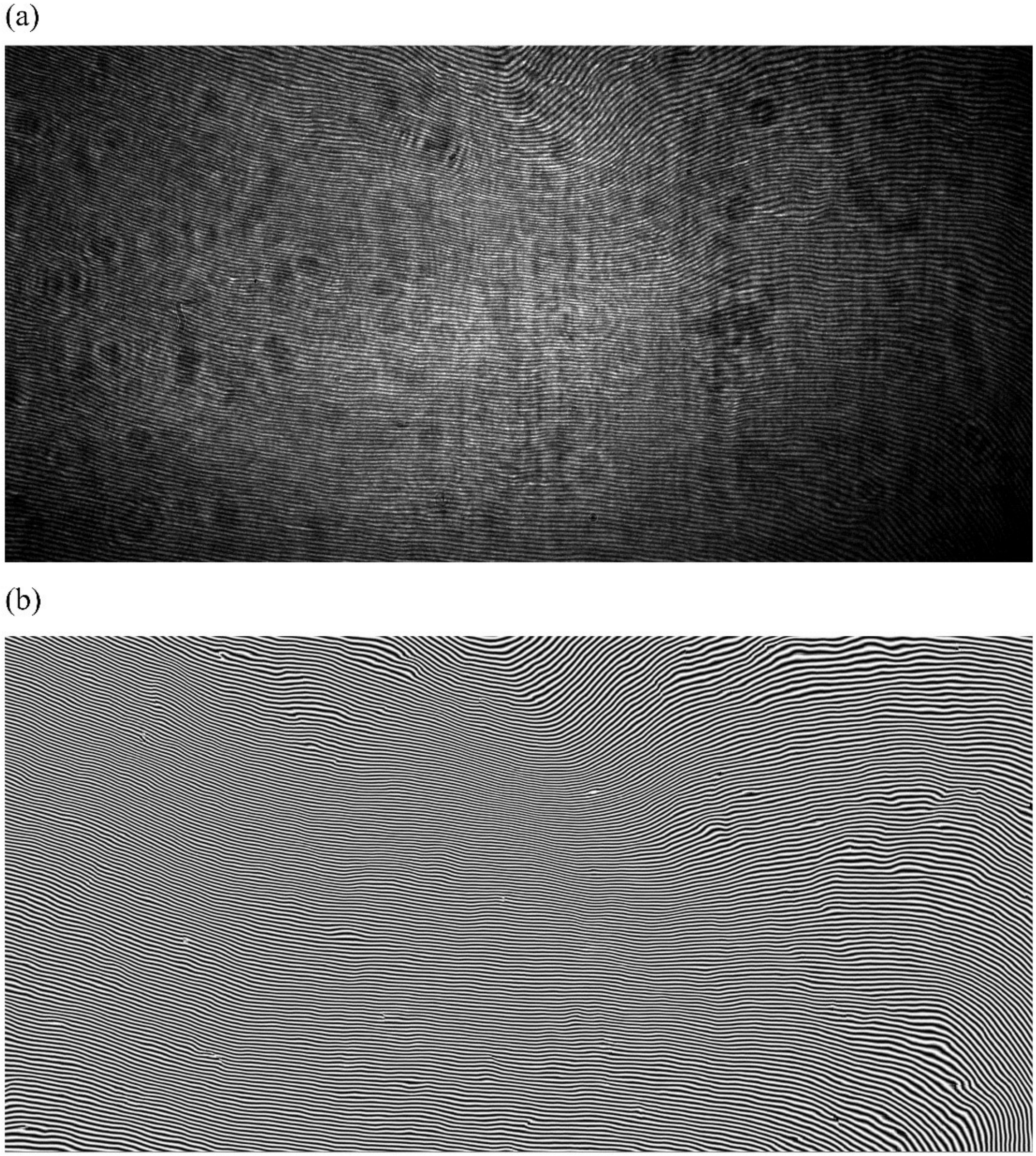

FIGURE 4.6. Samples of MZI fringe patterns (U_0=3.2 m/s): (a) raw data, and (b) correlation-based enhanced image.

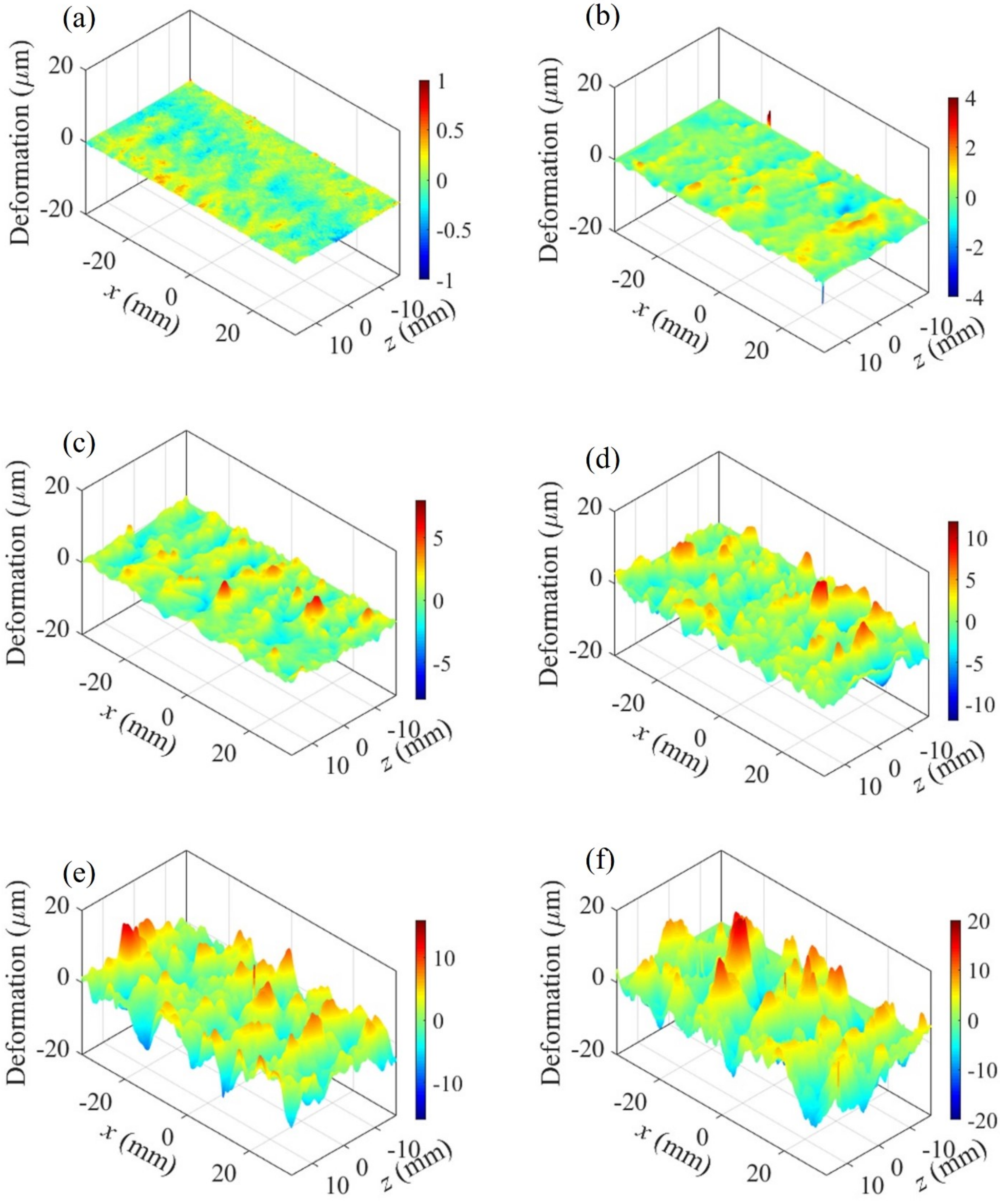

FIGURE 4.7. Samples of compliant surface shape for U_0 and $E/\rho U_0^2$ of: (a) 1.2 m/s, 59.0; (b) 1.9 m/s, 23.5, (c) 3.2 m/s, 8.3, (d) 4.5m/s, 4.2, (e) 5.3 m/s, 3.0 and (f) 5.9 m/s, 2.4. While the axis scales are constant, the color scales vary.

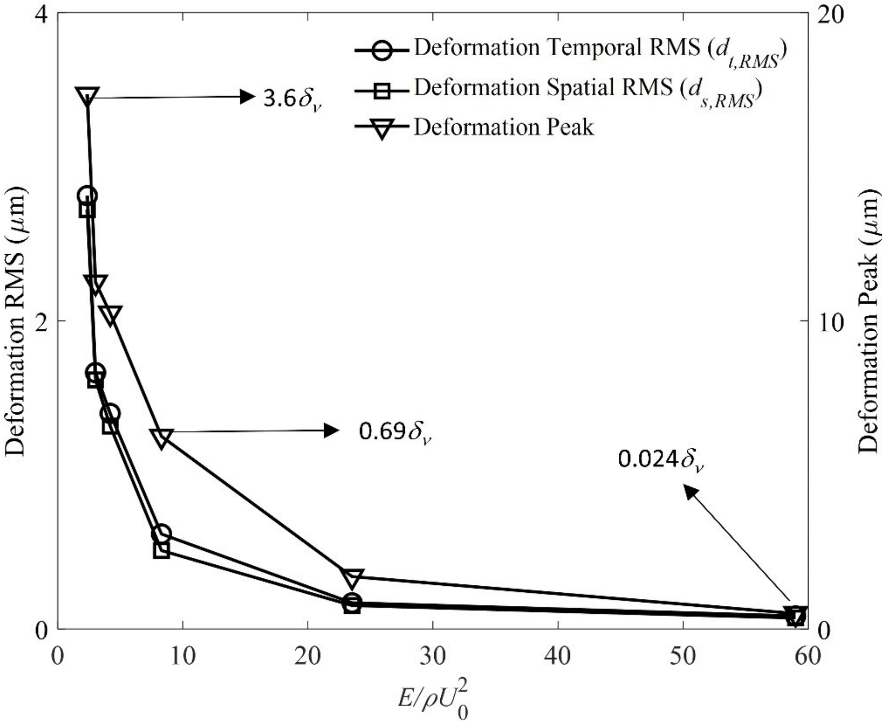

FIGURE 4.8. Variations of deformation peak as well as spatial and temporal RMS values with $E/\rho U_0^2$. Indicated values express the amplitude in terms of wall units.

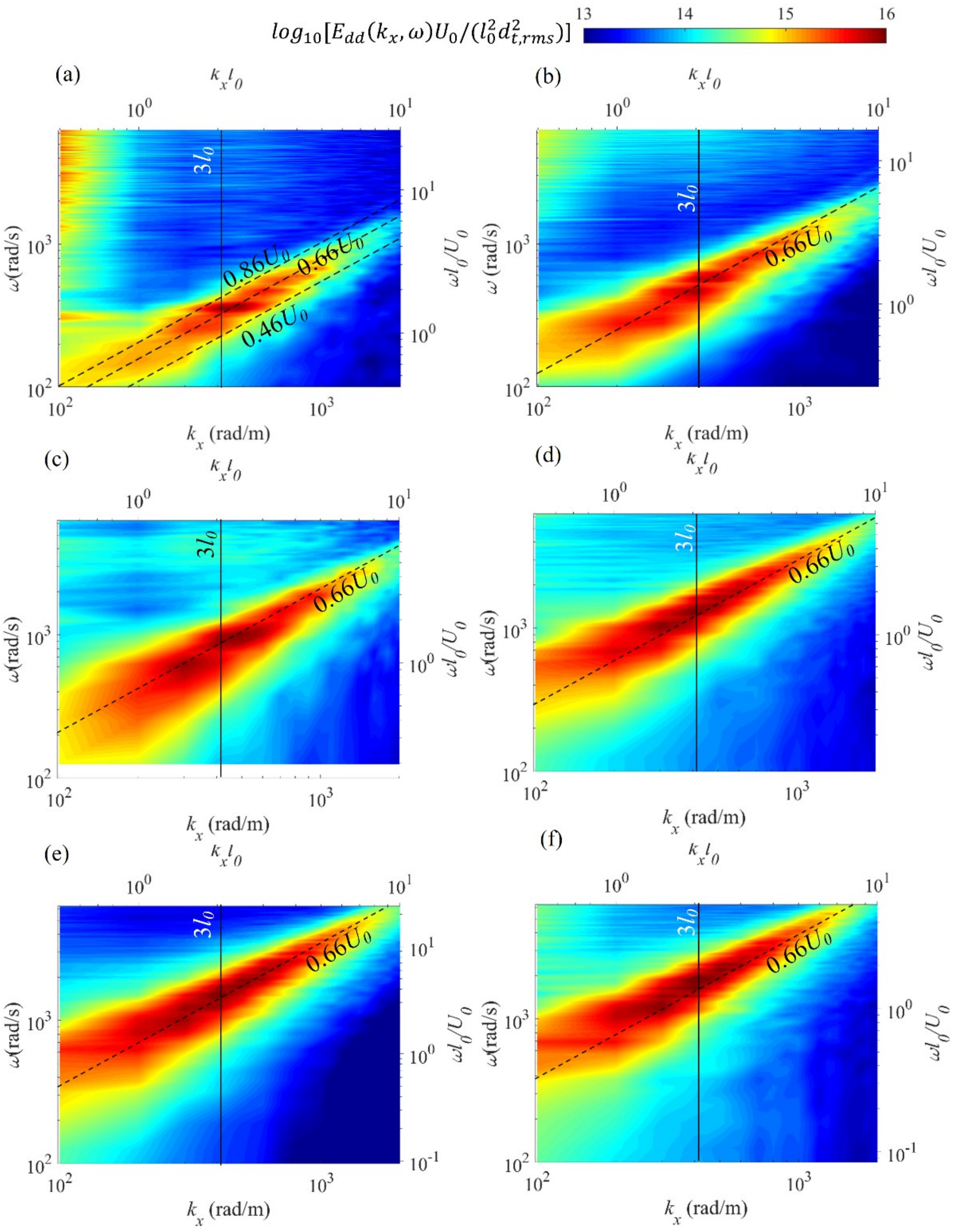

FIGURE 4.9. Streamwise wavenumber-frequency spectra of deformation for U_0 and $E/\rho U_0^2$ of: (a) 1.2 m/s, 59.0; (b) 1.9 m/s, 23.5, (c) 3.2 m/s, 8.3, (d) 4.5m/s, 4.2, (e) 5.3 m/s, 3.0 and (f) 5.9 m/s, 2.4. Dashed lines indicate an advection velocity of $0.66U_0$, and solid lines indicate the wavenumber correpnding to $3l_0$. Energy levels are scaled using $log_{10}[E_{dd}(k_x,\omega)U_0/(l_0^2 d_{t,rms}^2)]$, and the axes are presented both in dimensional and dimensionless scales.

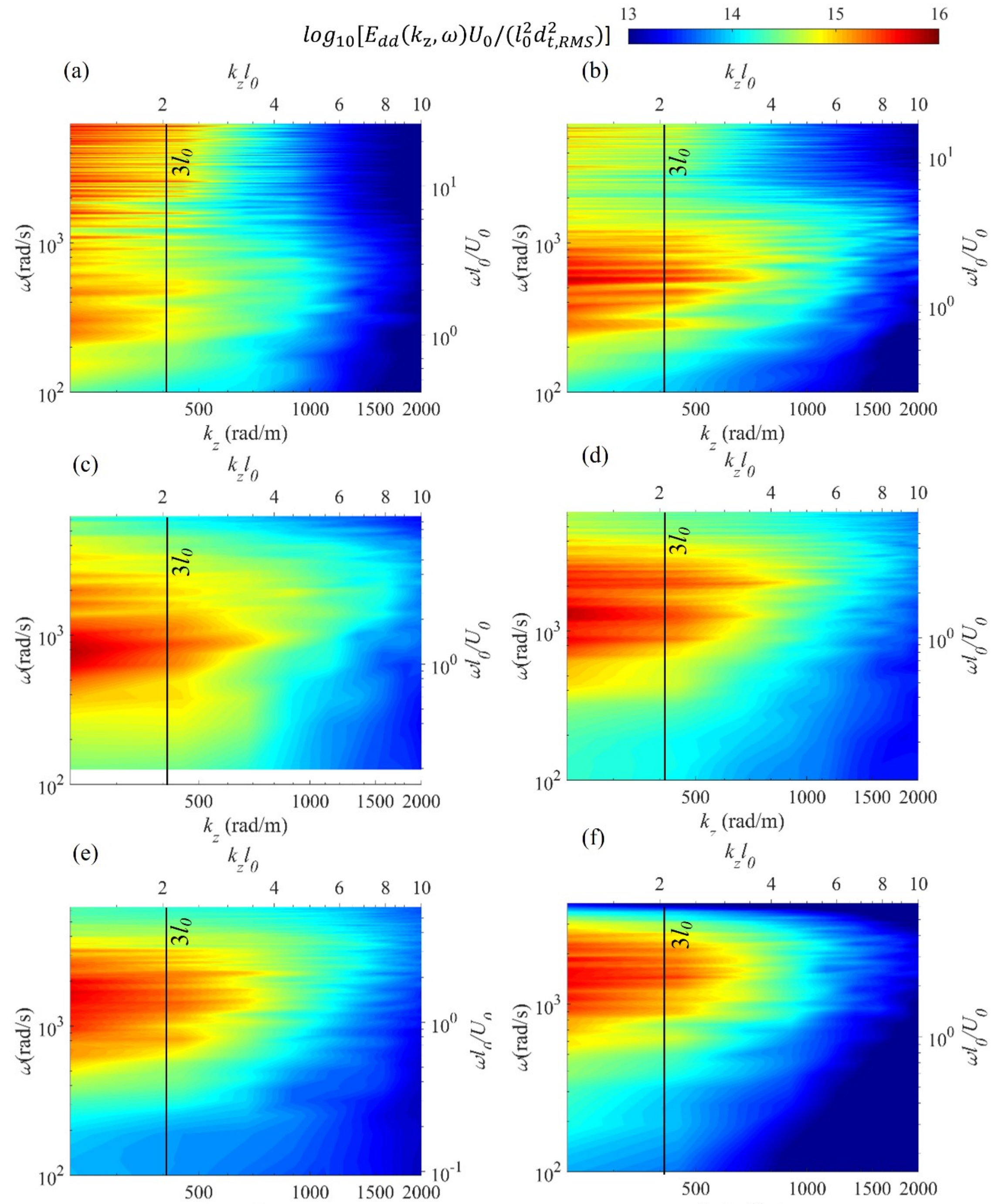

FIGURE 4.10. Spanwise wavenumber-frequency spectra of deformation for U_0 and $E/\rho U_0^2$ of: (a) 1.2 m/s, 59.0; (b) 1.9 m/s, 23.5, (c) 3.2 m/s, 8.3, (d) 4.5m/s,4.2, (e) 5.3 m/s, 3.0 and (f) 5.9 m/s, 2.4.

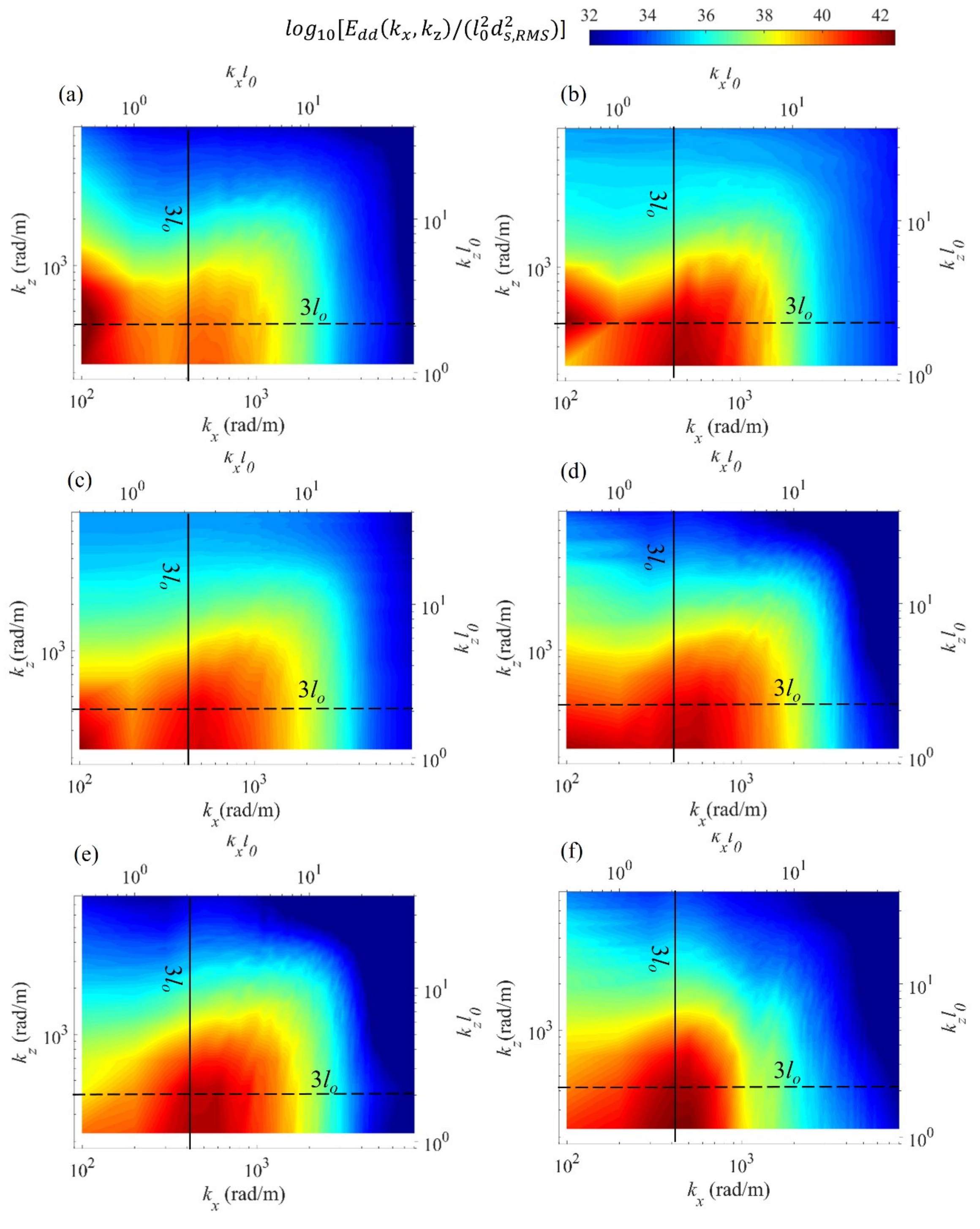

FIGURE 4.11. Two dimensional spectra of deformation for U_0 and $E/\rho U_0^2$ of: (a) 1.2 m/s, 59.0; (b) 1.9 m/s, 23.5, (c) 3.2 m/s, 8.3, (d) 4.5m/s,4.2, (e) 5.3 m/s, 3.0 and (f) 5.9 m/s, 2.4.

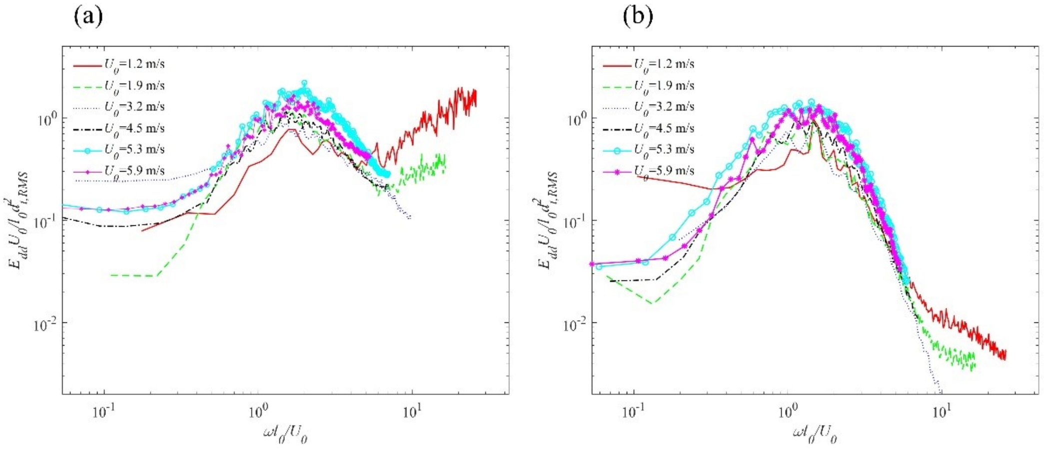

FIGURE 4.12. Temporal power spectral density of deformation for: (a) all wavenumbers and frequencies, and (b) the advected bands ($0.46U_0 < \omega/k < 0.86U_0$).

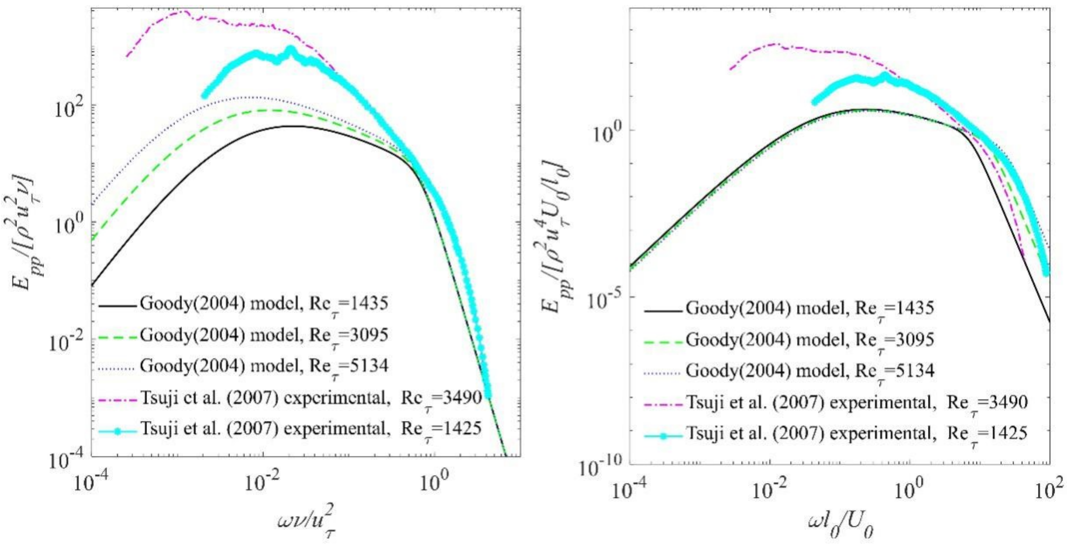

FIGURE 4.13. The pressure spectra from the Goody (2004) model and experimental measurement of Tsuji et al. (2007) at different Reynolds numbers: (a) normalized by inner variables, and (b) normalized by the outer variables.

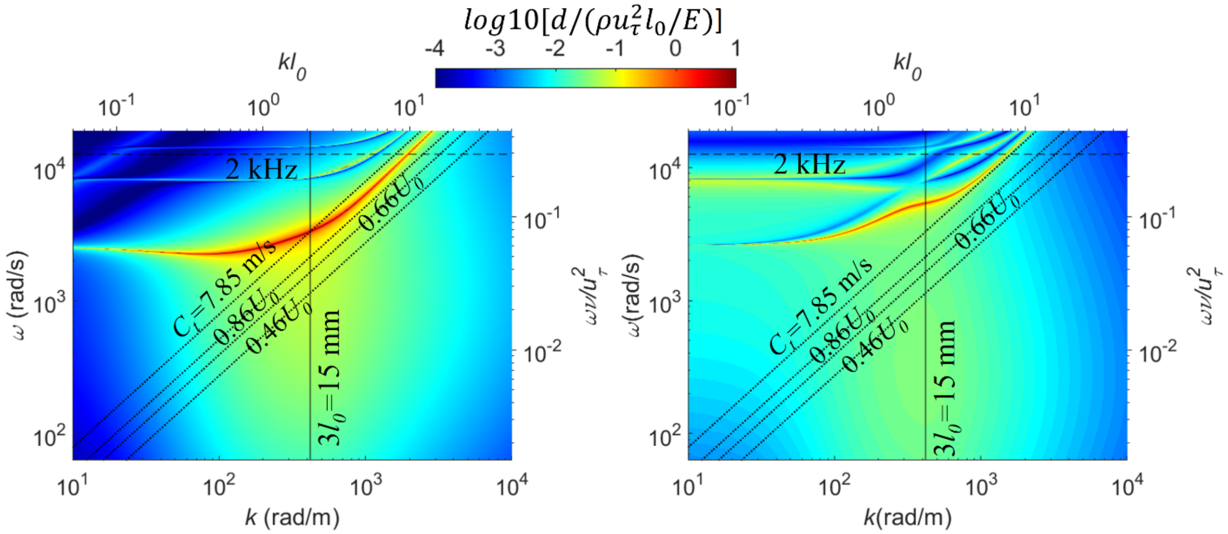

FIGURE 4.14. The amplitude of deformation (normalized by $\rho u_\tau^2 l_0/E$) in response to pressure perturbations modulated by the pressure spectra of Goody (2004), as predicted by: (a) the Chase (1991) model, and (b) the Benschop et al. (2019) models. Inclined dotted lines refer to advection bands at U_0=5.9 m/s.

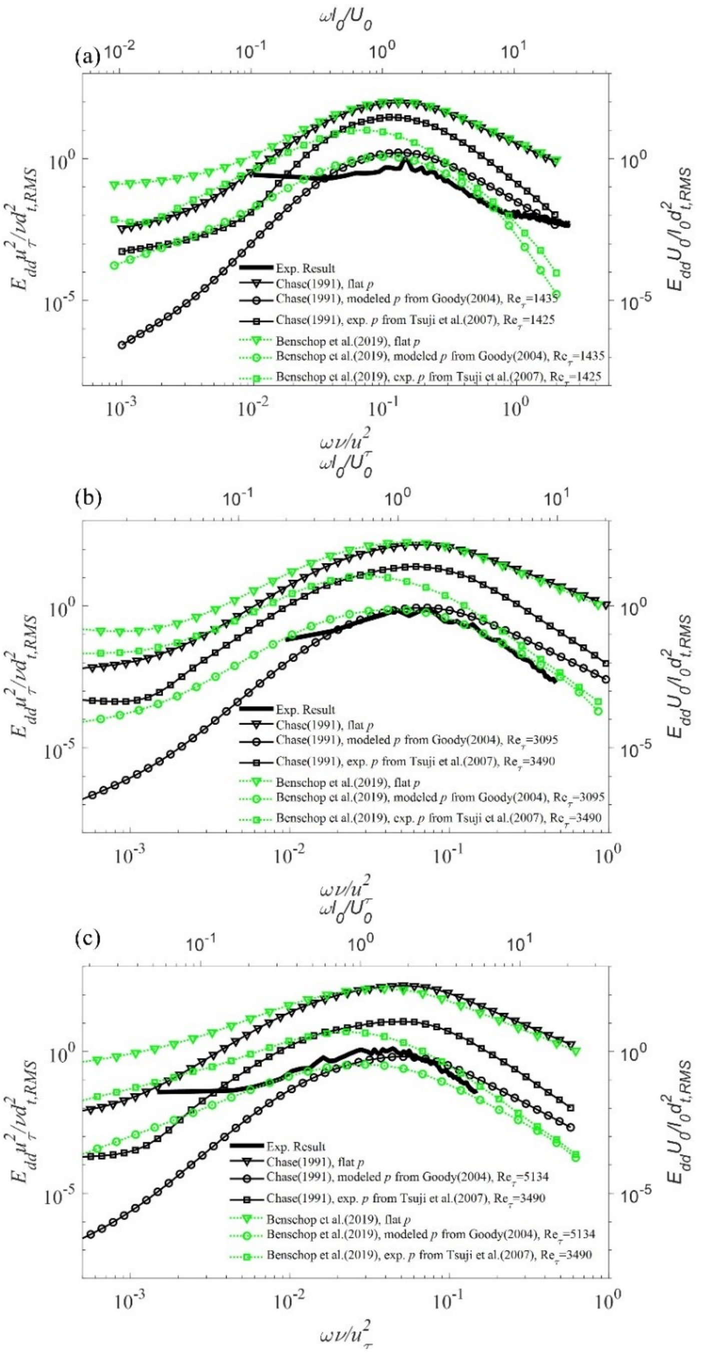

FIGURE 4.15. Comparison of the advected ($0.46U_0<\omega/k<0.86U_0$) measured power spectra with the predictions by the Chase and Benschop models. The analysis is performed using the measured frequency-dependent material properties, and three different pressure excitations spectra, namely flat, Goody (2004), and Tsuji et al. (2007). The corresponding U_0 and $E/\rho U_0^2$ are: (a) 1.2 m/s, 59.0, (b) 3.2 m/s, 8.3 and (c) 5.9 m/s, 2.4.

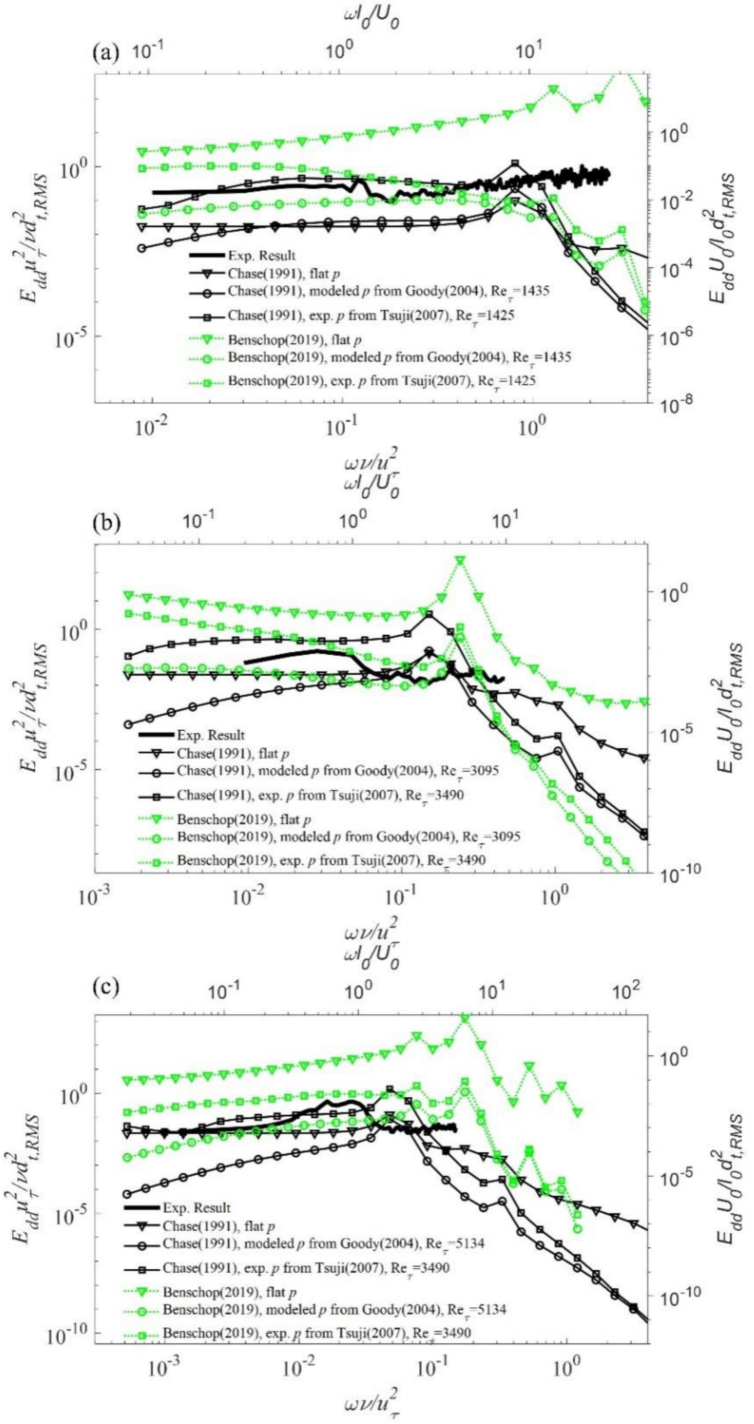

FIGURE 4.16. Comparison of the measured low-wavenumber power spectra (k_x<200 rad/m) with predictions by the Chase and Benschop models. The corresponding U_0 and $E/\rho U_0^2$ are: (a) 1.2 m/s, 59.0, (b) 3.2 m/s, 8.3 and (c) 5.9 m/s, 2.4. Excitation amplitude and material properties are the same as those in figure 4.15.

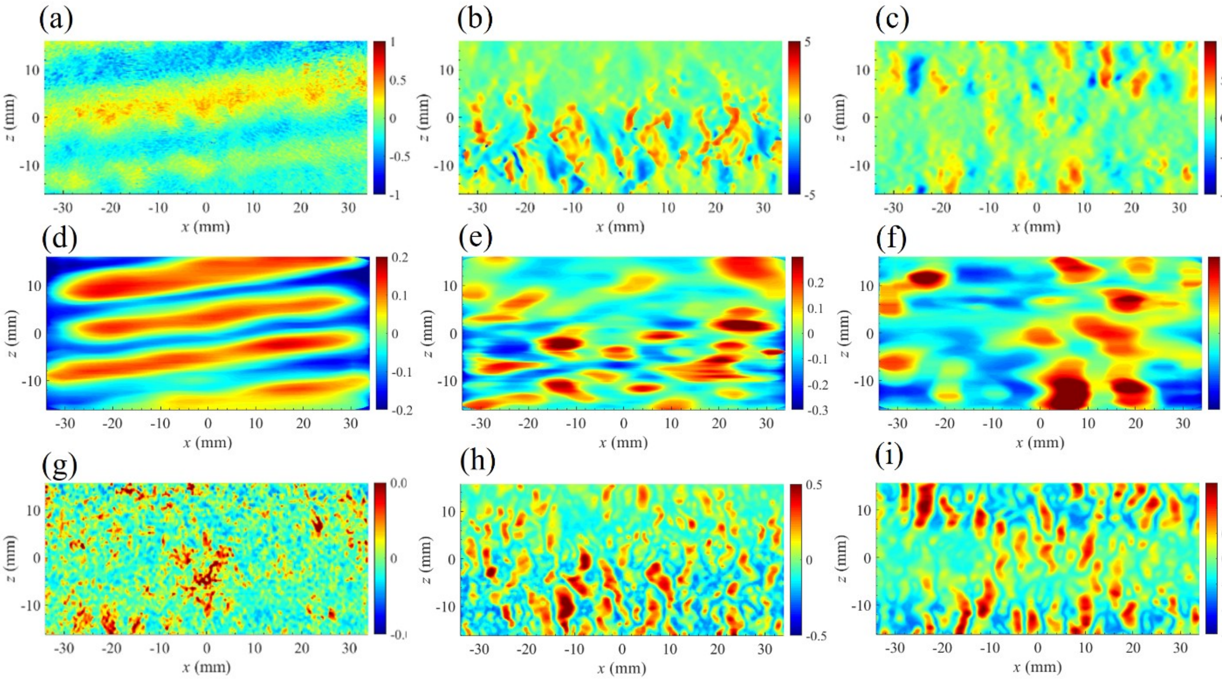

FIGURE 4.17. Deformation samples showing: (top row: a, b, c) the unfiltered signal, (middle row: d, e, f) low-pass fitered (k_x<200) signal, and (bottom row: g, h, i): advected modes filtered at $0.46<\omega/k<0.86$. Flow conditions are: (left column: a, d, g) U_0=1.2 m/s, and $E/\rho U_0^2$=59.0, (middle column:, b, e. h) U_0=3.2 m/s, and $E/\rho U_0^2$=8.3, and (right column, c, f, i) U_0=5.3 m/s, and $E/\rho U_0^2$=3.0. Note the differences in sclaes.

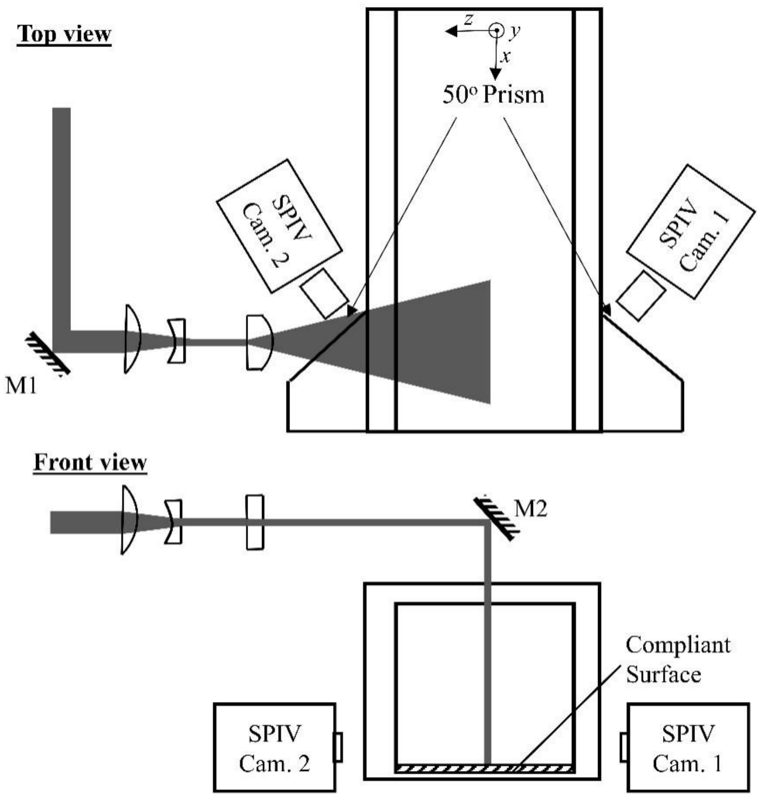

FIGURE 4.18. Stereo-PIV setup for measuring upper part of the turbulent boundary layer over a compliant surface

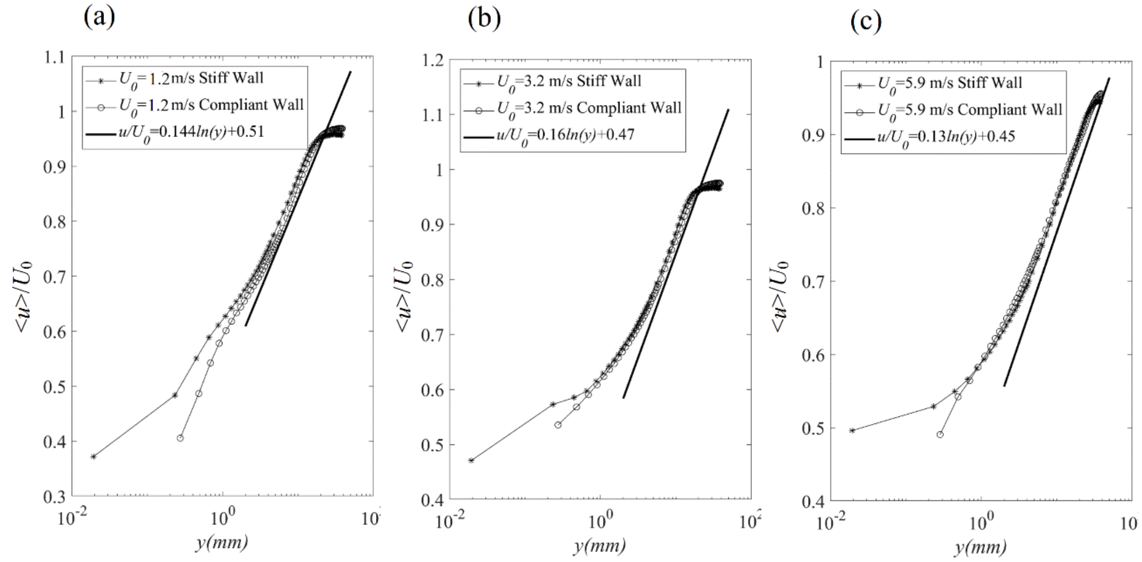

FIGURE 4.19. Mean velocity profiles measured by Stereo-PIV at U_0= (a) 1.2 m/s, (b) 3.2 m/s, (c) 5.9 m/s

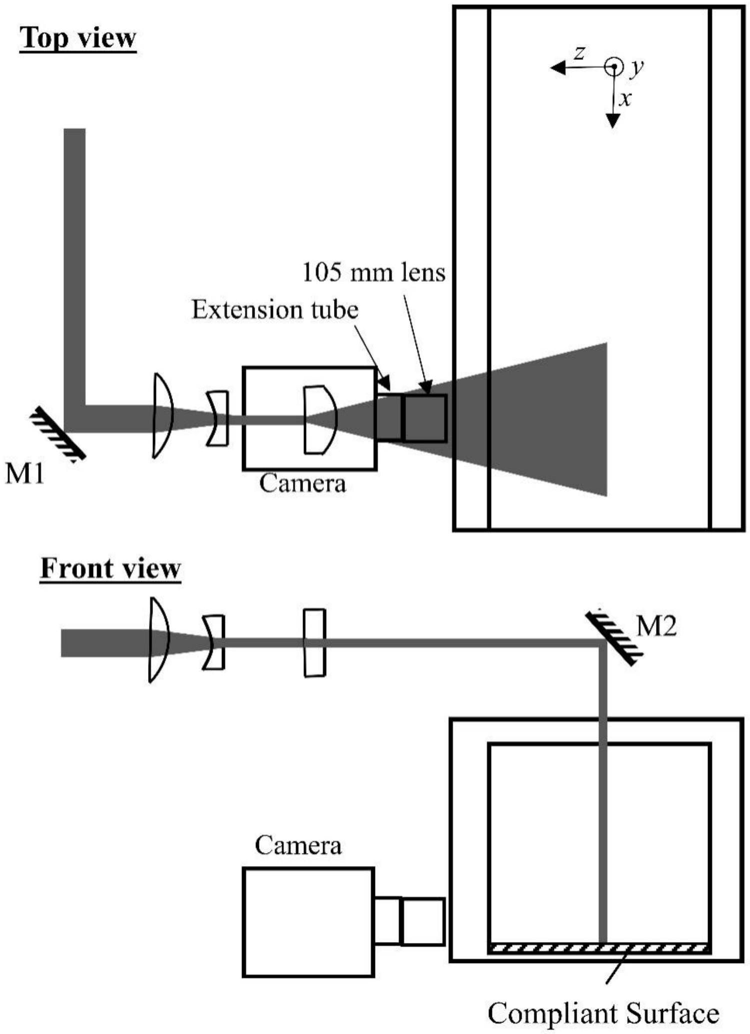

FIGURE 4.20. 2D-PIV setup for measuring the near-wall velocity in the turbulent boundary layer over a compliant surface.

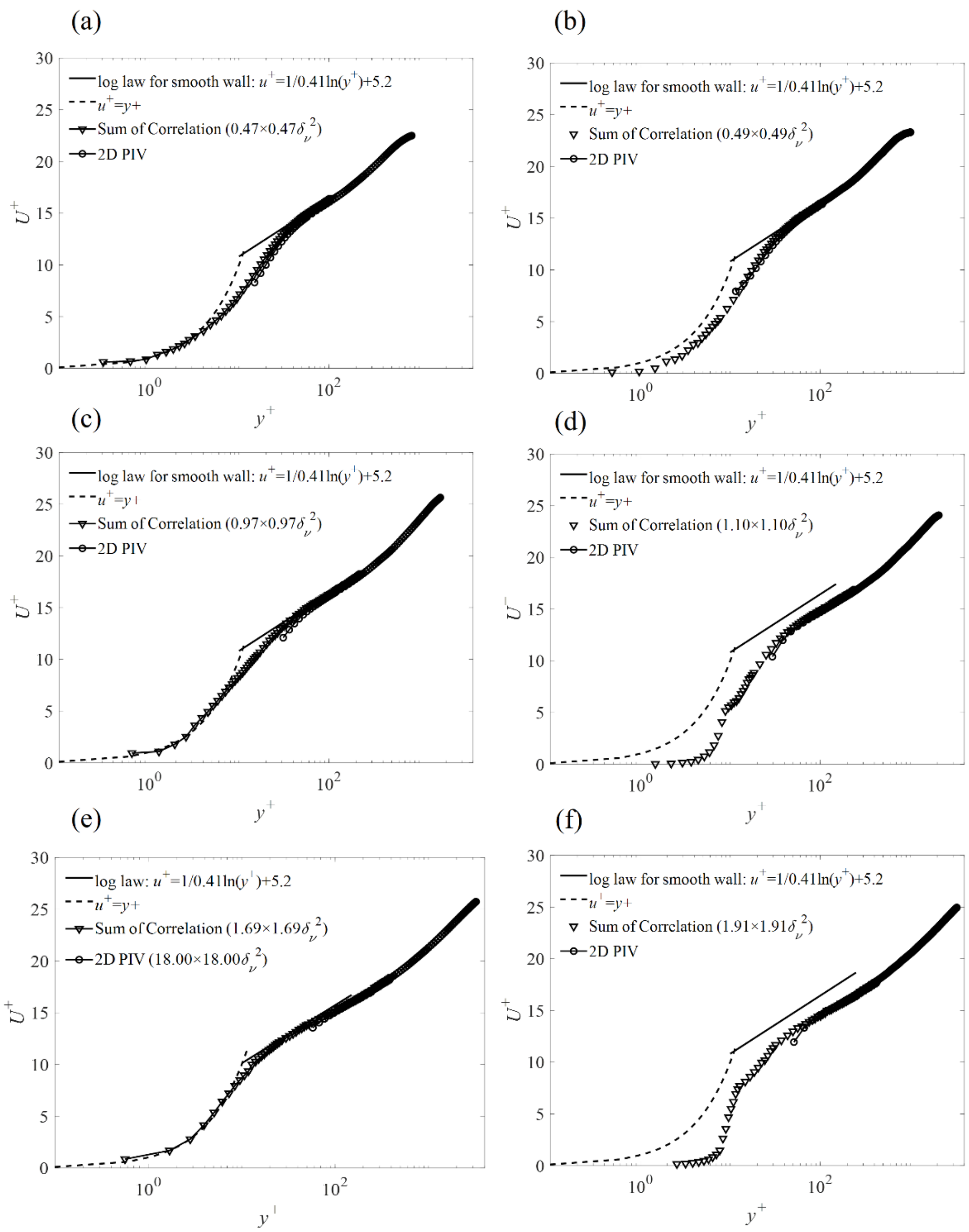

FIGURE 4.21. Normalized mean velocity profiles calculated using sum-of-correlation PIV and standard 2D PIV. Left column (a, c, e) smooth wall data; and right column (b, d, f) compliant wall data. (a, b) U_0=1.2 m/s, (c, d) U_0=3.2 m/s, and (e, f) U_0=5.9 m/s.

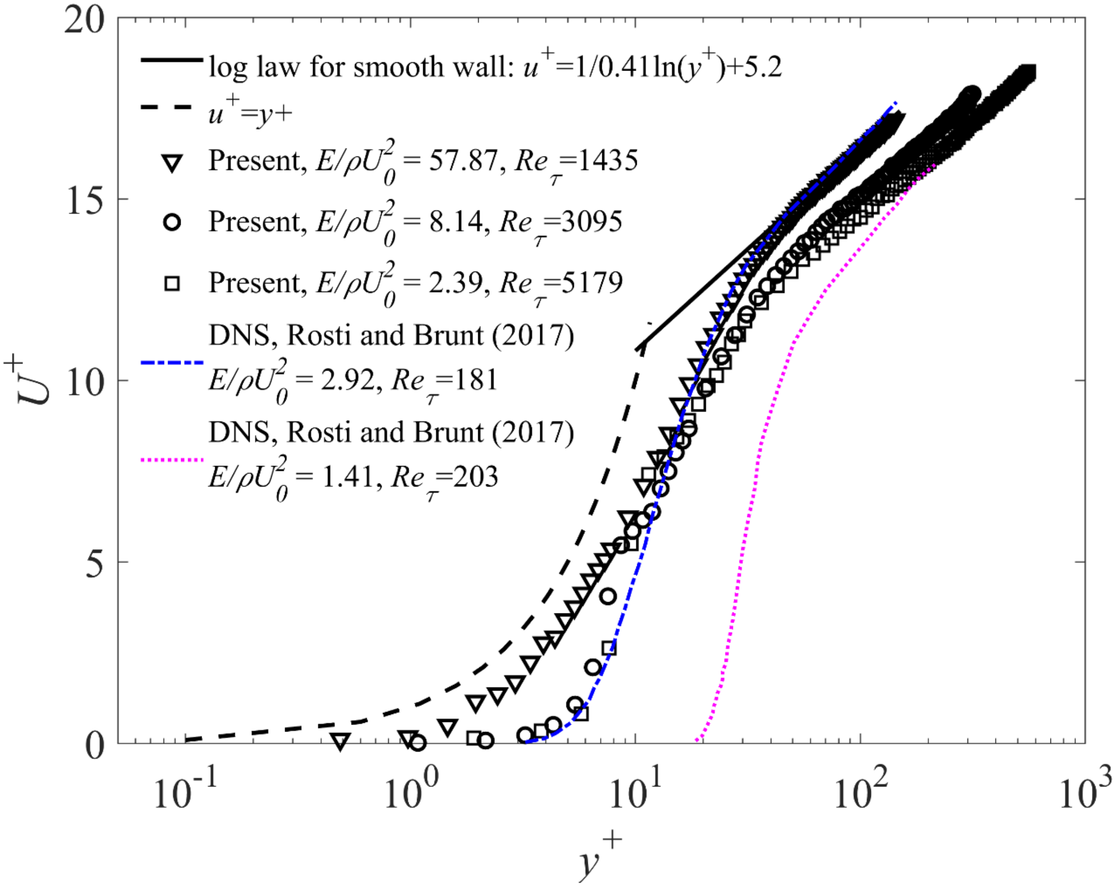

FIGURE 4.22. The mean velocity profiles for the compliant wall turbulent boundary layer are compared with the DNS results of Rosti and Brandt (2017).

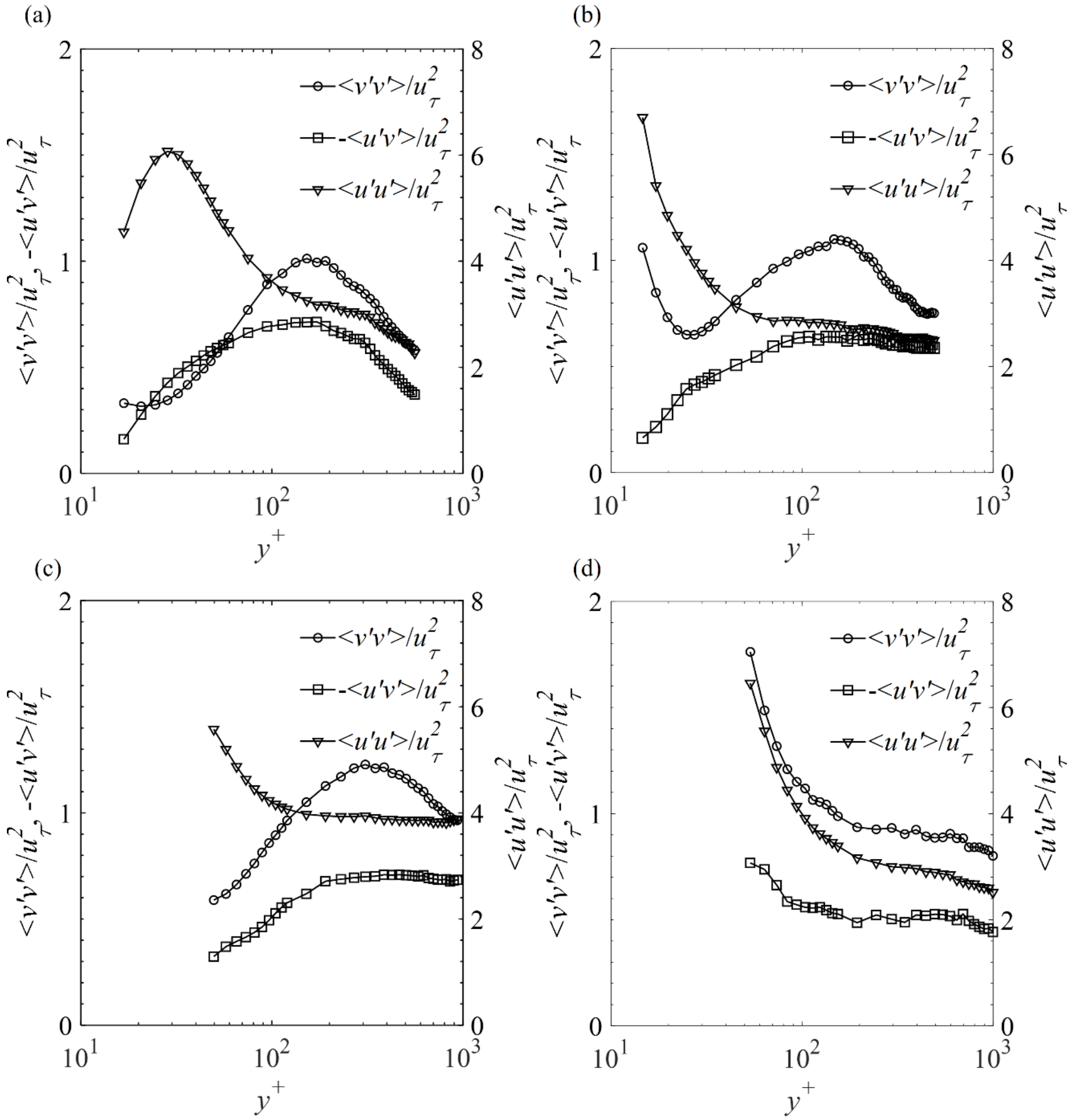

FIGURE 4.23. Reynolds stress profiles calculated using standard 2D PIV for Left column (a, c) a smooth wall; and right column (b, d) the compliant wall. (a, b) U_0=1.2 m/s, and (c, d) U_0=3.2 m/s. The scale for *<v'v'>* and -*<u'v'>* are provided on the left axis, and those for *<u'u'>,* on the right axi*s*.

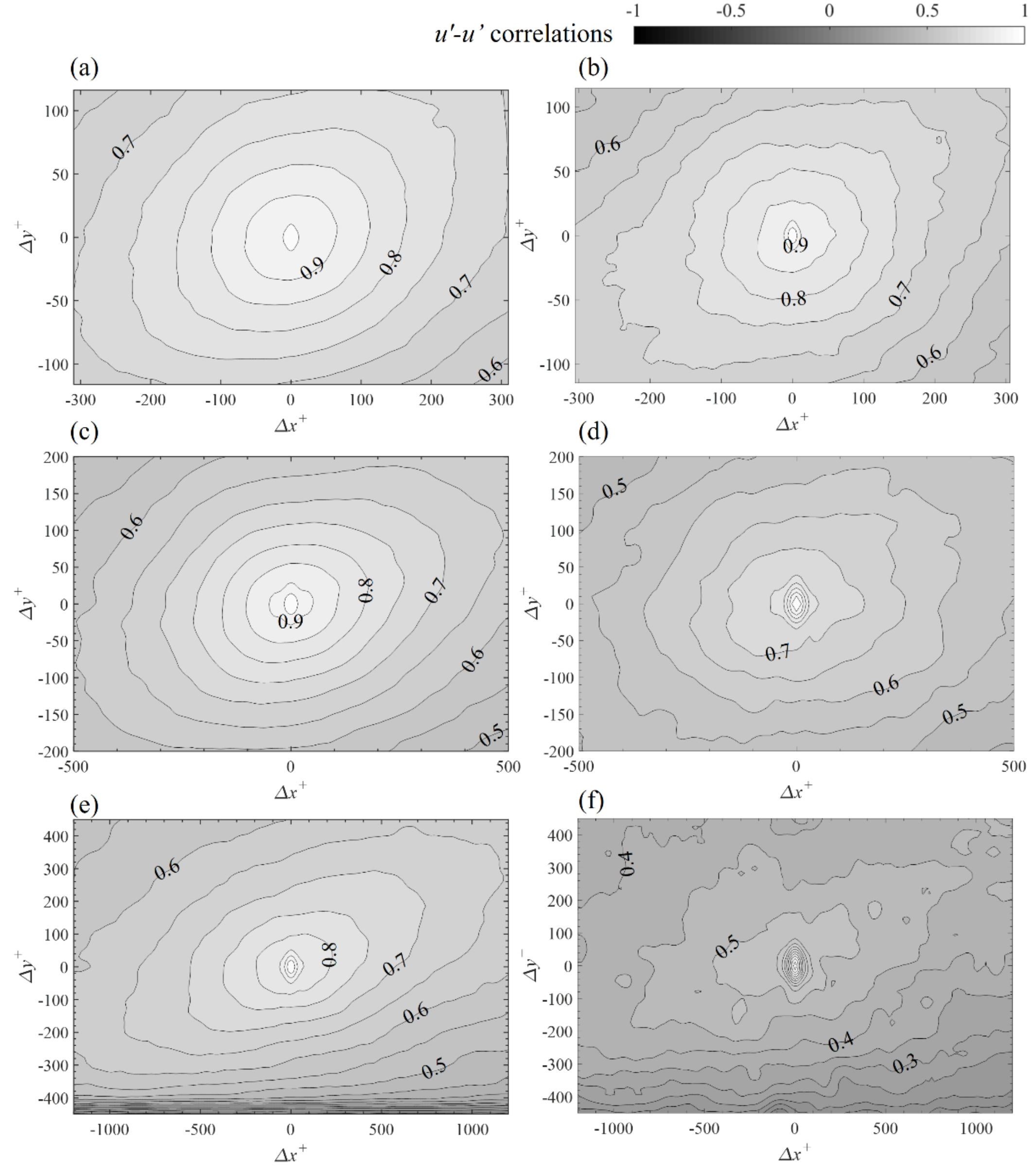

FIGURE 4.24. Two-point correlations of *u*'-*u*' at y^+=600 for: (left colum: a, c, e) smooth wall, and (right column: b, d, f) compliant wall at (a,b) U_0=1.2 m/s, (c, d) U_0=3.2 m/s and (e, f) U_0=5.9 m/s. Incremental increase between contour lines is 0.05.

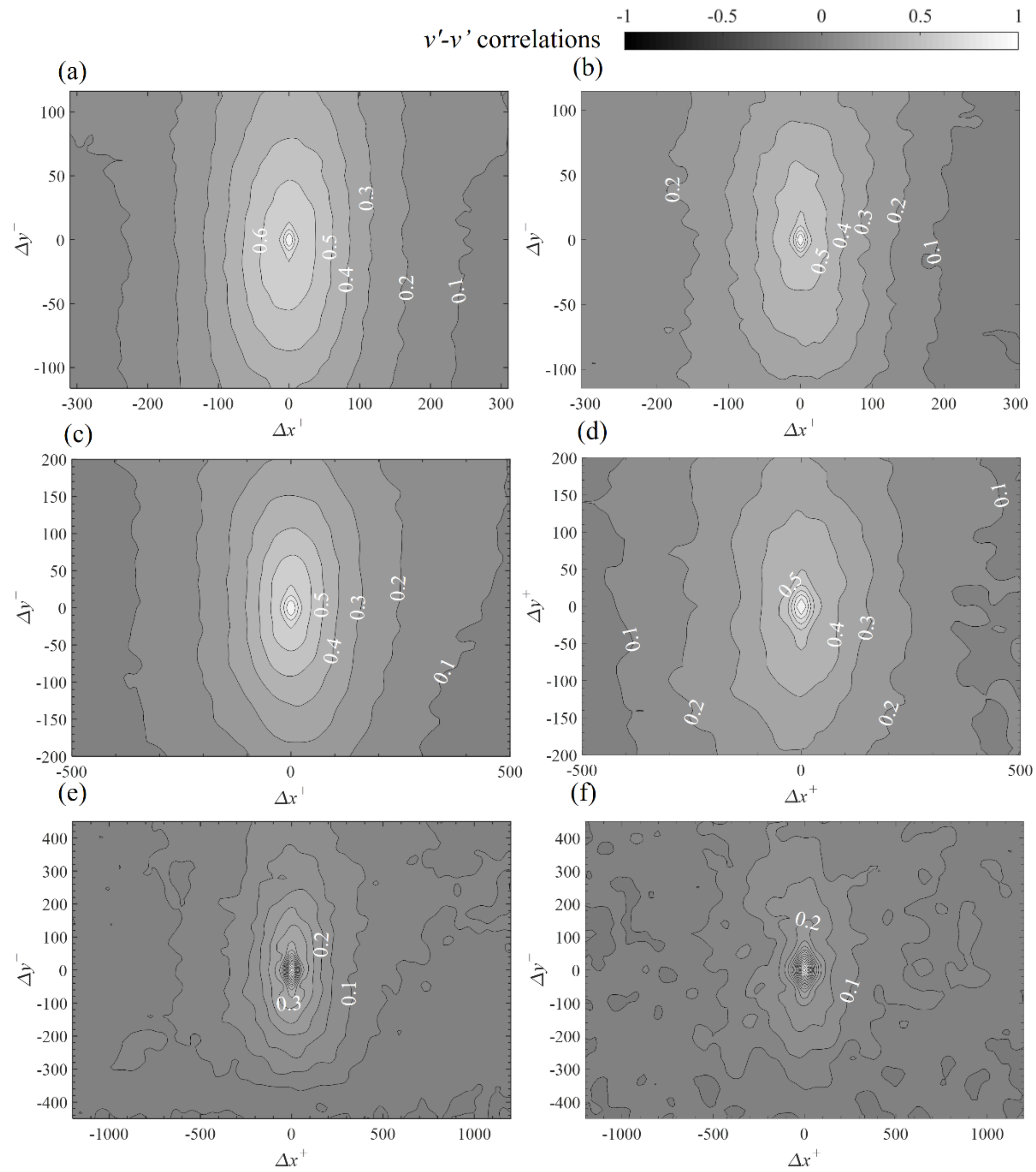

FIGURE 4.25. Two-point correlations of v'-v' at y^+=600 for: (left colum: a, c, e) smooth wall, and (right column: b, d, f) compliant wall at (a,b) U_0=1.2 m/s, (c, d) U_0=3.2 m/s and (e, f) U_0=5.9 m/s. Incremental increase between contour lines is 0.05.

Chapter 5. Application of GPU parallel computing to holographic imaging

In this chapter, the application of GPU parallel computing to the reconstruction and segmentation of holographic PIV will be discussed. The holographic PIV (Sheng et al. 2006, Katz and Sheng 2010) uses a hologram to record the interference fringe pattern of particles. Then the holograms are reconstructed to obtain 3D particle intensity distributions, followed by a segmentation procedure to determine to particle coordinates. The reconstruction and segmentation procedures require around an hour running on CPUs for a single realization. Using GPU parallel computing, the time can be reduced to less than a minute.

5.1. Digital Inline Holography

Holographic imaging involves the recordings of the interference fringe pattern between light scattered by a particle/object in a sample volume and the original reference. There are plenty of holographic optical setups (Katz and Sheng 2010). Among them, the most common one is the inline holography, shown in figure 5.1. A coherent laser beam is collimated, filtered and then used to illuminate a sample volume, in which the flows are seeded with particles. Part of the illumination light is scattered by the particles. Interference fringes between the scattered light and the undisturbed part of the light are recorded by a digital camera. The digital holograms stored in a local computer are numerically reconstructed to obtain the original 3D particle intensity distributions. A subsequent particle segmentation procedure aiming at determining the particle locations would generate a particle list containing the particle coordinates and statistics, e.g. bounding box, number of pixels and mean intensity. The numerical reconstruction involves convolving the hologram with a kernel which represents the light propagating from a point source, as listed in Equation 5.1, where x,y,z is the axis of the sample volume and z is perpendicular to the hologram plane, x_h,y_h is the axis on the hologram plane, $\widetilde{U}_r$ represents the light field. There are two commonly used kernels, i.e. the Rayleigh-Sommerfeld formula: $-\frac{\partial G}{\partial n}(x,y,z)=\frac{1}{\lambda}\frac{\exp(-jkr)}{r}cos\theta$ (λ is the wavelength of the illumination beam and k is the wavenumber, r=$\sqrt{x^2+y^2+z^2}$ and $cos\theta=z/r$) and the Kirchhoff-Fresnel approximation: $-\frac{\partial G}{\partial n}(x,y,z)=\frac{\exp(jkz)}{j\lambda z}\exp[j\frac{k}{2z}(x^2+y^2)]$.

$$\widetilde{U}_r(x,y,z)=\iint_{x_h,y_h}\widetilde{U}_r(\xi,\eta,z=0)\left[-\frac{\partial G}{\partial n}(x-\xi,y-\eta,z)\right]d\xi d\eta \tag{5.1}$$

The convolution (equation 5.1) can be either calculated directly via spatial integration or by multiplication in the frequency domain as denoted in equation 5.2:

$$\widetilde{U}_r(x,y,z)=F^{-1}(F(\widetilde{U}_r)\cdot\tilde{G}) \tag{5.2}$$

Where F represents the Fourier transform and $\tilde{G}=F(-\frac{\partial G}{\partial n})$.

For digital holograms, the discretized forms are $\tilde{G}(m,n)=\exp(-j\frac{2\pi z}{\lambda}\sqrt{1-\left(\frac{\lambda m}{M\Delta x}\right)^2-\left(\frac{\lambda n}{N\Delta x}\right)^2})$ of the Rayleigh-Sommerfeld formula and $\tilde{G}(m,n)=j\lambda exp\left\{-j\lambda z\pi\left[\left(\frac{m}{M\Delta x}\right)^2+\left(\frac{n}{N\Delta y}\right)^2\right]\right\}$ of the Kirchhoff-Fresnel approximation, where M and N are the total number of discretization points (i.e. pixel numbers of the hologram) along the x and y-axis, respectively. The reconstructions are performed plane by plane at different z locations. Typically, it requires 10 minutes to reconstruct 1000 planes for a hologram size of 1024×1024 pixels, if running on a quad-core i7-3770k, 3.6 GHz CPU, which means serval days will be needed to process 1000 realizations, even though this is only the reconstruction part. The convolution is highly parallel and it can be speeded up greatly by using GPU parallel computing.

5.2. GPU based parallel reconstruction and segmentation of digital hologram

Usually, the digital reconstruction procedure is performed using Equation 5.2. The flow chart of reconstruction code running on CPU is illustrated in figure 5.2a, in which numbers in the bracket mean the time needed in milliseconds for each procedure. The CPU used at the present is a quad-core Intel i7-3770k, 3.6 GHz CPU. We rewrote the code using Cuda Toolkit 6.0 and parallelized the reconstruction on a Tesla K40c GPU, as shown in figure 5.2b. The computation time tested using a 1024×1024 pixel hologram for CPU code is 669 ms comparing to 4.9 ms running on GPU, resulting in a speed-up ratio of 137. It should be noted that this speed-up ratio is for single plane reconstruction. As for multiple plane reconstruction, the procedures of reading images and forward FFT don't need to run multiple times, which can push the speed up ratio up to around 200.

The GPU based reconstruction code is validated using a synthetic hologram. A 1 um particle is put at z=100 μm, corresponding interference pattern at z=0 is calculated via Mie scattering theory (Slimani and Allano 1984, Bohren and Huffman 1983), in which the electromagnet of the vector Helmholtz equation is solved in spherical coordinate system. The 128×128 pixel intensity distribution of hologram with a pixel resolution of 0.55um is illustrated in figure 5.3a. Subsequently, the 3D intensity distribution from z=-150 μm to z=+150 μm is reconstructed using the GPU code, using the Rayleigh-Sommerfeld kernel. It should be noted that there is no significant difference between the two kernels (Katz and Sheng 2010). As shown in figure 5.3b, apart from the real particle image located at z=-100 um, a virtual image appears at z=+100 μm in the reconstructed intensity distributions, which is symmetric to the hologram plane. This "twin-image" phenomenon has been observed by others and it will cause trouble by introducing ghost particles into the field of view. Using dual-view inline digital holography, Ling and Katz (2014) have successfully removed the virtual particle image. From dual view hologram, the missing phase information of the hologram can be retrieved iteratively by propagating the wavefield back and forth between the two hologram planes using diffraction theory (Denis et al. 2005). Using the phase information as additional input for the reconstruction procedure, the virtual image could be eliminated. The reconstruction procedure of dual view inline holography has been incorporated into the GPU code, by adding an extra input of the imaginary part of the phase information. When the phase information is missing, this input is set as zero and the code is downgraded to single-view holography.

The 3D intensity distributions could be obtained from the reconstruction procedure. To detect the locations of particles or objects in the field of view, a 2D or 3D segmentation procedure is needed. There are plenty of image segmentation techniques. These techniques either separate the sample area into serval regions by looking at the discontinuity of edges or merge regions by studying the similarities. In this chapter, I'd like to introduce a commonly used algorithm for binary image segmentation, i.e. the connected-component labeling (LCC, Samet and Tamminen 1988) based segmentation technique, in which binary images are generated by thresholding. LCC uniquely labels subsets that are connected based on a given heuristic. This algorithm can be easily implemented on GPU and has been accomplished by Šťava and Beneš (2011). The procedures of 2D segmentation are shown in figure 5.4. After using CCL, each particle is labeled uniquely with an ID number and the background has a label ID of zero. We will use an atomic add function to count the total number of different labels. In the meanwhile, a label array containing all the label ids for each pixel is generated. During this process, each thread is assigned a pixel, if the current label ID of this pixel is not zero, then this label ID is added to the label array. The label array we got is not sorted, and it has duplicate label IDs. Hence, a sorting and reduction procedure based on the CUDA thrust library is utilized to remove the duplicate IDs and sort them in ascending order. The above label counting and sorting as well as reduction procedures are aimed at reducing the memory needed to store the particle list information. Apparently, without counting, sorting, and reduction, one would need a total amount of memory equivalent to the maximum ID. Usually, the maximum ID is equal to the total number of pixels. Considering an image size of 2048×2048 pixels, and 9 single precision numbers (4 Byte) to store the particle information (9 numbers to store particle information shown in figure 5.4), the memory needed will be 2048×2048×9×4 Byte = 144 MB. It's not a big deal for the 2D case, however, when we go to 3D segmentation, a number of 100 planes on the third dimension means more than 14 GB memory required. By using counting, sorting, and reduction, the total number of memory places will be the same as the total number of particles. Given a particle concentration of 0.002, which is dense for the holographic PIV, the memory needed is 3 orders of magnitude smaller. After the label array is obtained, a mapping between the label ID and its storing location in the global memory is produced in the label map. In the final step of the algorithm, information of particles (i.e. pixels having the same ID) regarding the centroid, the bounding box and a total number of pixels is analyzed using the atomic function. The analysis has been performed in parallel, assigning each pixel to a thread. For each pixel, the label ID can be obtained from the CCL result. According to the label ID, one can access the memory location by examining the label map. The 2D CCL based segmentation algorithm can be easily extended to the 3D case.

5.3. Experimental applications of GPU based reconstruction and segmentation

Holography has been widely used to study the 3-D location, motion, and size of particles, droplets, bubbles, and planktons in numerous applications, too many to summarize in a single paper (Katz & Sheng, 2010). In particular, size distributions have been measured by, e.g., Thompson (1974), Katz (1984), Ran and Katz (1991), Malkiel et al. (1999), Fugal and Shaw (2009), Tian et al. (2010), Gao et al. (2013), and Beals et al. (2015). Our code is utilized to study the size distributions of oil droplets in a breaking wave. Detailed descriptions about the facility, setup and results can be found in Li et al. (2017). Holograms of the crude oil droplet entrained in the breaking wave are captured with a magnification of 10, by using a 2016×2016 high-speed PCO camera. The light source of the digital holography system is pulsed, high frequency, low energy Nd: Yag laser (CrystaLaser, model QL532-500, 61 mJ/pulse at 1 kHz). The pixel resolution is 11 μm and the frame rate is 50 fps. figure 5.5 is the processing timeline using CCL based segmentation. As is shown, the majority of time is spent on initialization and memory allocation, which takes 1260 ms. The processing time needed on GPU is only 12 ms and 18 ms is used in outputting the results to the disk. If we run the same algorithm on CPU via the Matlab code, the time needed is 741 ms, ignoring data outputting time. Thus, a speed-up ratio of 25 is achieved. Figure 5.6a shows the reconstructed hologram and figure 5.6b is the droplet found by the segmentation code after thresholding. The droplet centroids calculated by the segmentation algorithm overlap well with the droplet shapes. The current program could not address the cases when two droplets overlap with each other, which should be considered in the future study.

5.4. Conclusions and Discussions

In this chapter, we talked about using GPU parallel computing to speed up the reconstruction as well as segmentation procedures of holographic PIV. A speed-up ratio of around 200 is achieved for the reconstruction part. Using the GPU based segmentation method for the 2D case reduces the processing time by 25. The reconstruction time using GPU (<4 ms) for an image size of 1024×1024 is really appealing. It enables the real-time holographic imaging considering a processing time of less than 41.7 ms is required for the frame rate of 24.

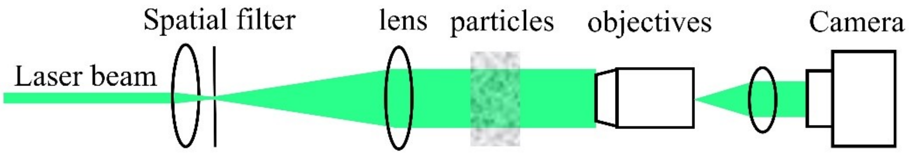

FIGURE 5.1. Optical setup for inline digital holographic PIV.

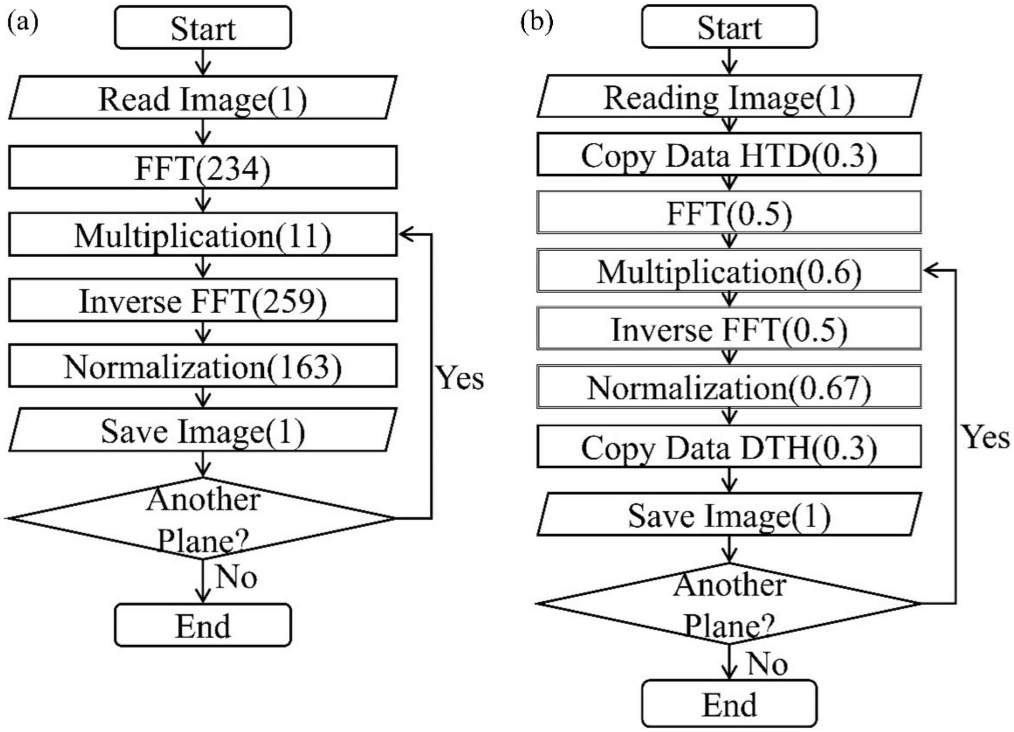

FIGURE 5.2. Flow chart for digital holographic reconstruction, (a) running on quad-core i7-3770k CPU, (b) running on Tesla K40c GPU with a double solid box indicating procedures running on GPU board. The number in the bracket means time in milliseconds for each procedure.

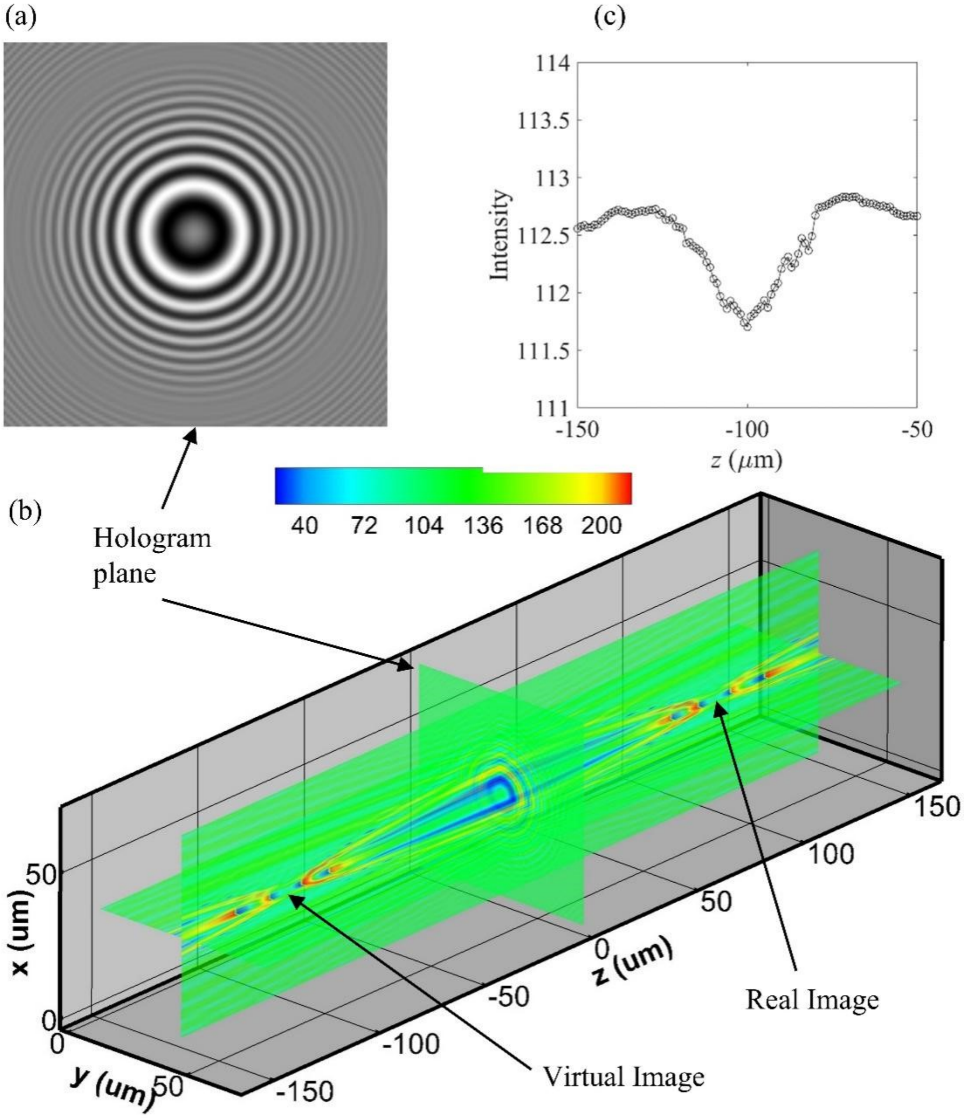

FIGURE 5.3. Synthetic test of the reconstruction code, (a) hologram calculated by Mie scattering theory at *z*=0, with the particle located at *z*=-100 µm, (b) plot of the reconstructed 3D intensity distribution using the GPU code, (c) variation of intensity with *z* averaged on the *x*-*y* plane.

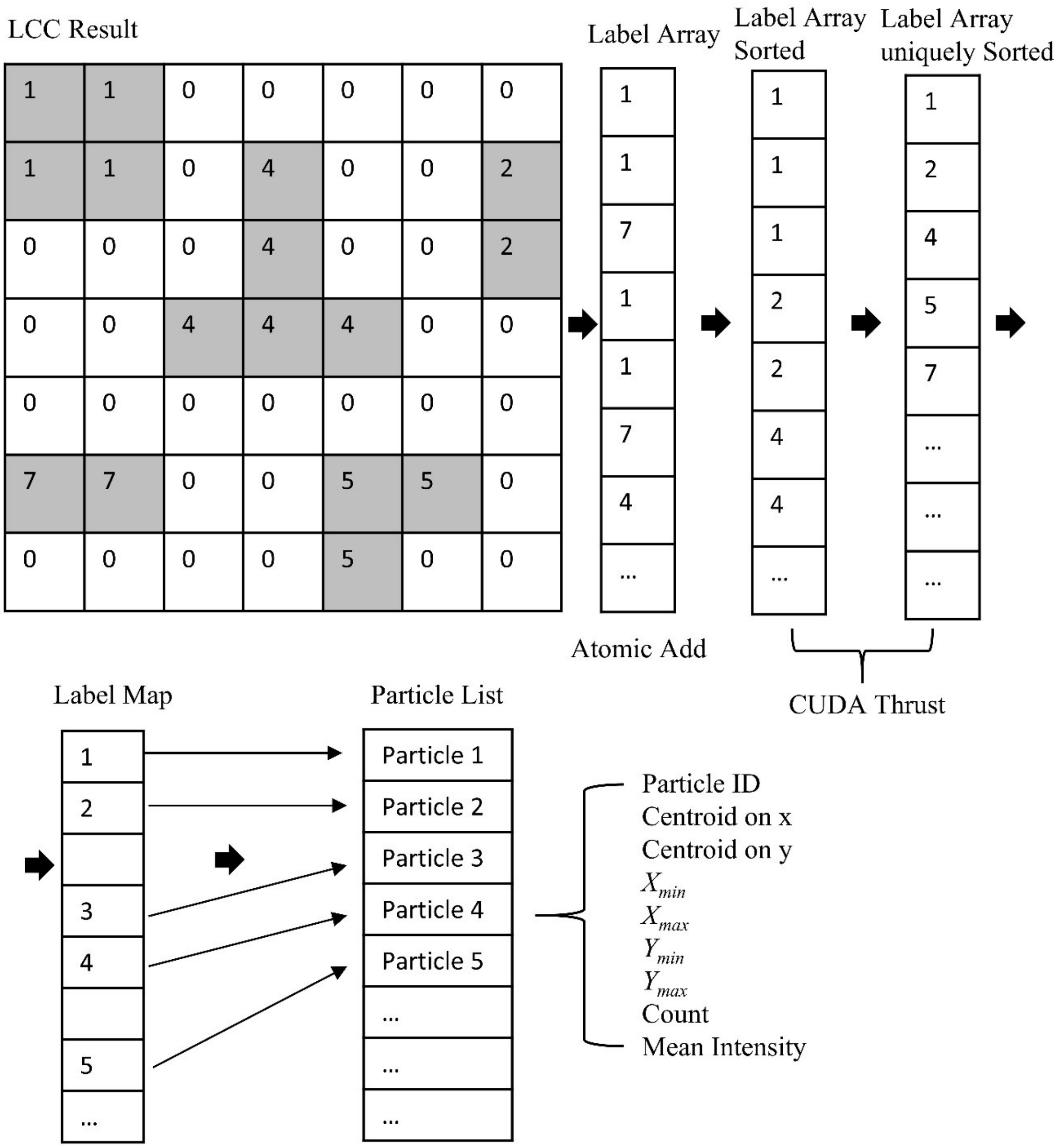

1	1	0	0	0	0	0
1	1	0	4	0	0	2
0	0	0	4	0	0	2
0	0	4	4	4	0	0
0	0	0	0	0	0	0
7	7	0	0	5	5	0
0	0	0	0	5	0	0

FIGURE 5.4. Schematics of the segmentation procedures, with all the procedures running on GPU.

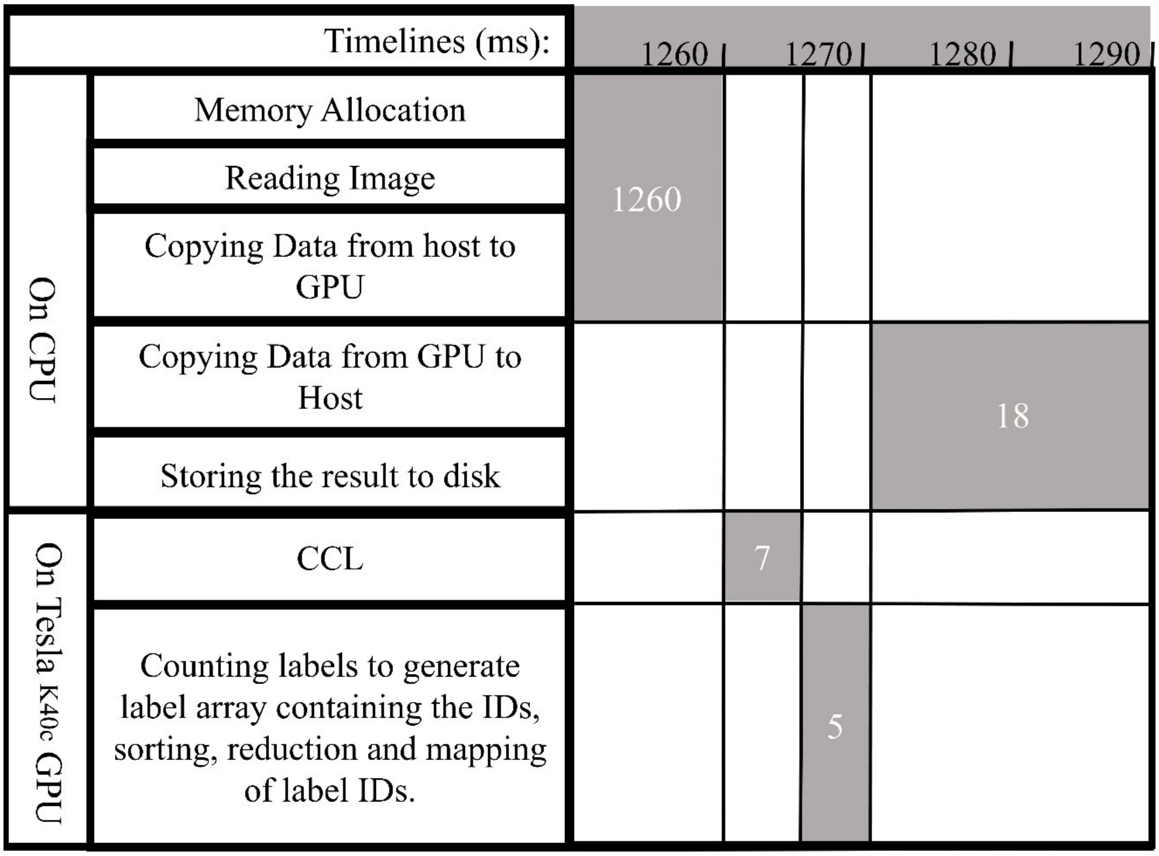

FIGURE 5.5.Timelines for the CCL based segmentation in milliseconds (Image Size: 2016 × 2016).

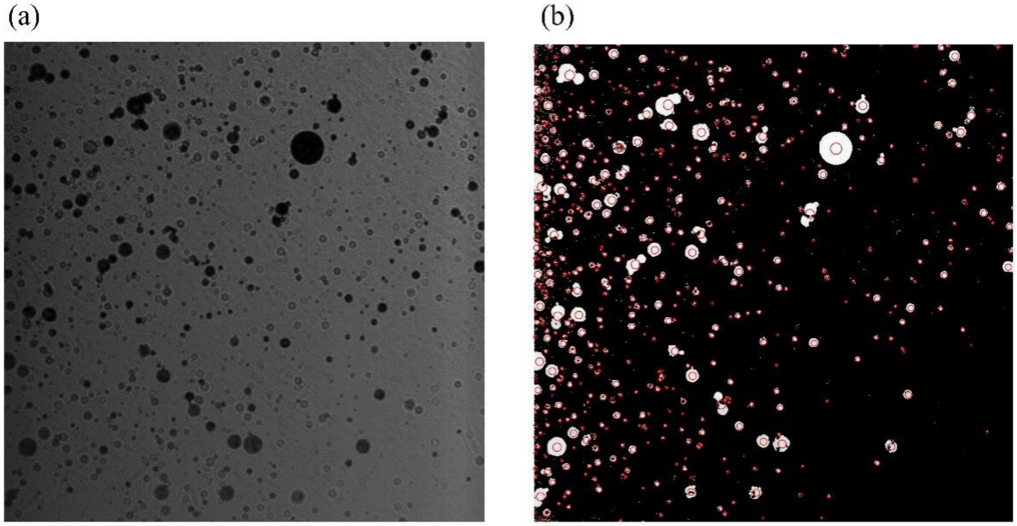

FIGURE 5.6. (a) Reconstructed image of the droplets. (b) Droplets found by the segmentation code (marked as red circles) superimposed on the threshed droplet image.

Chapter 6. Summary and discussion

A 3D GPU-based, parallel-line, omni-directional integration method is developed to calculate the 3D pressure field from TPIV results. This new method has been applied successfully to obtain the pressure in the experiment of turbulent channel flow over a compliant surface. Due to the utilization of a "hard" compliant surface, a one-way coupling between the flow and the deformation is observed. To achieve two-way coupling, we have carefully designed a new experiment using the Chase (1991) model. Compliant coating thickness, the Young modulus as well as the flow speed are selected to ensure that wall deformation is comparable to the wall unit. In this chapter, we will first summarize the Omni3D method focusing on the recent applications and further expansions of the method. In section 5.2, a discussion about the results of the experimental investigations of the turbulent boundary layer over a compliant surface will be presented. At last, we will briefly discuss what to do in future work.

6.1 Omni3D and the recent applications

An efficient three dimensional, parallel-line, omni-directional integration method (Omni3D) is introduced for calculating the pressure distribution from an experimental 3D velocity field. The number of integration directions and distance between parallel lines are matched with the data resolution since a further increase in resolution does not improve the data quality. This method is compared to several approaches, including the previously used Omni2D - the 2D virtual-boundary Omni-directional integration method, and several techniques based on solving the Pressure-Poisson Equation with different Dirichlet boundary conditions. These comparisons are based on using both DNS data for isotropic turbulence and turbulent channel flow as well as experimental data for turbulent channel flow. For the DNS channel flow, the analysis is based on generating synthetic particle fields with varying concentrations, and analyzing the velocity fields following established PIV procedures along with particle tracking augmented by the application of singular value decomposition to maps the data onto a regular grid. Subsequently, the Omni3D method is enhanced by adopting selected and weighted path methods aimed at minimizing the propagation of errors originating from regions where the experimental data have large errors. As implemented, Omni3D offers several advantaged: First, there is no need to specify a Dirichlet boundary condition, as commonly done for PPE-based techniques. Instead, an iterative process matches the pressure distribution along the boundary with the internal pressure gradient field. The self-consistent pressure field only misses a constant value. In the present paper, the spatially-averaged pressure is set arbitrarily to zero. However, this constant could be provided by e.g. a point pressure transducer. Another option to avoid prescribing the Dirichlet pressure distribution in PPE based calculations is to use Omni2D to generate the pressure distribution along this boundary. In flow with low errors in acceleration Omni3D and PPE-Omni2D give the same pressure distributions. In contrast, using other techniques based on e.g. Bernoulli's eqn. generates large errors near the Dirichlet boundary. These errors decay with increasing distance from the boundary.

Second, Omni3D involved homogeneous integration from all possible directions from the boundary to internal points, preventing any bias in direction, and minimizing the impact of random errors on the pressure distribution. Paths with particularly large errors in pressure gradients, evaluated from the magnitudes of their curl can be readily avoided. The present tests demonstrate that the weighted path Omni3D method is effective in preventing the propagation of errors. Hence, it is strongly recommended to use the weighted path method instead of using simple Omni3D. Third, Omni3D can be readily adopted for complex boundaries, including compound ones by terminating the integration along any path and at any point, and restarting it on the opposing boundary, the so-called selected path method. Fourth, while Omni3D involves massive computations, the procedures can be readily parallelized. Using a GPU-based code, the pressure computation is accelerated by more than two orders of magnitudes, enabling efficient processing of large databases.

The error analysis using synthetic data demonstrates the sensitivity of all the methods for calculating the pressure to the wall-normal resolution of the velocity distribution in the inner part of the boundary layer. It appears that the error decreases substantially as the wall-normal resolution is reduced to about five wall units, a challenge for high Reynolds number flows. Furthermore, the impact of the viscous terms in the inner part of boundary layers is not negligible, and so is the effect of sub-grid stresses, which increases with decreasing resolution. Significant improvements are achieved using particle tracking-based data, and projecting it onto the regular grid using SVD, which accounts for the exact position of each particle relative to the grid point. In this context, as discussed, the present Omni3D implementation is based on an Eulerian Cartesian coordinate system and involves integration steps along with grid points, which have minimal distance from the prescribed parallel line. As noted before, with the recent development of 4D-PTV methods, such as the Shake-The-Box (Daniel et al. 2016), a Voronoi-based integration method (Neeteson et al. 2015) can be used for determining the pressure by applying PPE on the unstructured data (Gent et al. 2017). Although not done in this paper, Omni3D can be readily implemented in an unstructured system by integration from particle to particle subject to a prescribed constraint on the distance from the integration path. This approach will be implemented and evaluated in future efforts.

Recently, Karuna et al. (2019) measured the 3D velocity distributions of the turbulent boundary layer over a backward-facing step. In the experiment, the Shake-The-Box method is utilized to obtain the Lagrangian tracks of the particle. However, their particle concentrations are sparse, preventing using a simple interpolation scheme to obtain the velocity and material acceleration on the Euler grid. In the paper, a Constrained Cost Minimization (CCM) technique to interpolate unstructured sparse particle tracks and get velocity, velocity gradients, material acceleration, and hence the pressure on Eulerian grids is introduced. The technique incorporates known information like the divergence-free condition of velocity and curl-free condition of material acceleration to improve the reliability of reconstruction of the flow, compensating for sparse data. Material accelerations are obtained for each particle and then interpolated onto the Euler grid. Subsequently, the 3D pressure field is obtained from the material acceleration on the Euler grid. Instead of integrating the interpolated material acceleration, we could also do the integration on the unstructured grid as discussed. The development of the Omni3D based on the unstructured grid is promising. A comparison between those two approaches should be performed in the future development of Omni3D.

6.2 Experimental investigation of turbulent flow over a compliant surface

In the experiment of turbulent channel flow over a compliant surface who has Young's modulus of around 1 MPa and $E/\rho U_0^2$=220, the measured surface deformation is in submicron (δ_v=11μm). One way of coupling between the deformation and the turbulent channel flow is observed. The deformation bumps are associated with sweep and ejection transition whereas the deformation dimples are located under a hairpin-like structure. The mean velocity profile and Reynolds stress profiles are found to be the same with a rigid wall turbulent boundary layer (Zhang et al. 2017). In the present experiment, a softer compliant surface whose Young's modulus is 158 kPa ($E/\rho U_0^2$ ranges from 59.0 to 2.4) has been used. Deformation magnitude is increased from submicron to serval wall units. The surface deformations are found to affect the turbulent boundary layer even when it's much smaller than a wall unit (0.02 δ_v). The turbulent boundary layer is altered by the surface deformation in three aspects. First, there is a sharp decrease in the mean velocity at the viscous sublayer and a momentum deficit at the log layer. Second, the compliant surface deformation will increase all the components of the Reynolds stress. Third, the correlation length scales are reduced both in the streamwise and wall-normal directions. These findings are consistent with the DNS results of Rosti and Brandt (2017). They also reported an increase in the spanwise length scale, which is supposed to be associated with the spanwise aligned deformation pattern. Although the spanwise information is lacked in our current experiment, we can still see that the deformations become spanwise oriented when the flow speed increases. At the lowest flow speed, when the deformation magnitude is significantly smaller than a wall unit, slight differences are observed in the wall shear stress between the compliant wall and the rigid smooth wall turbulent boundary layer. It's mentioned by Choi et al. (1997) that for this type of compliant wall (hydrodynamical smooth), a careful selection of material properties would introduce turbulent drag reduction. Currently, the wall shear stress is estimated from the log fit of the mean velocity profile. A more accurate way to calculate the wall shear stress should be used in order to draw a conclusion on the drag reduction. In the deformation measurement, two modes of deformation are observed, the first mode is caused by the flow and its advection speed is $0.66U_{0.}$ The advection speed is lower than the flow mode ($0.72U_0$) we found in the previous experiment. The second mode is a spanwise-propagating wave who has a phase speed of the shear speed. These waves are high in frequency, thus it's not fully resolved by our current measurement. For the future experiment, an MZI with higher sampling rates is needed to capture them.

6.3 Questions for future investigations

In the current experiment, the compliant coating is attached to the acrylic base using physical bondings, and no chemical bonding is used. Thus, the surface is easily peeled off by part when the flow speed is increased to 6 m/s and the facility has been running for serval hours. During the experiment, we have to install the surface multiple times. In future experiments, if measurements of the compliant surface deformation are not required, the author would suggest using chemical bondings to further fasten the surface. In the data analysis, pressure spectra are needed for modeling the surface response using the Chase or Benschop model. However, lacking pressure information, we have used the spectra form Tsuji et al. (2007) and Goody (2004). It should be noted that pressure spectra for compliant wall turbulent boundary layer might be different from the rigid wall case because of the two-way coupling. Thus, a further scrutinize of the pressure either by a pressure transducer or the Omni3D integration from PIV results is necessary. As discussed, the Omni3D integration result is missing a time-dependent pressure constant, which should be compensated e.g. from the measurement by pressure taps. The goal of studying turbulent flow over a compliant surface is to investigate the possible drag reduction and noise suppression. To the author's knowledge, a turbulent drag reduction could be achieved by careful selections of material properties, i.e. making the surface deformation smaller than a wall unit and deformation velocity large enough to affect the flow (Choi 2000, Choi et al. 1994, 1997a, Kulik et al. 1991). In our current experiment, the deformation velocity and deformation magnitude normalized by inner variables are of the same order for the lowest flow speed. As a result, the wall shear stress of the compliant wall is very close to that of a stiff wall. Noise suppression should be quantified by correlating the pressure fluctuations in the turbulent boundary layer to acoustic noise. This should also be done in future work.

Appendix A: Omni3D Boundary Iteration

After boundary integration in PLODI, we obtained a set of equations which quantify the pressure difference (PINT) between two different boundary nodes (n_{in}, n_{out}) as follows:

$$\mathrm{P(nout) - P(nin) = PINT(nin, nout), nout} \in [1, N\mathrm{surface}], \mathrm{nin} \in [1, N\mathrm{surface}]$$

where $N_{surface}$ is the total number of boundary nodes. These equations can be described by A*P=PINT, in which A is an ($N_{surface}$ -1)× $N_{surface}$ by $N_{surface}$ rectangular matrix, and

$$A_{i,j} = \begin{cases} 1 & \frac{i-1}{N\mathrm{surface}-1} + 1 = j) \\ -1 & i\%(N\mathrm{surface} - 1) = \mathrm{j} + 1 \text{ and } \mathrm{j} > \frac{i-1}{N\mathrm{surface}-1} + 1 \\ -1 & i\%(N\mathrm{surface} - 1) = \mathrm{j} \text{ and } \mathrm{j} < \frac{i-1}{N\mathrm{surface}-1} + 1 \end{cases} \quad \text{A.1}$$

For other cases, $A_{i,j}$ =0;

As an overdetermined linear system, it is solvable by a least-square fit.

$$A^T AP = A^T PINT \quad \text{A.2}$$

The $N_{surface}$ × $N_{surface}$ square matrix, C=$A^T A$, has the following values:

$$C_{i,j} = \begin{cases} -2 & (i \neq j) \\ (N\mathrm{surface} - 1) * 2 & (i = j) \end{cases} \quad \text{A.3}$$

and $B = A^T PINT$ is an $N_{surface}$ × 1 matrix:

$$B_{i,1} = -\sum_{nout=1}^{N\mathrm{surface}} PINT(i, nout) + \sum_{nin=1}^{N\mathrm{surface}} PINT(nin, i) \quad \text{A.4}$$

The resulting square linear system can be solved by a Jacobi iteration

$$C_{i,i} P_i^{new} = \sum_{j=1, i\neq j}^{N\mathrm{surface}} -C_{i,j}\, P_j^{old} + B_{i,1} \quad \text{A.5}$$

The iteration formula is:

$$P_i^{new} = \frac{2\sum_{j=1,i\neq j}^{N\mathrm{surface}} P_j^{old} - \sum_{nout=1}^{N\mathrm{surface}} PINT(i,nout) + \sum_{nin=1}^{N\mathrm{surface}} PINT(nin,i)}{2(N\mathrm{surface}-1)} \quad \text{A.6}$$

$$P_i^{new} = \frac{\sum_{nout=1,i\neq nout}^{N\mathrm{surface}} (P_{nout}^{old} - PINT(i,nout)) + \sum_{nin=1,nin\neq i}^{N\mathrm{surface}} (P_{nin}^{old} + PINT(nin,i))}{2(N\mathrm{surface}-1)} \quad \text{A.7}$$

Apply $\mathrm{PINT(nin, nout) = -PINT(nout, nin)}$

$$P_i^{new} = \frac{\sum_{nout=1,i\neq nout}^{N\mathrm{surface}} (P_{nout}^{old} + PINT(nout,i)) + \sum_{nin=1,nin\neq i}^{N\mathrm{surface}} (P_{nin}^{old} + PINT(nin,i))}{2(N\mathrm{surface}-1)} \quad \text{A.8}$$

$$P_i^{new} = \frac{\sum_{nin=1,nin\neq i}^{N\text{surface}}(P_{nin}^{old}+PINT(nin,i))}{N\text{surface}-1} \tag{A.9}$$

i.e.

$$P_{nout}^{new} = \frac{\sum_{nin=1,nin\neq nout}^{N\text{surface}}(P_{nin}^{old}+PINT(nin,nout))}{N\text{surface}-1} \tag{A.10}$$

Hence, this iteratively solved boundary pressure is equivalent to a least-square fit of the known pressure differences between boundary nodes. This formula is used in the presently introduced iteration scheme for calculating the pressure distribution along the boundary of the sample volume.

$$\begin{array}{c} A \\ \begin{array}{|c|c|c|c|} \hline 1 & -1 & & \\ \hline 1 & & -1 & \\ \hline 1 & & & -1 \\ \hline -1 & 1 & & \\ \hline & 1 & -1 & \\ \hline & 1 & & -1 \\ \hline -1 & & 1 & \\ \hline & -1 & 1 & \\ \hline & & 1 & -1 \\ \hline -1 & & & 1 \\ \hline & -1 & & 1 \\ \hline & & -1 & 1 \\ \hline \end{array} \end{array} \quad \begin{array}{c} P \\ \begin{array}{|c|} \hline P_1 \\ \hline P_2 \\ \hline P_3 \\ \hline P_4 \\ \hline \end{array} \end{array} \quad \begin{array}{c} PINT \\ \begin{array}{|c|} \hline \text{PINT(1,2)} \\ \hline \text{PINT(1,3)} \\ \hline \text{PINT(1,4)} \\ \hline \text{PINT(2,1)} \\ \hline \text{PINT(2,3)} \\ \hline \text{PINT(2,4)} \\ \hline \text{PINT(3,1)} \\ \hline \text{PINT(3,2)} \\ \hline \text{PINT(3,4)} \\ \hline \text{PINT(4,1)} \\ \hline \text{PINT(4,2)} \\ \hline \text{PINT(4,3)} \\ \hline \end{array} \end{array}$$

Figure A.1 the Matrix in Eqn. A.1

Bibliography

ATKINSON, C. COUDERT, S. FOUCAUT, J.M. et al. 2011 The accuracy of tomographic particle image velocimetry for measurements of a turbulent boundary layer. Exp Fluids 50: 1031

BENJAMIN, T. B. 1960 Effects of a flexible boundary on hydrodynamic stability. J. Fluid Mech. 9, 513–532.

BENJAMIN, T. B. 1963 The threefold classification of unstable disturbances in flexible surfaces bounding inviscid flows. J. Fluid Mech. 16, 436–450.

BENSCHOP, H. O. G. GREIDANUS, A. J. DELFOS, R. WESTERWEEL, J. & BREUGEM, W.-P. 2019 Deformation of a linear viscoelastic compliant coating in a turbulent flow. J. Fluid Mech. 859,613–658.

BLAKE, W. 2017 Mechanics of Flow-induced Sound and Vibration. Academic.

BUKOV, A.P., ORLOV, A. A., MOSHAROV V. E., RADCHENKO, V. N., PESETSKY, V.A., SOROKIN, A. V., PHONOV, S.D., ALATY, L. and COLUCCI, V. 1992 Application of Luminescent Quenching for Pressure Field Measurements on the Model Surface in a Wind Tunnel, Wind Tunnels and Wind Tunnel Test Techniques, The Royal Aeronautical Society, Southhampton University, United Kingdom, September

BLICK, E. F. & WALTERS, R. R. 1968 Turbulent boundary-layer characteristics of compliant surfaces. J. Aircraft 5(1), 11–16.

BRERETON, G. J. & HWANG, J. L. 1994. The spacing of streaks in unsteady turbulent wall-bounded flow. Phys. Fluids 6,2446–2454.

BROOKE BENJAMIN, T. 1963. The threefold classification of unstable disturbances in flexible surfaces bounding inviscid flows. J. Fluid Mech. 16,436–450.

BURATTINI, P. LEONARDI, S. ORLANDI, P. & ANTONIA, R. A. 2008. Comparison between experiments and direct numerical simulations in a channel flow with roughness on one wall. J. Fluid Mech. 600,403–426.

CARPENTER, P. W. 2013 the Hydrodynamic Stability of Flows Over Simple Non-Isotropic Compliant Surfaces. Frontiers of Fluid Mechanics (Vol. 170).

CASTELLINI, P. MARTARELLI, M. & TOMASINI, E. P. 2006 Laser Doppler Vibrometry: Development of advanced solutions answering to technology's needs. Mech. Syst. Signal Process. 20,1265–1285.

CHARRUAULT, F. GREIDANUS, A. & WESTERWEEL, J. 2018 A dot tracking algorithm to measure free surface deformations. 18th Int. Symp. Flow Vis. paper 042.

CHARONKO, J.J. KING, C.V., SMITH, B.L. & VLACHOS, P.P. 2010 Assessment of pressure field calculations from particle image velocimetry measurements, Meas. Sci. Technol. 21,105401

CORCOS, G.M. 1963 Resolution of pressure in turbulence. J. Acoustic. Soc. Am. 35, 192–199.

CHASE, D. M. 2005 Generation of fluctuating normal stress in a viscoelastic layer by surface shear stress and pressure as in turbulent boundary-layer flow. J. Acoust. Soc. Am. 89,2589–2596.

CHOI, H. & MOIN, P. 1990 On the space-time characteristics of wall-pressure fluctuations. Phys. Fluids A 2,1450–1460.

DE KAT, R. VAN OUDHEUSDEN, B.W. 2012 Instantaneous planar pressure determination from PIV in turbulent flow, Exp Fluids, 52:1089-1106

DE SILVA, M. BAIDYA, R. KHASHEHCHI, M. MARUSIC, I. 2011 Assessment of tomographic PIV in wall-bounded turbulence using direct numerical simulation data, Exp Fluids 52:425–440

DJENIDI, L. ANTONIA, R. A. AMIELH, M. & ANSELMET, F. 2008 A turbulent boundary layer over a two-dimensional rough wall. Exp. Fluids 44,37–47.

DUNCAN, J. H. 1986 The response of an incompressible, viscoelastic coating to pressure fluctuations in a turbulent boundary layer. J. Fluid Mech. 171,339–363.

ELSINGA, G. E. SCARANO, F. WIENEKE, B. VAN OUHEUSDEN B. W. 2005 Tomographic particle image velocimetry. 6th International Symposium on Particle Image Velocimetry, 1–12.

ENDO, T. & HIMENO, R. 2002 Direct numerical simulation of turbulent flow over a compliant surface. J. Turbul. 3, 1–10.

FISHER, D. H. & BLICK, E. F. 1966 Turbulent damping by flabby skins. J. Aircraft 3(2), 163–164.

GHAEMI, S. RAGNI, D. SCARANO, F. 2012 PIV-based pressure fluctuations in the turbulent boundary layer. Experiments in Fluids, 53(6), 1823–1840.

GHAEMI, S. SCARANO, F. 2013 Turbulent structure of high-amplitude pressure peaks within the turbulent boundary layer. Journal of Fluid Mechanics, 735, 381–426.

GAO, J. & KATZ, J. 2018 Self-calibrated microscopic dual-view tomographic holography for 3D flow measurements. Opt. Express 26,16708.

GHIGLIA, D. C. MASTIN, G. A. & ROMERO, L. A. 1987 Cellular-automata method for phase unwrapping. J. Opt. Soc. Am. A 4,267.

GRAHAM, J. KANOV, K. YANG, X. Lee, M.K. MALAYA, N. LALESCU, C. C. BURNS, R. EYINK, G. SZALAY, A. MOSER, R. D. and MENEVEAU, C. 2016 A Web Services-accessible database of turbulent channel flow and its use for testing a new integral wall model for LES. Journal of Turbulence 17(2), 181-215

GOLDSTEIN, R. M. ZEBKER, H. A. & WERNER, C. L. 1988 radar interferometry: Two-dimensional phase unwrapping 23,713–720.

GOODY, M. 2004 Empirical Spectral Model of Surface Pressure Fluctuations. AIAA J. 42,1788–1794.

GOLUB, G.H. LOAN, C.F.V. 1996 Matrix computation, JHU Press

GRANT, I. 2000 Particle Image Velocimetry 56,55–76.

HANSEN, R. J. & HUNSTON, D. L. 1974 An experimental study of turbulent flows over compliant surfaces. J. Sound Vib. 34, 297–308.

HANSEN, R. J. & HUNSTON, D. L. 1983 Fluid-property effects on flow-generated waves on a compliant surface. J. Fluid Mech. 133, 161–177.

HANSEN, R. J., HUNSTON, D. L., NI, C. C. & REISCHMAN, M. M. 1980 An experimental study of flow-generated waves on a flexible surface. J. Sound Vib. 68, 317–334.

HARRIS, G. L. & LISSAMAN, P. B. S. 1969 Turbulent skin friction on compliant surfaces. AIAA J. 7(8), 1625–1627.

HANSEN, R. J. & HUNSTON, D. L. 1974 an Experimental Study of Turbulent Flows Over Compliant Surfaces. J. Sound Vib. 34,297–308.

HESS, D. E. PEATTIE, R. A. & SCHWARZ, W. H. 1993 A noninvasive method for the measurement of flow-induced surface displacement of a compliant surface. Exp. Fluids 14,78–84.

HONG, J. KATZ, J. MENEVEAU, C. & SCHULTZ, M. P. 2012 Coherent structures and associated subgrid-scale energy transfer in a rough-wall turbulent channel flow. J. Fluid Mech. 712,92–128.

HONG, J. KATZ, J. & SCHULTZ, M. P. 2011 Near-wall turbulence statistics and flow structures over three-dimensional roughness in a turbulent channel flow. J. Fluid Mech. 667,1–37.

HUNSTON, D. L. 1983 Fluid-property effects on flow-generated waves on a compliant surface. J. Fluid Mech. 133,161–177.

IKEDA, T. & DURBIN, P. A. 2007 Direct simulations of a rough-wall channel flow. J. Fluid Mech. 571,235–263.

JIMENEZ, J. 2003 Turbulent Flows Over Rough Walls. Annu. Rev. Fluid Mech. 36,173–196.

JIMENEZ, J. and HOYAS, S. 2008 Turbulent fluctuations above the buffer layer of wall-bounded flows, J. Fluid Mech. Vol. 611, pages 215-236

JOSHI, P. Liu, X. Katz, J. 2014 Effect of mean and fluctuating pressure gradients on boundary layer turbulence. Journal of Fluid Mechanics, 748, 36–84.

KIM, E. & CHOI, H. 2014 Space-time characteristics of a compliant wall in a turbulent channel flow. J. Fluid Mech. 756, 30–53.

KIM, J. 1983 On the structure of wall bounded turbulent flows. *Phys. Fluids* **26**, 2088–2097.

KIM, J. 1989 On the structure of pressure fluctuations in simulated turbulent channel flow. J. Fluid Mech. 205, 421–451.

KIM, E. & CHOI, H. 2014 Space-time characteristics of a compliant wall in a turbulent channel flow. J. Fluid Mech. 756,30–53.

KIM, J. & MOSER, R. 2019 Turbulence statistics in fully developed channel flow at low Reynolds number. J. Fluid Mech 177,133–166.

KO, S. H. & SCHLOEMER, H. H. 1989 Calculations of turbulent boundary-layer pressure fluctuations transmitted into a viscoelastic layer," J. Acoust. Soc. Am. 85, 1469-1477.

KOBASHI, Y. & ICHIJO, M. 1986 Wall pressure and its relation to turbulent structure of a boundary layer. Exp. Fluids 4, 49–55.

KRAMER, M. O. 1957 Boundary-layer stabilization by distributed damping. J. Aero. Sci. 24, 459–460.

KRAMER, M. O. 1962 Boundary-layer stabilization by distributed damping. Naval Eng. J. 74(2), 341–348

KULIK, V. M. 1997 Turbulent drag reduction using compliant surfaces. Proc. R. Soc. Lond. A 453, 2229–2240.

MOSER, R. KIM, J. MANSOUR 1999 Direct numerical simulation of turbulent channel flow up to Re_{τ}=590, Physics Of Fluids Volume 11, Number 4

LANDAHL, M. T. 1962 On the stability of a laminar incompressible boundary layer over a flexible surface. J. Fluid Mech. 13, 609–632.

LECORDIER, B. WESTERWEEL, J. 2004 The EUROPIV Synthetic Image Generator (S.I.G.). In: Stanislas M., Westerweel J., Kompenhans J. (eds) Particle Image Velocimetry: Recent Improvements. Springer, Berlin, Heidelberg

LEE, M. & MOSER R. D. 2015 Direct numerical simulation of turbulent channel flow up to $Re_\tau \approx 5200$. J. Fluid Mech. 774, 395–415.

LEE, S. H. & SUNG, H. J. 2007 Direct numerical simulation of the turbulent boundary layer over a rod-roughened wall. J. Fluid Mech. 584,125–146.

LEE, T., FISHER, M. & SCHWARZ, W. H. 1993a Investigation of the stable interaction of a passive compliant surface with a turbulent boundary layer. J. Fluid Mech. 257, 373–401.

LEE, T., FISHER, M. & SCHWARZ, W. H. 1993b The measurement of flow-induced surface displacement on a compliant surface by optical holographic interferometry. Exp. Fluids 14, 159–168.

LEE, T., FISHER, M. & SCHWARZ, W. H. 1995 Investigation of the effects of a compliant surface on boundary-layer stability. J. Fluid Mech. 288, 37–58.

LI, Y. CHEN, H. & KATZ, J. 2017 Measurements and Characterization of Turbulence in the Tip Region of an Axial Compressor Rotor. J. Turbomach. 139,121003.

LING, H. SRINIVASAN, S. GOLOVIN, K. MCKINLEY, G. H. TUTEJA, A. & KATZ, J. 2016 High-resolution velocity measurement in the inner part of turbulent boundary layers over super-hydrophobic surfaces. J. Fluid Mech. 801,670–703.

LIU, X. & KATZ, J. 2006 Instantaneous pressure and material acceleration measurements using a four-exposure PIV system. Experiments in Fluids, 41(2), 227–240.

LIU, X. & KATZ, J. 2008 Cavitation phenomena occurring due to interaction of shear layer vortices with the trailing corner of a two-dimensional open cavity, Physics Of Fluids 20, 041702.

LIU, X. & KATZ, J. 2013 Vortex-corner interactions in a cavity shear layer elucidated by time-resolved measurements of the pressure field. Journal of Fluid Mechanics, 728, 417–457.

LIU, X. MORETO, J.R. SIDDLE-MITCHELL, S. 2016 Instantaneous Pressure Reconstruction from Measured Pressure Gradient using Rotating Parallel Ray Method, 54th AIAA Aerospace Sciences Meeting San Diego, California, USA

LIU, X. & KATZ, J. 2018 Pressure–Rate-of-Strain, Pressure Diffusion, and Velocity–Pressure-Gradient Tensor Measurements in a Cavity Flow AIAA Journal

LUHAR, M., SHARMA A. S. & MCKEON, B. J. 2015 A framework for studying the effect of compliant surfaces on wall turbulence. J. Fluid Mech. 768, 415–441.

LYNCH, K. & SCARANO, F. 2013 A high-order time-accurate interrogation method for time-resolved PIV, Meas. Sci. Technol. 24 035305

LYNCH, K. SCARANO, F. 2014 Material acceleration estimation by four-pulse tomo-PIV, Meas. Sci. Technol. 25 084005

MCKEON, B. J. & SHARMA, A. S. 2010 A critical-layer framework for turbulent pipe flow. J. Fluid Mech. 658, 336–382.

MCMICHAEL, J. M., KLEBANOFF, P. S. & MEASE, N. E. 1980 Experimental investigation of drag on a compliant surface. In Viscous Flow Drag Reduction (ed. G. R. Hough), vol. 72, pp. 410–438. AIAA.

MORRIS, M.J. 1995 Use of Pressure-Sensitive Paints in Low Speed Flows, CH34827-95, IEEE 16th International Congress on Instrumentation in Aerospace Simulation Facilities (ICIASF), Wright-Patterson AFB, OH, pp.31.1-10

NAKA, Y. STANISLAS, M. FOUCAUT, J. COUDERT, S. LAVAL, J. OBI, S. 2015 Space–time pressure–velocity correlations in a turbulent boundary layer, J. Fluid Mech., vol. 771, pp. 624–675.

OCEAN, N. & DIEGO, S. 1980 An experimental study of flow-generated on a flexible surface 68,317–334.

PALCHESKO, R. N. ZHANG, L. SUN, Y. & FEINBERG, A. W. 2012. Development of Polydimethylsiloxane Substrates with Tunable Elastic Modulus to Study Cell Mechanobiology in Muscle and Nerve. PLoS One 7.

PANTON, R.L. GOLDAMN, A.L. LOWERY, R.L. & REISCHMAN, M.M. 1980 Low-frequency pressure fluctuations in axisymmetric turbulent boundary layers. J. Fluid Mech. 97 (part 2), 299–319.

PERLMAN, E. BURNS, R. Li, Y. MENEVEAU, C. 2007 Data Exploration of Turbulence Simulations using a Database Cluster. Supercomputing SC07, ACM, IEEE.

PETERSON, J.I. and FITZGERALD, V.F. 1980 New Technique of Surface Flow Visualization Based on Oxygen Quenching of Fluorescence Rev. Sci. Instrum., Vol. 51, No. 5, pp. 670-671

POPE, S.B. 2000 Turbulent flows. Cambridge University Press, Cambridge.

RICHNER, R. P. 2011. Research Collection. Brisk Bin. Robust Invariant Scalable Keypoints 12–19.

ROACHE, P.J. 1976 Computational Fluid Dynamics, Hermosa, Albuquerque, NM, p. 180

RONALD J. ADRIAN. 1991. Particle-Imaging Techniques for Experimental Fluid Mechanics. Annu. Rev. Fluid Mech. 23,261–304.

ROSTI, M. E. & BRANDT, L. 2017. Numerical simulation of turbulent channel flow over a viscous hyper-elastic wall. J. Fluid Mech. 830,708–735.

SEXTON, M.R. O'BRIEN, W.F. and MOSES, H.L. 1973 An on Rotor Investigation of Rotating Stall in an Axial Compressor, Defense Technical Information Center (DTIC) Technical Report, Cameron Station, Alexandria, VA, pp. 33.1-10

SCHEWE, G. 1983 On the structure and resolution of wall-pressure fluctuations associated with turbulent boundary-layer flow. J. Fluid Mech. 134, 311–328.

SCHNEIDERS, J.F.G. PROBSTING, S. Dwight R P, van Oudheusden BW, and Scarano F (2016) Pressure estimation from single-snapshot tomographic PIV in a turbulent boundary layer.

Experiments in Fluids, 57(4), 53.

SHENG, J. MALKIEL, E. & KATZ, J. 2006. Digital holographic microscope for measuring three-dimensional particle distributions and motions. Appl. Opt. 45,3893.

SOUVEREIN, L.J. 2007 Evaluation of integral forces and pressure fields from planar velocimetry data for incompressible and compressible flows, 153–162.

STANISLAS, M. OKAMOTO, K. KAHLER, C.J. WESTERWEEL, J. 2005 Main results of the Second International PIV Challenge, Experiments in Fluids 39: 170–191

SMITH, C. R. & METZLER, S. P. 1983. The characteristics of low-speed streaks in the near-wall region of a turbulent boundary layer. J. Fluid Mech. 129,27–54.

TABATABAI, H. OLIVER, D. E. ROHRBAUGH, J. W. & PAPADOPOULOS, C. 2013. Novel applications of laser doppler vibration measurements to medical imaging. Sens. Imaging 14,13–28.

TALAPATRA, S. & KATZ, J. 2012. Coherent structures in the inner part of a rough-wall channel flow resolved using holographic PIV. J. Fluid Mech. 711,161–170.

TSUJI, Y. FRANSSON, J. H. M. ALFREDSSON, P. H. & JOHANSSON, A. V. 2007. Pressure statistics and their scaling in high-Reynolds-number turbulent boundary layers. J. Fluid Mech. 585,1.

TURBULENT BOUNDARY LAYER CHARAC - TERISTICS OF FLOW OVER A COMPLIANT The University of Oklahoma , Ph . D ., 1969 Engineering , aeronautical University Microfilms , Inc ., Ann Arbor , Michigan. 1969.

VAN OUDHEUSDEN, B.W. 2013 PIV-based pressure measurement. Measurement Science and Technology, 24(3), 32001.

VILLEGAS, A. DIEZ, F. J. 2014 Evaluation of unsteady pressure fields and forces in rotating airfoils from time-resolved PIV. Experiments in Fluids, 55(4), 1697.

VIOLATO, D., MOORE, P. SCARANO, F. 2011 Lagrangian and Eulerian pressure field evaluation of rod-airfoil flow from time-resolved tomographic PIV, Experiments in Fluids, 50(4), 1057–1070.

WANG, Z., YEO, K.S., & KHOO, B.C. 2005 On two-dimensional linear waves in Blasius boundary layer over viscoelastic layers. European Journal of Mechanics B/Fluids 25, 33-58.

WANG, J. ZHANG, C. & KATZ, J. 2019. GPU-based, parallel-line, omni-directional integration of measured pressure gradient field to obtain the 3D pressure distribution. Exp. Fluids 60,0.

WANG, Z. YEO, K. S. & KHOO, B. C. 2006. On two-dimensional linear waves in Blasius boundary layer over viscoelastic layers. Eur. J. Mech. B/Fluids 25,33–58.

WESTERWEEL, J. GEELHOED, P. F. & LINDKEN, R. 2004. Single-pixel resolution ensemble correlation for micro-PIV applications. Exp. Fluids 37,375–384.

WILLMARTH, W. W. 1975 Pressure Fluctuations Beneath Turbulent Boundary Layers. Annual Review of Fluid Mechanics, 7, 13–36.

WORTH, N. A. NICKELS, T.B. SWAMINATHAN, N. 2010 A tomographic PIV resolution study based on homogeneous isotropic turbulence DNS data, Exp Fluids (2010) 49:637–656

YOUNG, J. J. THIBAUT, T. LUDOVIC, C. LAURENT, D. 2014 3D extension of the fluid trajectory evaluation based on an ensemble averaged cross- correlation (FTEE) for acceleration and pressure, 17th International Symposium on Applications of Laser Techniques to Fluid Mechanics.

XU, S. REMPFER, D. & LUMLEY, J. 2003. Turbulence over a compliant surface: numerical simulation and analysis. J. Fluid Mech. 478,11–34.

YU, H. KANOV, K. PERLMAN, E. GRAHAM, J. FREDERIX, E. BURNS, R. SZALAY, A. EYINK, G. and MENEVEAU, C. 2012 Studying Lagrangian dynamics of turbulence using on-demand fluid particle tracking in a public turbulence database, Journal of Turbulence 13, No. 12

ZHANG, C. MIORINI, R. & KATZ, J. 2015. Integrating Mach – Zehnder interferometry with TPIV to measure the time - resolved deformation of a compliant wall along with the 3D velocity field in a turbulent channel flow. Exp. Fluids 56,1–22.

ZHANG, C. WANG, J. BLAKE, W. KATZ, J. 2017 Deformation of a compliant wall in a turbulent channel flow, J. Fluid Mech. (2017), vol. 823, pp. 345–390

CURRICULUM VITA

Date of Birth: August 24th, 1989

Place of Birth: Hubei, China

Education

Ph.D., Johns Hopkins University, Baltimore, Maryland	October 2019
B.S., University of Science and Technology of China	June 2012

Journal Publications

J Wang, SS Koley, J Katz, (2019), "Impact of Deformation of a Compliant Wall on a Turbulent Boundary Layer", submitted to Journal of Fluid Mechanics

J Wang, C Zhang, J Katz, (2019)," GPU-based, parallel-line, omni-directional integration of measured acceleration field to obtain the 3D pressure distribution", Experiments in Fluids, 60 (4), 58

C Zhang, J Wang, W Blake, J Katz, (2017) " Deformation of a compliant wall in a turbulent channel flow", Journal of Fluid Mechanics 823, 345-390

C Li, J Miller, J Wang, SS Koley, J Katz (2017) "Size distribution and dispersion of droplets generated by impingement of breaking waves on oil slicks", Journal of Geophysical Research: Oceans, 122, 7938-7957

Conference Publications

J Wang, C Zhang, J Katz (2018) “GPU-Based, Parallel-Line, Omni-Directional Integration of the Acceleration Field to Obtain the 3D Pressure Distribution”, Proceedings of the 10th International Symposium on Cavitation (CAV2018)

J Wang, C Zhang, J Katz (2017) "GPU-Based, Parallel-Line, Omni-Directional Integration of the Acceleration Field to Obtain the 3D Pressure Distribution", The 12th International Symposium on Particle Image Velocimetry. Busan, Korea (the Republic of). June 18, 2017